TECHNISCHE UNIVERSITÄT WIEN
Vienna University of Technology

DIPLOMARBEIT

Size effects in the catalytic hydrogen oxidation on rhodium

Ausgeführt am Institut für

Materialchemie (165)
der Technischen Universität Wien

unter der Anleitung von

Assoc.Prof. Dipl.-Phys. Dr.rer.nat. Yuri Suchorski

durch

Johannes Zeininger
Stuckgasse 3
1070 Wien, Österreich

Wien, 06.04.2018

Kurzfassung

Polykristalline Edelmetallfolien und µm-große "gebogene" Kristalle, die aus vielen µm-großen Domänen oder Facetten unterschiedlicher Strukturen bestehen, können eine Rolle als "Oberflächenstrukturbibliotheken" spielen. Der Einsatz solcher "Oberflächenstrukturbibliotheken" in Kombination mit ortsaufgelösten kinetischen Experimenten ermöglicht die gleichzeitige Bestimmung der inhärenten katalytischen Eigenschaften verschiedener kristallographischer Orientierungen unter identischen Reaktionsbedingungen. Dieser Ansatz ermöglicht neue Einblicke in die katalytische Zündung und die Ausbreitung von Reaktionsfronten.

In der vorliegenden Arbeit wurde die Wasserstoffoxidationsreaktion an verschiedenen Rh-Proben im Druckbereich von 10^{-6} *mbar* untersucht. Die untersuchten Rh-Proben, die sich durch ihre Größe und Form unterscheiden, haben freiliegende Oberflächen unterschiedlicher kristallographischer Orientierung: (i) Der Scheitel einer nanometergroßen Rh-Spitze, die aus nm-großen Rh(hkl)-Facetten besteht; (ii) eine gekrümmte, µm-große Rh-Einkristallprobe, die aus sub-µm Rh(hkl)-Facetten besteht. Die halbkugelförmige Form dieser beiden Proben erzeugt vollständige kubisch flächenzentrierte “Oberflächenstrukturbibliotheken” und hat eine Form, die mit den in der Katalyse verwendeten Partikeln vergleichbar ist; (iii) eine polykristalline Rh-Probe mit flachen, unterschiedlich orientierten Rh(hkl)-Domänen von 20 bis 100 µm Größe. All diese Rh-Oberflächen repräsentieren katalytische Modellsysteme von wenigen nm bis zu hunderten von µm entlang einer Größenachse.

Zwei Arten von Mikroskopen wurden verwendet, um die Wasserstoffoxidation an den Rh-Proben unterschiedlicher Größe *in situ* abzubilden: das Feldemissionsmikroskop (FEM) und das Photoemissionselektronenmikroskop (PEEM). Beide Techniken sind in der Lage, die lokale Oberflächenbedeckung von adsorbierten Spezies während einer laufenden Wasserstoffoxidationsreaktion zu unterscheiden. Mit Hilfe des *kinetics by imaging* Ansatzes konnte auch ein Zusammenhang zwischen Bildhelligkeit und katalytischer Aktivität (hoher oder niedriger Aktivitätszustand) hergestellt werden. Das katalytische Verhalten der Wasserstoffoxidation auf Rh wurde untersucht und quantitativ in kinetischen Phasendiagrammen zusammengefasst. Ein Größeneffekt bei der Wasserstoffoxidation auf Rh wurde durch Vergleich der nm- und µm-großen Rh-Proben untersucht.

Kinetische Übergänge zwischen der hohen und der niedrigen katalytischen Aktivität wurden untersucht. Solche Übergänge werden von sich ausbreitenden Reaktionsfronten be-

gleitet, die im Temperaturbereich von 413 bis 493 K betrachtet wurden. Auf den µm-großen Rh(hkl)-Domänen der polykristallinen Rh-Folien wurde die Nukleierung von Reaktionsfronten auf mikroskopischen Defekten beobachtet. Es konnte gezeigt werden, dass gestufte Rh-Domänen die vorherrschende Richtung einer sich ausbreitenden Reaktionsfront beeinflussen und Korngrenzen die Wasserstofffront nicht daran hindern, in benachbarte Domänen überzugehen.
Mit dem Feldionenmikroskop (FIM) wurden Wassermoleküle, die als Produkt der Wasserstoffoxidation auftreten, ionisiert und zur Abbildung der Rh-Probenoberfläche verwendet. Auf diese Weise wurden katalytisch aktive Oberflächenbereiche *in situ* abgebildet. Während eines kinetischen Übergangs in den aktiven Zustand wurden die Rh{112} Facetten als Zentren der Reaktionsfrontnukleation identifiziert. Zusätzlich konnte durch FEM-Bildgebung gezeigt werden, dass die zu Rh{112} Facetten angrenzenden Facetten verschiedener kristallographischer Orientierungen die Reaktionsfronten über die gesamte Oberfläche einer gekrümmten Rh Probe, in einer temperaturabhängigen Weise, entlang bestimmter "Ausbreitungswege" führen. Dies lässt sich durch temperaturabhängige sauerstoffinduzierte Rekonstruktionen bei der Wasserstoffoxidation erklären.

Abstract

Polycrystalline noble metal foils and µm-sized "curved" crystals, consisting of many µm-sized domains or facets of different structures, may play a role of "surface structure libraries". The application of such "surface structure libraries" in combination with spatially resolved kinetic experiments allows simultaneous determination of inherent catalytic properties of different crystallographic orientations under identical reaction conditions. This approach allows new insights into catalytic ignition and reaction front propagation. In the present work the hydrogen oxidation reaction was studied on different Rh samples in the pressure range of 10^{-6} *mbar*. The probed Rh samples, that differed by their size and shape, have exposed surfaces of different crystallographic orientation: (i) The apex of a nanometer-sized Rh tip consisting of nm-sized Rh(hkl) facets; (ii) a curved µm-sized Rh crystal sample consisting of sub-µm Rh(hkl) facets. The hemispherical shape of these two samples generates complete fcc "surface structure libraries" and a shape which is comparable to the particles used in catalysis; (iii) a polycrystalline Rh sample exhibiting flat differently oriented Rh(hkl) domains of 20 to 100 µm in size. All these Rh surfaces represent model catalytic systems ranging from few nm to hundreds of µm along a size axis.

Two types of microscopes were used to image *in situ* the hydrogen oxidation on the Rh samples of different sizes: the field emission microscope (FEM) and the photo emission electron microscope (PEEM). Both techniques are able to distinguish the local surface coverage of adsorbed species during an ongoing hydrogen oxidation reaction. Using the *kinetics by imaging* approach, a relationship between image brightness and catalytic activity (high or low activity state) could also be established. The catalytic behaviour of hydrogen oxidation on Rh was studied and quantitatively summarized in kinetic phase diagrams. A size effect in hydrogen oxidation on Rh was studied by comparison of the nm-sized and µm-sized Rh specimens.

Kinetic transitions between the high and low catalytic activity steady states were studied. Such transitions are accompanied by propagating reaction fronts which were monitored in the temperature range of 413 to 493 K. On the µm-sized Rh(hkl) domains of the polycrystalline Rh foil nucleation of reaction fronts was observed on microscopic defects. It could be shown, that stepped Rh domains affect the predominant direction of front propagation and grain boundaries do not prevent the hydrogen front from crossing over to adjacent domains.

Using the FIM, water molecules appearing as a product of hydrogen oxidation were ionized and used for imaging of the Rh specimen surface. In this way, catalytically active surface sites were *in situ* imaged. During a kinetic transition to the active state the Rh{112} facets were identified as centers of reaction front nucleation. In addition, by FEM imaging, it could be shown that the adjacent facets to Rh{112} of different crystallographic orientations guide reaction fronts across the entire surface of a Rh curved sample in a temperature dependent way along certain "front propagation paths". This can be explained by temperature dependent oxygen-induced reconstructions during hydrogen oxidation.

Acknowledgements

I would like to express my thanks to all the people who have supported me during my studies. Particularly I would like to thank...

... my supervisor **Prof. Yuri Suchorski**, who always took the time to guide me since I started to work in his group as a trainee.

... my colleagues **Ivan Bespalov**, **Martin Datler**, **Sebastan Buhr**, **Clara Freytag** and **Philipp Winkler** for the fruitful collaboration and a really great time.

... **Prof. Günther Rupprechter**, the head of the IMC, who enabled me to work at his institute.

... the **Fonds zur Förderung der wissenschaftlichen Forschung (FWF)** and in particular the Special Research Program „Functional Oxide Surfaces and Interfaces“ (SFB F45 „FOXSI“) for financially supporting my research.

... my friends and family for their support and patience, especially **Katrin**.

Table of Contents

Table of Contents

1

Introduction

1.1 A brief history of catalysis

It is known since millennia, that the fermentation of sugar can result in the fabrication of alcoholic spirits, whereas a catalytic ingredient e.g. wild yeast is crucial to the successful conversion [1]. Despite the absence of any specific knowledge about catalysis, corresponding equipment, recipes and instructions had been established and improved, to secure that yeast was inserted in the vessel for an efficient fermentation [2]. In the late 17th century, using early optical microscopes, the presence of "globular formations" in the mash was observed by Antoni van Leeuwenhoek and associated with a successful fermentation process. In 1787 Antoine Laurent Lavoisier quantitatively described the alcoholic fermentation process and concluded that sugar decomposes solely into alcohol and carbon dioxide. In 1836, yeast was understood to be small "plants" that are responsible for the fermentation process by F.T. Kutzing. The resulting early theory of alcoholic fermentation was heavily debated and opposed from leading chemists such as J. von Liebig and J. J. von Berzelius. In that time, Berzelius had just established the term "catalysis" to describe the reaction of substances that can compose or decompose other materials. In 1835 he published his qualitative definition of catalysis as phenomena, where substances can change the progression of a chemical reaction without being consumed [3]. An example of such a phenomenon was reported earlier in 1823 by Johann Wolfgang Döbereiner, who detected the first inorganic catalytic process. He noticed that dispersed platinum causes hydrogen gas to react with oxygen from air. The platinum itself was not altered by the chemical reaction and remained unconsumed [4].

Finally in 1909 W. Ostwald was awarded the Nobel Prize in Chemistry for his definition of catalysis embedded in the concept of chemical kinetics [5]. His statement that "*a catalyst is a substance which affects the rate of a chemical reaction without being part of its products*" marks a period where systematic research on key catalytic reactions by the growing chemical industry, as well as up-scaling of developed processes begun. The most prominent example is possibly the nitrogen fixation process realized by F. Haber in 1909

(Nobel Price 1918) and brought to technical scale by C. Bosch (Nobel Price 1931) [6]. From air and hydrogen NH_3 can be artificially produced and used as a basic precursor to form fertilizers and explosives, which had a dramatic impact on human society in the last century. The possibility to grow food supported by fertilizers contributed to the rise of the global population from 1.6 billion in 1900 to 7 billion today [7].
The first plant led by BASF started the synthesis of ammonia in 1913 using an osmium based catalyst. The catalyst could be replaced after intensive research by an easier accessible alkali promoted iron catalyst which is still the mostly used today. Studies to characterize the used catalysts and reveal the precise kinetics of the process were done along the construction of numerous new plants, but were not able to reveal the full picture of the chemical process. I. Langmuir (Nobel Price 1932) came up with a new idea to first simplify a studied reaction system. A catalytic surface should be idealized by a plane with periodically arranged atoms. This "surface science approach" could render possible, along with the development of ultra high vacuum systems (UHV) and new surface sensitive analytic methods, detailed insights into microscopic surface processes. A significant contribution to the revealing of the complete mechanism of the artificial nitrogen fixation came from G. Ertl (Nobel Price 2007) [8]. In his studies, starting from single crystal surfaces under UHV conditions, the gap towards the real catalytic systems was bridged step by step by increasing complexity of the catalytic model systems both for the catalyst and for the applied conditions.

1.2 Working principle of a catalyst

A catalyst is an additional substance in a chemical reaction e.g. $(A + B \rightarrow C)$ that increases the reaction rate forming the product. In a heterogeneously catalyzed reaction, typically chemical bonds are broken and rearranged between the substrate and reacting species. Figure 1.1 illustrates this idea and shows the activation energy E_a that has to be surpassed to form the product, and the reaction enthalpy e.g. the energy gain from an exothermic reaction. The Arrhenius equation displays the general relation between the activation energy, the rate and temperature. The reaction rate (R) is then given by

$$R = A \cdot e^{(\frac{-E_a}{k \cdot T})} \tag{1.1}$$

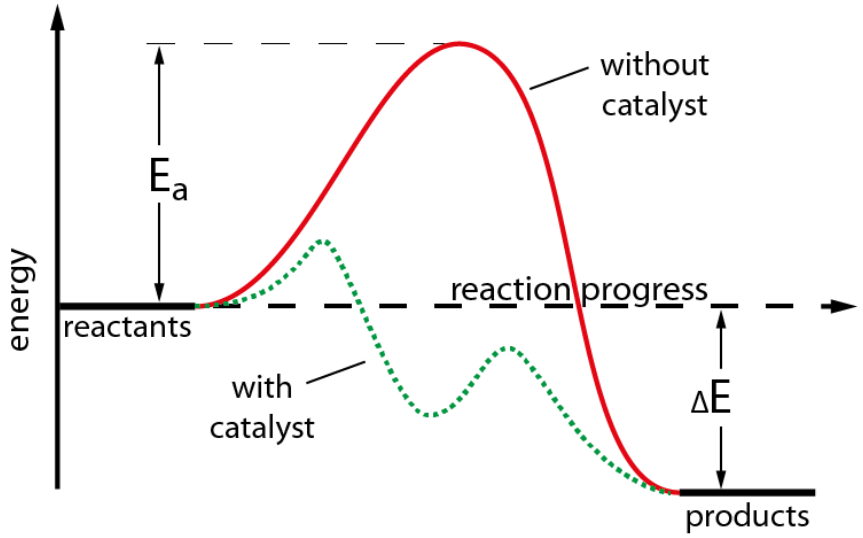

Fig. 1.1. Schematic energy diagram representing the reaction pathway with a catalyst (green dotted line) and without (red line).

where A is a frequency factor, k is the Boltzmann constant and T the temperature. According to Eq. 1.1 an increase of the reaction rate can either be achieved by an increase of temperature or by lowering the activation energy. The latter is realized by using a catalyst which can form intermediates with the reacting molecules and thereby alters the energy-pathway of the reaction as illustrated in Fig 1.1. The resulting activation barriers for the catalyzed reaction are smaller than for the non-catalyzed reaction and therefore the overall reaction rate is higher. As a last reaction step the catalyst is separated from the products and is available for further reaction.

In turn, in homogeneous catalysis the catalyst and the reactants are in the same phase e.g. liquid or gaseous. For example, enzymes in living organisms catalyze various biochemical processes. On an industrial scale catalyzed reactions mostly rely on heterogeneous catalysis, where a solid phase catalyst interacts with the reactants present in different phases (liquid or gaseous). This effect is called heterogeneous catalysis. Atoms from the topmost layers of the catalyst can form bonds with molecules and atoms from the liquid or gaseous phase, a process called chemisorption. During this chemisorbed state bonds might be broken or present bonds can be rearranged. The chemisorbed molecules and atoms can diffuse from their sites to adjacent empty sites and can react with other molecules. The formed product will eventually desorb from the surface, allowing a continuous depletion.

1.3 The noble metal rhodium

Rhodium is a transition metal and displays a silvery, white and metallic appearance. It has the atomic number 45 and is located in the cobalt group of the periodic table (Fig. 1.2a). Its properties are similar to those of palladium and platinum, other platinum group metals (PGM) that show a high catalytic activity. Rhodium is one of the rarest elements in the crust of the earth with a concentration of about 1 ppb. It is mostly found in its native form mixed with ores like silver, gold or other PGMs.

1.3.1 Bulk properties

Rhodium crystallizes, like other group 9 metals, in a face-centered cubic (fcc) arrangement. In the Hermann-Mauguin notation the space group is represented by $Fm\bar{3}m$ (space group number 225). The lattice constant a equals 380.4 pm and there are four formula units within the cubic unit cell (Fig. 1.2b) [9]. The melting point is typical for a PGM with a value of 2239 K. The rhodium metal has the highest thermal and electrical conductivity of all PGM. At a temperature below 0.9 K it becomes a superconductor.

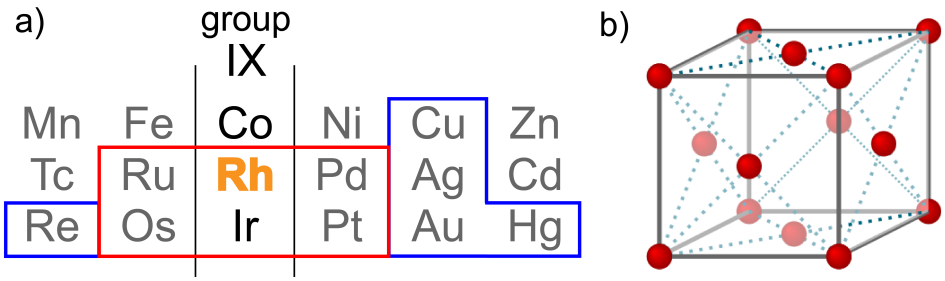

Fig. 1.2. The position of Rh in the periodic table and the Rh crystal structure: a) rhodium belongs to the cobalt IX group of the periodic table. Platinum group metals are enclosed by a red rectangle and noble metals are confined by blue lines; b) face-centered cubic (fcc) lattice of Rh.

1.3.2 Surface structure

A pure rhodium crystal exhibits surfaces of distinct steric orientations which are usually labeled by Miller indices. Figure 1.3 shows three main low index planes. The Rh{111} surfaces are the most dense with hexagonal atom configuration, followed by Rh{100} surfaces showing a cubic primitive surface unit cell and Rh{110} surfaces have the most open surfaces with a rectangular surface unit cell. A real crystal surface can, of course,

also be misoriented from one of the low index planes by a certain tilt. This deviation can be described with three parameters: 1) the tilt zone describes the axis around which the rotation occurs; (2) the tilt azimuth specifies the direction of the tilt and; (3) the tilt angle represents the angle of the rotation. Such surfaces are high Miller index surfaces and in the case of low deviations, they are called vicinal surfaces. They can be described by their corresponding Miller indexes and are composed of terraces limited by steps of monatomic height. When all three positions of the Miller index differ in their value, these rows of step forming atoms also show kinks. Such crystal plane system is graphically illustrated in Fig. 1.3 showing three main low index planes, an example of a stepped surface, an example of a kinked surface and an inverse pole figure (IPF). Three corners of the figure

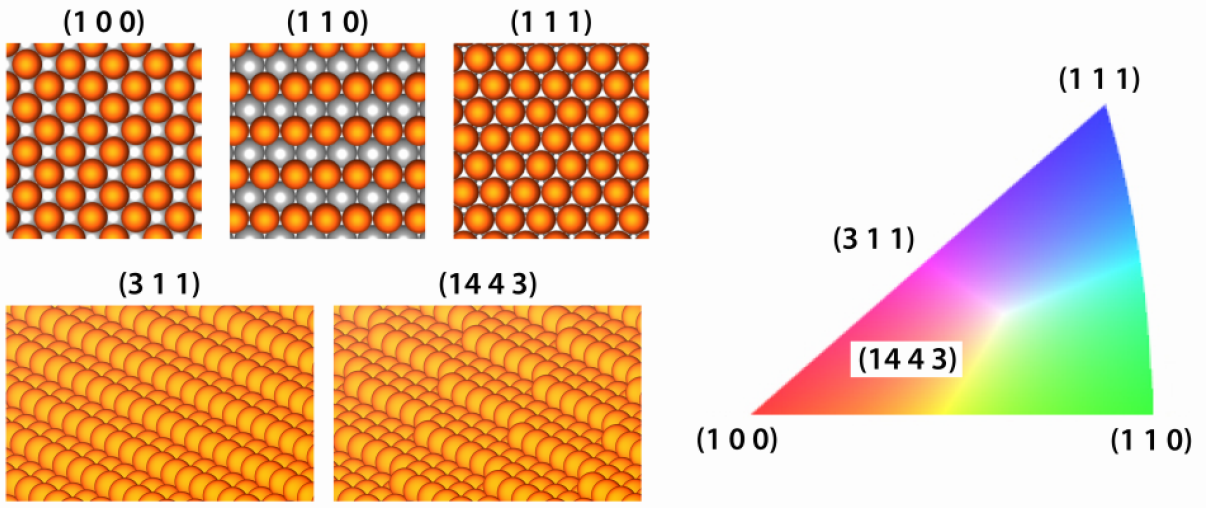

Fig. 1.3. Examples of surface structure: upper row: three low Miller surfaces Rh(100), Rh(110) and Rh(111); lower row: a stepped Rh(311) surface and a Rh(1443) surface with kinked steps; On the right hand side, the inverse pole figure is shown with labeled orientations.

are occupied by the main low index planes represented by fundamental colors. On the lines, that connect the three corners, just pure stepped surfaces are found. The mixing of only two main low Miller index planes results in terraces of the main component and monatomic steps of the minor component. For example, the Rh(311) surface consists of a terrace with (100) orientation and, along the step edge, a narrow (111) oriented surface is formed.

1.3.3 The spherical projection

As described in section 1.3.2, plane crystal surfaces are usually labeled by Miller indices. Methods like electron backscatter diffraction (EBSD, see section 2.4.2) allow to determine

the Miller indices of a certain area of interest of a single crystal or of a domain in a polycrystalline sample.

Intersection of planes with the fcc crystal system generates flat surfaces of a certain crystallographic orientation. However, it is also possible to confine the surface area by an intersecting hemisphere. Such an ideal hemisphere is usually thermodynamically unstable and, upon annealing, facets are formed, which again can be described by Miller indices. At a small hemisphere radius only few low Miller index facets are present, but more stepped facets and even kinked surfaces are formed, when the hemisphere radius is enlarged. Besides the 3D-modeling of such a faceted hemisphere a stereographic projection onto a plane makes it possible to map the surface of such a hemisphere. The projection functions as follows: a sphere, where the southern hemisphere is of interest (Fig. 1.4a), touches a plane, perpendicular to the axis between the origin pole and the infinity pole (Fig. 1.4b). Any point on the southern hemisphere can be mapped by projecting this point from the infinity pole onto the plane. Such projection is called the stereographic projection. Systematical stereographic projection of all facets present on the hemisphere generates a 2D crystallographic map (Fig. 1.4c). Dependent on the orientation of the hemisphere in the fcc lattice one of the main low Miller index facets can be centered in the origin pole. Since the other main low Miller index facets are present on the hemispherical surface, the triangular shaped IPF can be found multiple times in the projection. The above concept can be applied to the curved dome-shaped crystals (see section 3.2) and tip-shaped specimens, both exhibiting faceted hemisphere-like surfaces.

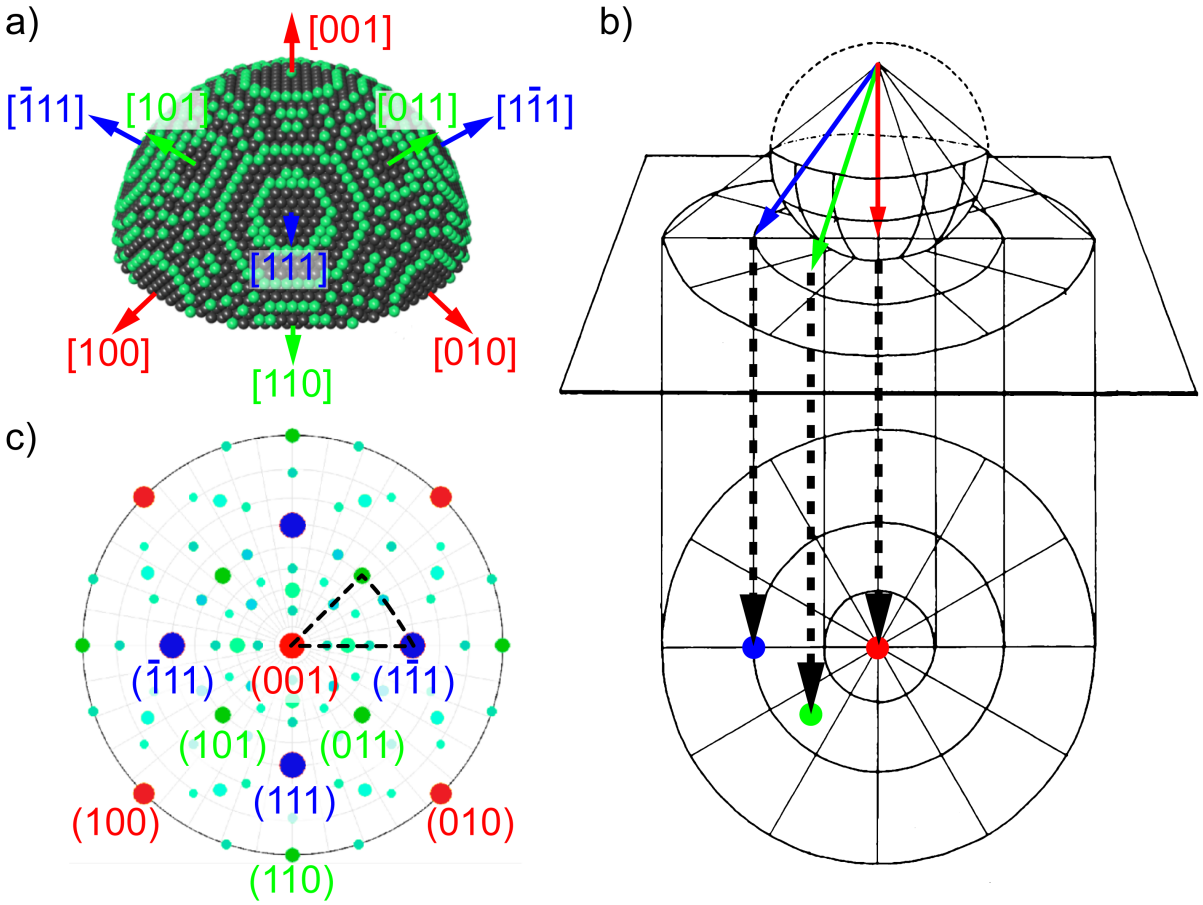

Fig. 1.4. Concept of the stereographic projection: a) a ball model of a [001] oriented Rh tip apex is shown and for convenience the protruding atoms are colored. The orientations of low main Miller index facets Rh{001} are indicated by red, Rh{111} by blue and Rh{110} by green arrows; b) points of interest on the southern hemisphere are projected along lines (colored arrows), from the infinity pole through the point, onto the plane. Projected points form a 2D crystallographic map below; c) a 2D crystallographic map corresponding to the model in (a) is presented. The central red point represents the center of the Rh(001) facet. Other crystallographic orientations are also labeled. One of the possible positions of a triangular shaped inverse pole figure is indicated by dotted lines.

1.4 The hydrogen oxidation reaction

The gas phase hydrogen oxidation reaction is a strong exothermic chemical reaction ($\Delta_r H^0 = -571.6 kJ/mol$) and can be summarized by

$$H_2 + \frac{1}{2}\, O_2 \rightarrow H_2O \tag{1.2}$$

where molecular hydrogen H_2 and molecular oxygen O_2 form water. Hydrogen is the most abundant element on earth and is mostly chemically bound as water or hydrocarbons. The H_2 gas is used worldwide as a raw material in the chemical industry at about $5 \times 10^{10}\ kg$ per year. Most of the H_2 resources are produced from the reaction of water with hydrocarbons at high temperatures (water gas shift reaction) or by the water electrolysis. The possibility to produce hydrogen in a "clean" way, e.g. by the use of sunlight, is one of the "green" possibilities for a clean technology because H_2 can be used as fuel. Since water is the solely reaction product of hydrogen combustion or catalytic oxidation reaction, advantages of H_2 fuel over fossil fuels are evident. Aside from the environmental benefits the energy per mass unit of hydrogen (142 MJ/kg) is higher than for any other chemical fuel. This makes hydrogen an alternative to natural gas for heating, and to fossil fuels used to power vehicles [10, 11]. In power vehicles, hydrogen can either be burned in a combustion engine, where the Carnot efficiency limit is around 25 % for the hydrogen-air mixture, or be used electrochemically in a fuel cell, which powers an electric motor. The resulting efficiency of 50-60 % is approximately twice as high as in the thermal process.
The first commercial use of the catalytic hydrogen oxidation reaction was performed by Döbereiner 1823, when he constructed a "Döbereiner-lighter" [12]. There, hydrogen, produced from the reaction of acid with a not-noble metal, was used to catalytically react with oxygen from air at a Pt sponge. The exothermic catalytic reaction heats up the platin sponge which in turn provides the activation energy for the gas reaction (combustion). Döbereiner exploited the fact that the reaction between H_2 and O_2 can occur as both, a gas phase reaction or over a heterogeneous catalytic path. A detailed H_2/O_2 reaction mechanism for the gas phase reaction was refined from experimental kinetic data and thermochemical studies at different conditions [13]. The catalytic hydrogen oxidation reaction discussed in section 1.4.1 in turn has a small activation energy barrier and happens spontaneously.

1.4.1 Catalytic hydrogen oxidation

As already mentioned in section 1.4, the hydrogen oxidation reaction can be heterogeneously catalyzed by transition metals such as platinum and rhodium. Beside its technological relevance for energy conversion, the catalytic hydrogen oxidation reaction is interesting from a fundamental point of view. A heterogeneously catalyzed reaction requires the adsorption of at least one reactant on the catalyst surface. In case both reactants adsorb on the surface prior to reaction, the reaction mechanism is called "Langmuir-Hinshelwood-mechanism" [14]. The Langmuir Hinshelwood mechanism generally occurs in the catalytic hydrogen oxidation reaction on transition metals [15]. Both reacting species H_{ads} and O_{ads} adsorb on the surface dissociatively from H_2 gas and O_2 gas before the reaction and compete for the same adsorption sites. An empty adsorption site is represented by $*$.

$$O_{2,\ g} + 2 * \rightleftharpoons O_{2,\ ads} + * \rightarrow 2\ O_{ads} \tag{1.3}$$

$$H_{2,\ g} + 2 * \rightleftharpoons H_{2,\ ads} + * \rightarrow 2\ H_{ads} \tag{1.4}$$

Assuming Langmuir-Hinshelwood behavior, the reaction rate towards H_2O can be determined as

$$R = \frac{kK_H K_O p_{H_2} p_{O_2}}{(1 + K_H p_{H_2} + K_O p_{O_2})^2} \tag{1.5}$$

where k is the reaction constant for water formation (Eq. 1.2), K_O and K_H are adsorption constants, p_{O_2} and p_{H_2} each represent the partial pressure of a species, and R equals the reaction rate times the surface coverages of both species [16]. If one species e.g. hydrogen is weaker adsorbed compared to oxygen species ($K_H << K_O$) and p_{H_2} is in the range of p_{O_2} , following approximation is valid at low pressures ($K_O p_{O_2} << 1$)

$$R = kK_H K_O p_{H_2} p_{O_2} \quad . \tag{1.6}$$

At high pressures, where p_{O_2} inhibits the reaction by saturating the surface with O_{ads}, the rate equation can be formulated as

$$R = \frac{kK_H p_{H_2}}{K_O p_{O_2}} \quad . \tag{1.7}$$

Equations 1.6 and 1.7, representing the reaction rate in low and high pressure regimes, are limiting cases which enclose the maximum for the reaction rate.

The following sequence of reaction equations is suitable to describe the formation of water on the catalysts surface, when O_{ads} and H_{ads} are present.

$$O_{ads} + H_{ads} \rightleftharpoons OH_{ads} + * \tag{1.8}$$

$$OH_{ads} + OH_{ads} \rightleftharpoons H_2O_{ads} + O_{ads} \tag{1.9}$$

$$OH_{ads} + H_{ads} \rightarrow H_2O_{ads} + * \tag{1.10}$$

$$H_2O_{ads} \rightarrow H_2O_g + * \tag{1.11}$$

The species O_{ads} and H_{ads} react (1.8) and form the intermediate OH_{ads} and a free surface site $*$. The OH_{ads} species requires an additional hydrogen atom to form water, which is either contributed by another OH_{ads} (1.9) or by H_{ads} (1.10). Partial pressures below 1×10^{-5} $mbar$ for both hydrogen and oxygen and the removal of the reaction product water by pumping ensures the desorption(1.11) of water from the catalytic surface to be almost irreversible.

For the catalytic hydrogen oxidation reaction two different mechanisms contribute as competing and parallel pathways to the H_2O formation (Fig 1.5) [17]. The OH_{ads} + H_{ads} pathway (Fig 1.5a) forms one equivalent of OH_{ads} during the reaction and all steps towards H_2O_{ads} are exothermic. The pathway is the major contribution to the water production rate in a temperature range of 373 $\leq$T$\leq$ 723 K. The OH_{ads} disproportionation pathway (Fig 1.5b) forms two equivalent OH_{ads} to produce H_2O_{ads}. This pathway plays a minor role for the rate of water formation, but as temperature increases, the overall surface coverage decreases and the pathways contribution to water formation is higher.

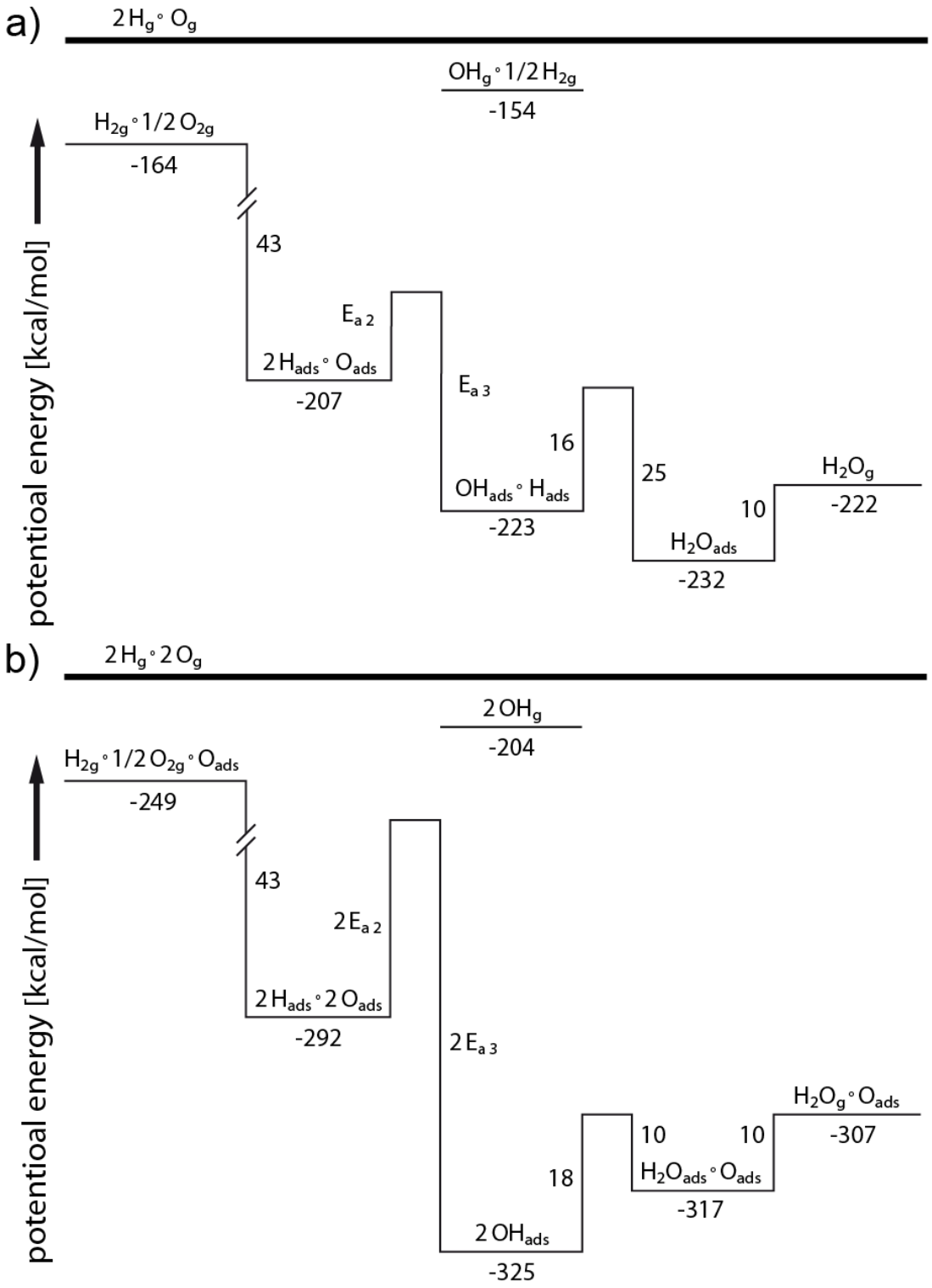

Fig. 1.5. Competing parallel pathways of the catalyzed hydrogen oxidation reaction [17]: The activation energy $E_{a\ 2} \leq 13\ kcal/mol$ and the energy gain $E_{a\ 3} \leq 29\ kcal/mol$ are valid for both pathways. a) The $OH_{ads} + H_{ads}$ pathway is shown in detail. The first and the second potential well shift toward the zero potential line when the oxygen surface coverage increases. In turn the well containing H_2O_{ads} decreases its potential energy. a) The disproportionation of OH_{ads} is shown in detail. 2 $E_{a\ 2}$ - 2 $E_{a\ 3}$ results in a potential difference of 33 kcal/mol.

1.4.2 Adsorption from the gas phase

The surface in heterogeneous catalysis may break bonds of molecular species. In the case of the catalytic hydrogen oxidation reaction a competitive dissociative adsorption of diatomic molecules H_2 and O_2 precedes the reaction. The impinging molecule dissociates into two atoms, this process needs two free adjacent adsorption sites for each adsorbing molecule. The ratio of the adsorption rate to the impinging rate is called sticking coefficient, which is dependent on a steric factor, the energy gain of the adsorbed species, the surface coverage and the temperature. Dependent on conditions, the adsorbates form two-dimensional structures on the substrate. These ordered or disordered surface phases can also alter the substrate and can lead to the relaxation and reconstruction of Rh surfaces as discussed in section 1.4.3. Adsorption and desorption of hydrogen and oxygen on differently oriented Rh surfaces and the resulting ordered adsorbate layers on Rh substrates are discussed briefly below.

The chemisorption properties of hydrogen and oxygen on Rh(111) and Rh(100) planes were studied at exposures of $1 - 10^3$ L, at pressures of $10^{-8} - 10^{-5}$ $mbar$ and at temperatures of $273 - 573$ K [18]. Adsorbed hydrogen does not alter the (1×1) surface structure of the clean Rh(111) and Rh(100) surfaces. The peak maximum in the hydrogen desorption spectrum (Fig. 1.6a) has been measured at 423 K for the Rh(111) substrate. Adsorbed oxygen in turn forms a (2×2) structure at about 0.25 coverage on Rh(111)

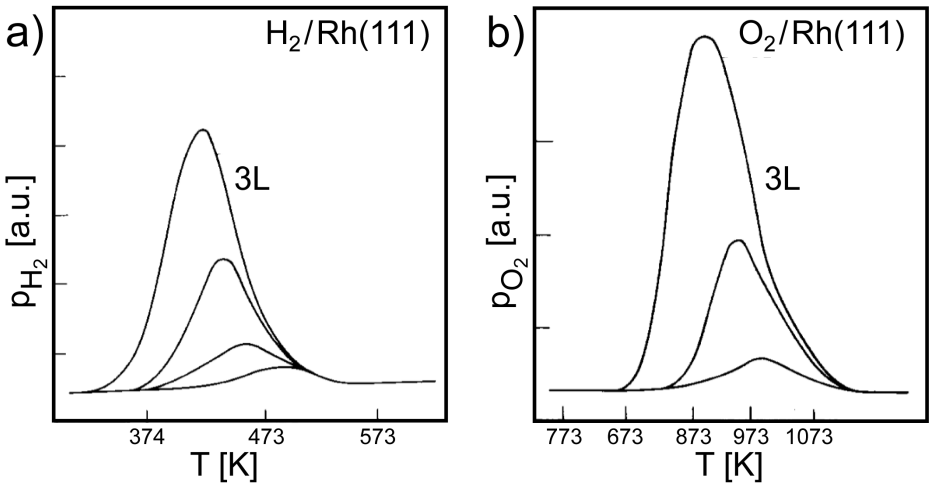

Fig. 1.6. Thermal desorption spectra measured for the (a) H_2 and (b) O_2 adsorbed Rh(111) surfaces. Adapted from Ref. [18]

and Rh(100) surfaces. An increased exposure to O_2 reversibly creates a c(2×2) phase on

Rh(100) surfaces. Oxygen starts to desorb at 670 K (Fig. 1.6b) from the Rh(111) surface. At oxygen coverages around 0.5 monolayer, a (2×1) adsorbate structure is formed on Rh(111) surfaces [19]. Further dosing of oxygen ($10^5 L$) consumes the existing phases and forms an (8×8) overlayer or an (1×1) overlayer if atomic oxygen is used [20–22]. It is assumed that the adsorbate structures (2×2) and (2×1) shown in Fig. 1.7 include a number of hydrogen trap sites for the small H atom [23]. This trap sites seem to stabilize

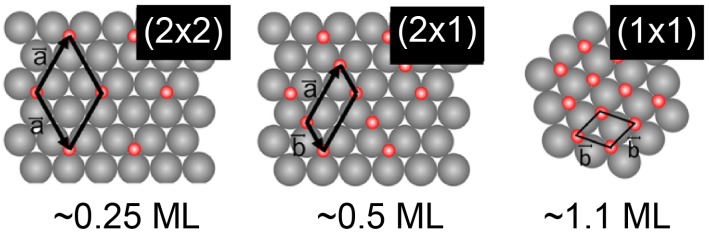

Fig. 1.7. Schematic view of a (2×2), a (2×1) and a (1×1) structure on a Rh(111) substrate. Adsorbed atoms are represented by red dots and surface Rh atoms by bigger gray dots. The area of the shown unit cell decreases when the coverage of oxygen increases from 0.25 monolayer to 1.1 monolayer. The increase of the oxygen coverage closes possible adsorption sites for smaller molecules like H_2. Adapted from Ref. [19]

the dissociated H_{ads} atoms and enable the oxidation reaction. On Rh(110) six different phases with long range order were reported for O_{ads}, where the structures depend on the surface coverage of oxygen and temperature [24]. The temperature desorption spectrum reveals six oxygen binding states having temperature maxima in the range of 780 to 1150 K. Oxygen adsorption studies on a stepped Rh(711) substrate revealed that, besides the c(2×2) phase typical for Rh(100) terraces, ordered oxygen structures of the type $(1 \times N)$ are present due to Rh(111) steps [25].

It is further reported that, at oxygen saturation, up to 60 % of the adsorbed oxygen may be present in subsurface sites. The oxygen incorporation is increased when steps are present and the temperature was elevated to 675 K [25]. This intercalation of oxygen atoms marks the beginning initial oxidation of Rh surfaces and is discussed in section1.4.4 in detail.

Studies performed with the field emission microscopy report that the desorption of hydrogen is virtually complete at about 450 K but part of the hydrogen goes beneath the surface and is desorbed at $600 - 800\ K$ [26]. In the same study oxygen starts to desorb at 600 K with a maximum observed at 950 K. No evidence of adsorbed water above 280 K were found and it is likely that formed water immediately desorbs.

1.4.3 Reconstruction of rhodium surfaces

Surfaces of transition metals do not usually show an ideal bulk like termination. Because of the high density of dangling bonds the surface free energy can be minimized by the rearrangement of atoms which form new bonds or by charge transfer between dangling bonds, a mechanism called autocompensation. However, the rearrangement of atoms can form lattice stress increasing surface free energy. The combination of these two contrary effects may lead to the formation of a particular reconstruction of the surface in order to minimize surface free energy. The instability of ideal surfaces becomes evident when chemical species adsorb on the surface.

The Rh(110) surface is a prominent example for such a reconstruction, where dissociative adsorption of oxygen at temperatures beyond 400 K induces a missing row reconstruction [27]. At oxygen coverages of 0.5 to 0.8 monolayer ($1 \times n;\ n = 2 - 5$) missing row reconstructions are observed where i.e. every nth $[1\bar{1}0]$ row is missing. An adsorbate induced step-doubling reconstruction of the Rh{332} surface is induced by a change of external parameters. Different paths lead to the reversible reconstruction governed by oxygen pressure and temperature. [28]. Another study exposed a nm-sized Rh tip (Fig. 1.8a) to oxygen in a temperature range between 400 to 600 K [26]. Already exposures of 0.5 L lead to structural changes observed with field ion microscopy. Facets such as Rh{110} and Rh{113} are reconstructed in mixtures of (1×2) and (1×3) missing row reconstructions. It is summarized that no structural changes were observed below 400 K and it can be argued that the process of reconstruction is thermally activated. Figure 1.8b shows a ball model of a Rh($\bar{1}13$) tip before and after the (1×3) missing row reconstruction discussed above. The Rh atomic chain positioned in the third layer could not be imaged at 35.5 V/nm and is therefore labeled as arbitrary. The increased mobility of Rh atoms, in the presence of oxygen and at temperatures above 400 K ,leads to such surface reconstructions. It is reported, that the liberated Rh atoms may have diffused into Rh(001) terrace regions as indicated by a smoothing of facet boarders [26].

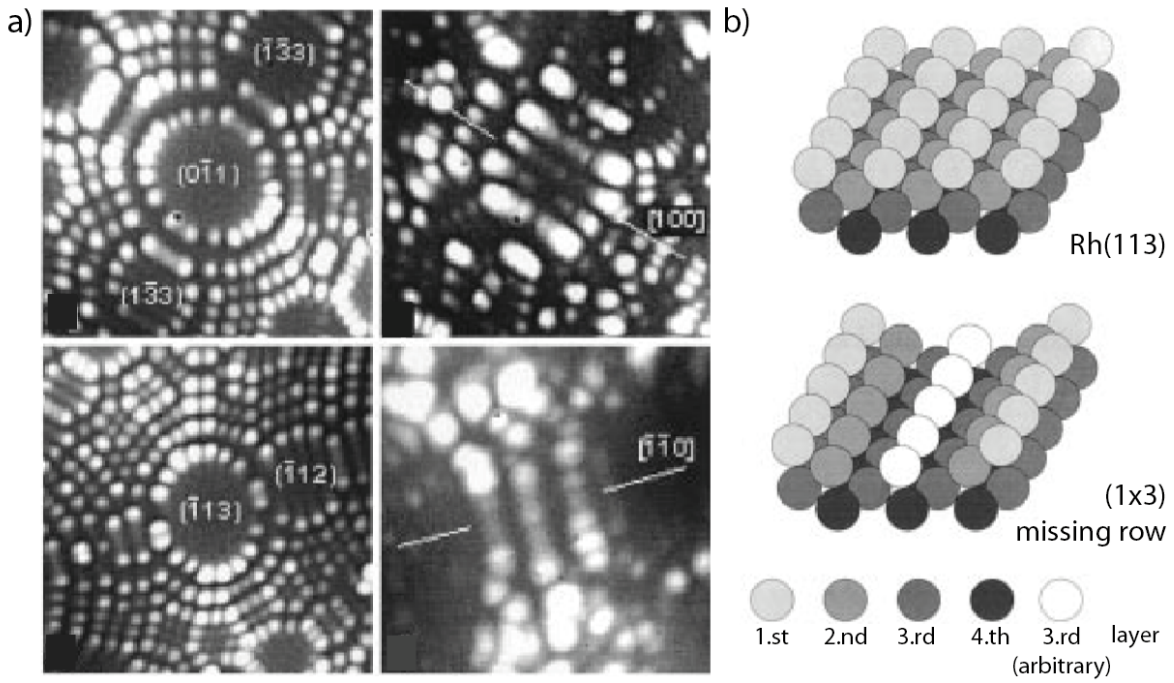

Fig. 1.8. Segments of a FIM image of a [001]-oriented Rh tip apex (adapted from Rev. [26]): a) left hand side: Images of the clean surface planes $(0\bar{1}1)$ and $(\bar{1}13)$; right hand side: The same planes right after oxygen adsorption at 550 K; b) Ball model for the Rh(113) surface and the corresponding (1×3) missing-row reconstruction. A third layer Rh atomic chain is arbitrary and could not be imaged in FIM.

1.4.4 Oxidation of rhodium

The initial stages of Rh oxidation follow the formation of an adsorbed oxygen phase as described in section 1.4.2. The initial oxidation process of Rh(100), Rh(110) and Rh(111) surfaces was studied with laterally resolved X-ray electron spectroscopy and is described in terms of an O-Rh-O trilayer which functions as a precursor for the formation of bulk Rh_2O_3 [27]. Oxidation at slow rates was observed already at room temperature but the formation of complete trilayer was noticeable above 520 K. The study further reports that the initial oxidation performed using molecular O_2 results in an inhomogeneous oxide growth in contrary to experiments with atomic oxygen. It is concluded that structural defects and irregular structures are more effective sites for O_2 dissociation and stabilize the RhO_2 stoichiometry oxide. An oxidation study probing a nanometer sized Rh tip apex in the temperature range of 350 to 483 K reports the intensive oxidation of the (111)-vicinals [26]. It was observed that the high number of kink density in these areas (Fig. 1.8) facilitate the oxidation. The temperature of 417 K is reported to be the initial temperature for the oxide granulation of the Rh(111) vicinals.
The initial oxidation of Rh(111) surfaces was studied in detail. Temperature-programmed desorption spectroscopy revealed a low binding energy state for oxygen which was linked to the formation of subsurface oxygen [29]. The analysis of LEED intensity data revealed that adsorbed oxygen on Rh(111) increases the topmost layer spacing by approximately 3 % [30]. This effect enables the diffusion of oxygen at moderate temperature and coverages into subsurface regions and was observed for the (2×2) and the (2×1) oxygen adlayers. Additional X-ray photoelectron diffraction data showed that at an oxygen exposure of $10^5 L$ at 470 K about 5 % of a monolayer of adsorbed oxygen is present in octahedral interstitial sites just below the fcc adsorption sites [31, 32].
The following model was proposed for subsurface oxygen formation on a Rh(111) substrate: On a surface with a 0.5 monolayer oxygen coverage, where oxygen occupies fcc hollow sites, further oxygen adsorption is kinetically hindered. At 470 K the surface is thermally activated and more oxygen can adsorb on top adsorption sites where the coverage remains below one monolayer. At this oxygen adsorption phase adsorbed oxygen starts to dissolve into the bulk and formation of subsurface oxygen at octahedral interlayer sites is observed. Above this sites adsorbed oxygen switches from fcc to hcp hollow sites. It is assumed that O_{sub} can hop from the octahedral subsurface site to the fcc hollow site. Such a surface, with both fcc and hcp hollow sites occupied, shows changed analytical properties for reactions requiring atomic oxygen. In addition, subsurface oxygen can also

be an auxiliary source of atomic oxygen that supports a catalyzed reaction.
DFT calculations have shown, that oxygen incorporation into subsurface regions is possible already at low coverages i.e. for Rh, at a point when the oxide phase becomes thermodynamically more stable than the chemisorbed oxygen surface phase. It is concluded, that subsurface oxygen is a metastable precursor to oxide formation, which follows immediately at not too low temperatures [32].

1.4.5 Bistability in hydrogen oxidation and the kinetic phase diagram

The catalytic hydrogen oxidation reaction follows the Langmuir-Hinshelwood mechanism as already explained in section 1.4. Both, hydrogen and oxygen adsorb dissociatively on the catalyst surface and follow step $1-6$ of elementary reactions which result in H_2O formation. At any set of external parameters (p_{H_2}, p_{O_2} *and* T), the competitive adsorption of H_2 and O_2 for adjacent empty surface sites is nonequivalent. As a result the surface becomes predominantly covered either by oxygen or by hydrogen and the catalytic H_2 oxidation on Rh operates in one of two different steady states. When the adsorption of hydrogen prevails, the system is in a high activity state where the reaction rate is high. The adsorbed hydrogen atoms frequently recombine to H_2 and desorb, leaving empty surface sites for the adsorption of hydrogen and oxygen. The O_{ads} can immediately react towards the intermediate species OH_{ads} which forms water either by a reaction with H_{ads} or by OH_{ads} disproportionation [17]. Reaction conditions which favor the adsorption of oxygen render in turn the reaction in a low activity state. A high surface coverage of O_{ads} creates a dens oxygen adlayer on Rh surfaces that blocks the dissociative adsorption of H_2 since adjacent free surface sites are hardly present on the surface. The surface is in a "poisoned" state and the reaction rate is diminished.
An abrupt change of the kinetic behavior of the catalytic system at small variations of a control parameter i.e. a switch from one steady state to another one is called a kinetic phase transition [33]. Such a transition is usually accompanied by nucleation and propagation of reaction-diffusion front as explained in detail in section 1.5 [34–36].
In Figure 1.9a the water production is schematically shown as dependent on the p_{H_2} partial pressure (p_{O_2} and T are constant). When starting at a low p_{H_2} (low reaction rate), and p_{H_2} is increased to a critical value $p_{H_{2,\tau_A}}$, a kinetic phase transition to the active state occurs as indicated by a step in the blue dotted line. The corresponding transition point is labeled with τ_A and stands for the steep increase of the reaction rate from the low activity

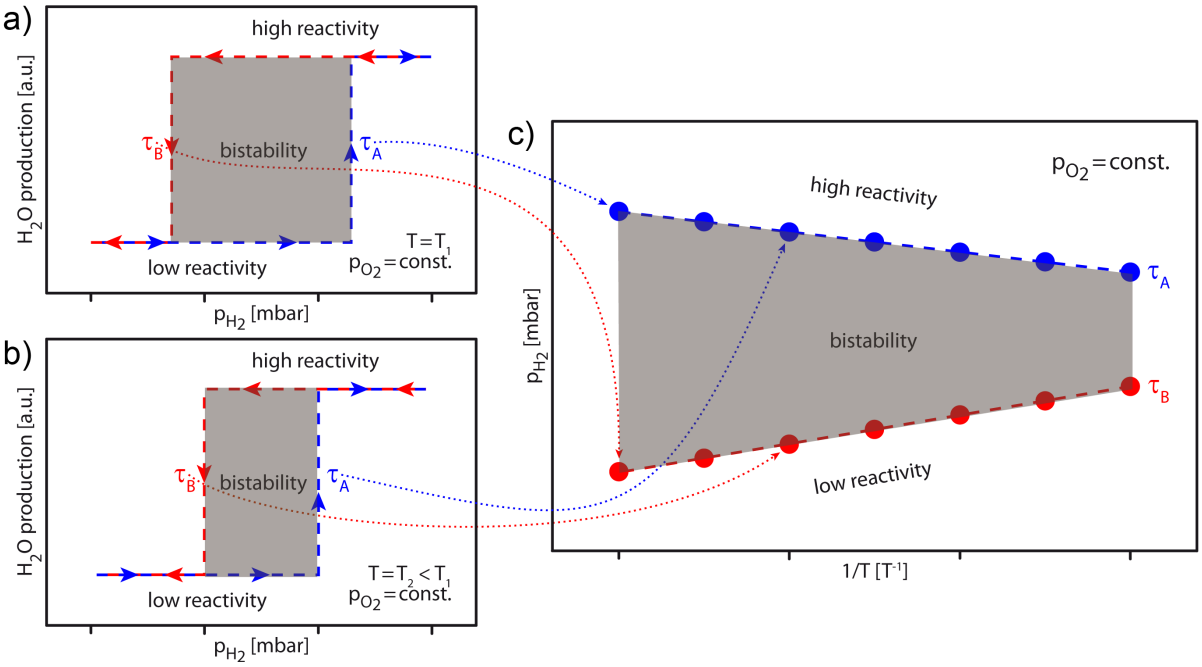

Fig. 1.9. Water formation hysteresis and the construction of a kinetic phase diagram: a) Schematically drawn hysteresis curve for the H_2O production in the catalytic hydrogen oxidation reaction. The parameters p_{O_2} and T_1 are constant; b) a second hysteresis curve is shown where the temperature T_2 is lower than T_1. At this temperature the kinetic transition points τ_A and τ_B are closer together reducing the bistability area along the p_{H_2} coordinate; c) the kinetic phase diagram is constructed from transition points (τ_A and τ_B) at a corresponding temperature as indicated by dotted lines. The region of bistability divides the regions of low and high activity.

regime to the high activity regime. Contrary τ_B labels a kinetic transition from the high activity regime to the low activity regime when the p_{H_2} is decreased subsequently to the critical value $p_{H_{2,\tau_B}}$. Due to the asymmetry in H_2 and O_2 adsorption, $p_{H_{2,\tau_B}}$ is lower than $p_{H_{2,\tau_A}}$ and at a cyclewise variation of p_{H_2} the resulting R_{H_2O} curve shows a hysteresis-like shape. This behavior of the catalytic reaction is called bistability and the region between τ_A and τ_B is labeled accordingly in Fig. 1.9. At the same constant p_{O_2} the τ_A and τ_B values appear to be different at different temperatures (Fig. 1.9b) [37]. From the pairs of τ_A and τ_B, measured at different temperatures but at the same p_{O_2}, a kinetic phase diagram can be constructed by plotting the obtained τ_A and τ_B values against the reciprocal temperature as is shown schematically in Fig. 1.9c. Regions of monostability i.e. of low activity and high activity and region of bistability are labeled. Using such kinetic phase diagrams, different reaction systems can be easily compared. The influence of a change in composition, structural differences and complexity on the kinetic behavior can be interpreted by the changes in the individual kinetic phase diagrams [38].

1.5 Reaction-diffusion fronts

Kinetic phase transitions may result in the appearance of reaction fronts. In general such a front is represented by traveling concentration gradients of different species. In the hydrogen oxidation reaction an induced kinetic transition appears as propagation of hydrogen and oxygen reaction fronts correspondingly. Such fronts were observed on Rh(110) surfaces in a temperature range from 480 to 780 K [39]. Such reaction fronts nucleate usually on defects and may show an anisotropy in their directional propagation. This anisotropy changes when an external parameter, e.g. partial pressure or temperature, varies. The change of parameter may have an effect on the substrate structure, the coverage dependent activation barriers of diffusion and therefore on the reaction front itself, because it results from coupling between diffusion and reaction. The hydrogen oxidation reaction on Rh(111) surfaces were studied at about 450 K and revealed an uniform spreading of reaction fronts on the substrate [40, 41] but also triangular shaped reaction fronts could be observed at high exposures of oxygen (10^6 L) in H_2 titration experiments [42]. For the Rh(533) surface, a step induced diffusion anisotropy was noticed for the hydrogen oxidation reaction resulting in elliptically shaped patterns [43]. Faster front propagation along the step edges caused the anisotropy.
Besides the rough structure of a high Miller index surface, also structural defects can generate a spatial dependence of diffusivity. Subsequently, reaction fronts move in a discontinuous way as it was shown on an imperfect Pt(100) surface for the CO oxidation reaction: a "stop-and-go" nature of the spreading of fronts upon crossing monatomic steps or mesoscopic step bunches was noticed [44].
Studies of the front propagation on platinum group metals (Pt,Pd,Rh and Ir) prepared as a faceted tip apex, where different crystallographic orientations are present, could show the nucleation and evolution of hydrogen oxidation reaction fronts. In the performed catalytic titration reaction ($H_{2\ g} + O_{ads} \rightarrow H_2O_{ads} + H_{ads}$) on the Rh sample the influence of the crystallographic orientation at constant external parameters becomes evident [45]. That study also revealed the temporary catalytically active sites and reported an orientation specific reaction sequence by monitoring the reaction fronts.

1.6 The *kinetics by imaging* approach

The external energy can be transferred to the electron system of a solid sample by illumination, e.g. UV-light or X-rays. If the amount of transferred energy per photon exceeds

the work function, an electron can be emitted to vacuum outside the solid surface. The work function equals the energy difference of the Fermi level of the material and the vacuum potential. In this way, the work function is a specific property of the material surface and depends i.e. on the crystallographic orientation, contamination and adsorbed species. When a Rh surface is covered with H_{ads} the work function increases for about 0.3 eV at 300 K against the clean Rh surface and saturation by adsorbed oxygen leads in turn to an increase of 0.9 eV in respect to a clean Rh surface [46].
The correlation of the work function with the surface coverage of adsorbed species in a catalyzed surface reaction is the basis of the concept of a *kinetics by imaging* approach [47]. In Figure 1.10 this concept is summarized. As already discussed in section 1.4.5, the cat-

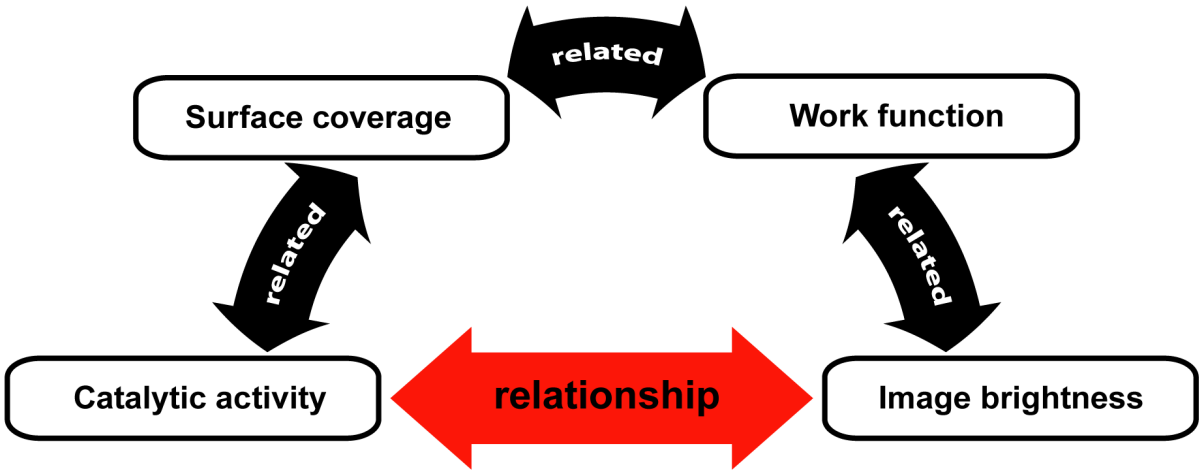

Fig. 1.10. Schematic relation between the catalytic activity and the image brightness: for some reactions, i.e. the catalytic hydrogen oxidation reaction, the catalytic activity is related to the coverage of chemical species adsorbed on the surface. The surface coverage by adsorbates can alter the work function of the sample surface. Thus the work function reflects the catalytic activity [47].

alytic hydrogen oxidation reaction can be in different states of catalytic activity. These states are accompanied by corresponding surface coverages of adsorbed hydrogen and oxygen. This coverages govern the catalytic activity and in the same time vary the work function. Therefore, a relationship between the catalytic activity and the image brightness can be established. This allows the "image based" study of the reaction kinetics, and since the microscopic images are in a natural way spatially-resolved, spatially-resolved kinetic studies (local kinetics) become possible [38, 47, 48].

2

Experimental

2.1 Experimental setups

2.1.1 The ultra-high vacuum system

A vast majority of experiments performed to reveal the composition of a sample have to be performed under ultra-high vacuum (UHV) conditions. There are different opinions at which pressure the UHV region starts. This section follows two basic considerations leading to different terminologies. The UHV pressure range might start at 1×10^{-7} *mbar*. This is argued with the nature of gas flow. When the molecular flow regime is present, the *mean free path* excels the diameter of the vessel, resulting in collisions between particles to occur far less frequent than collisions with inclusive surfaces. However, considering the concept of *time to form a monolayer*, a vacuum in the order of 1×10^{-9} *mbar* is required to achieve a monolayers arrival time of minimum one hour. This is the typical time range to perform an experiment, that needs the sample surface essentially unchanged by absorbed species. In addition, UHV as a prerequisite is above all inevitable for high voltage applications (section 2.2) to avoid breakdown or glow discharge.
An ultra-high vacuum system integrates one or multiple chambers, a pumping stack, valves, process equipment (i.e. sample holders, load locks, heaters, etc.) service components, and facilities for surface analysis. In the following subsections two multicomponent UHV set-ups are introduced and the relevant components are discussed.

2.1.1.1 The FEM/FIM system

The system consists of a main chamber which is connected to a gas supply line (Fig. 2.1), that can be separated by a valve. The gas supply line is equipped with four leak valves and is used as a primary zone for establishing the wanted gas composition. The base pressure of 1×10^{-10} *mbar* is achieved by a rotary pump, connected upstream to a turbomolecular pump. A gate point can distribute the pumping speed to both chambers by throttling valves. Three ion getter pumps and an auxiliary titanium sublimation pump complete

the pumping system and allow maintaining the base pressure. The quadrupole mass spectrometer and three ionization gauges enable the residual gas analysis as well as the total and partial pressure monitoring during experiments. The main chamber holds a high field microscope setup explained in detail in section 2.2.

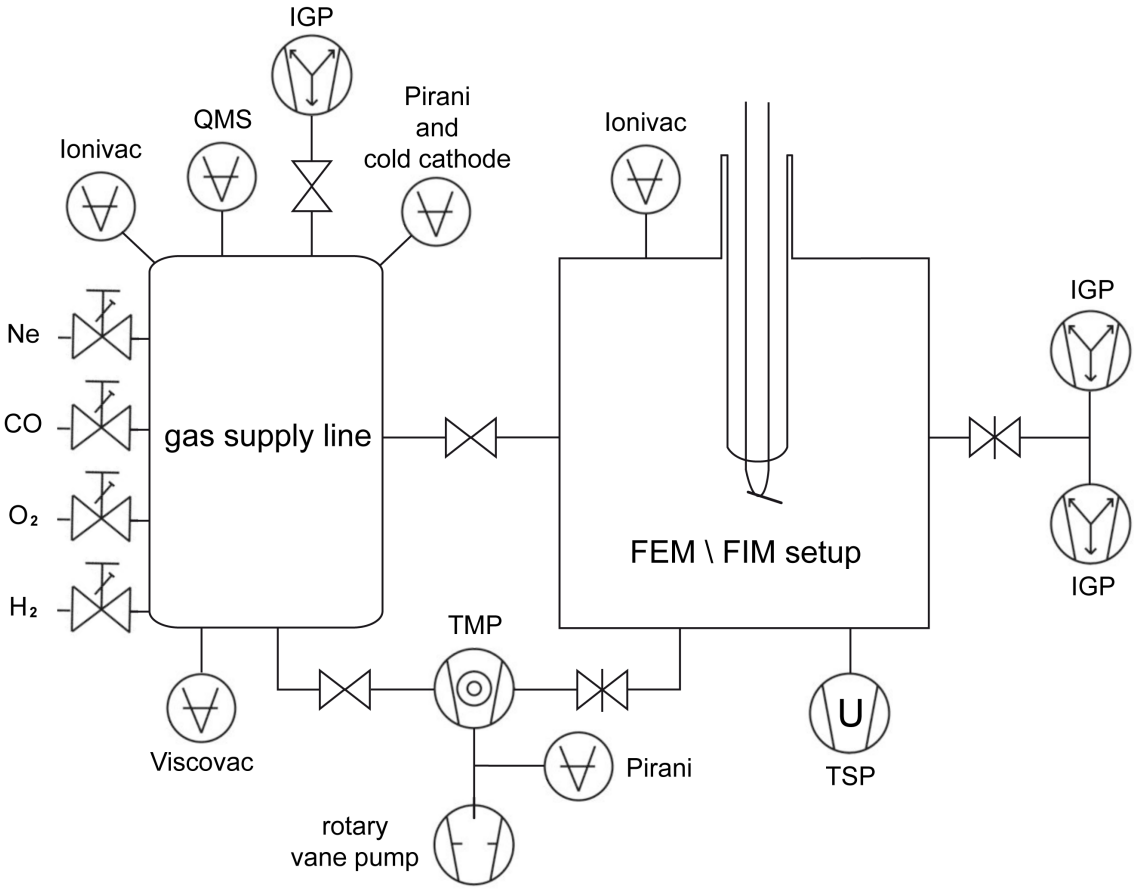

Fig. 2.1. Technical drawing of the FEM/FIM UHV system. The main chamber holds the FEM/FIM-setup and is connected to the gas supply line by a valve. The UHV is achieved by a row of pumps and is monitored by a set of total pressure gauges. The reaction gas atmosphere is controlled by leak valves connected to the gas supply and partial pressures are monitored by a residual gas analyzer.

2.1.1.2 The PEEM/XPS system

The second system is a multifunctional UHV setup with a base pressure of 1×10^{-10} *mbar*. It consists of two chambers interlinked with a load lock (Fig. 2.2). The chamber *A*, equipped with a photoemission electron microscope (section 2.3.3) and a UV deuterium discharge lamp, functions as a microscopy chamber. A spectroscopy chamber *B*, equipped

with an x-ray source and an hemispherical energy analyzer, complements the UHV system setup. Two linearly aligned gate valves and a sample transfer system allow the positioning of the sample in the separated zones for experiments. Sample manipulators with integrated heating devices allow, in turn, precise positioning of the sample within a chamber. To achieve UHV conditions, rotary pumps and turbomolecular pumps as well as the ion getter pumps are mounted. Different gauges and quadrupole mass spectrometers monitor the vacuum conditions and partial pressures in different zones of the setup during an experiment. The mixture of reaction gases can be adjusted by a leak valve connected to each gas supply line.

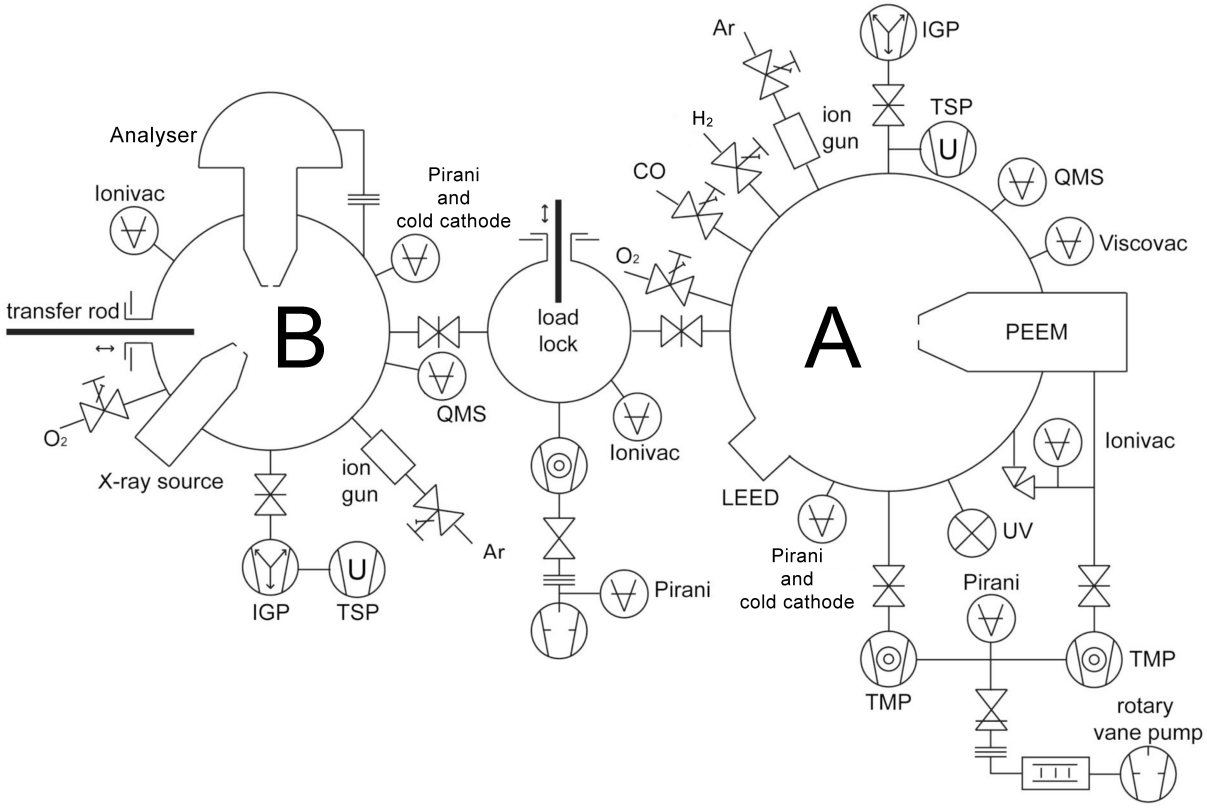

Fig. 2.2. Technical drawing of the PEEM/XPS UHV system. The microscopy chamber A, which holds a PEEM, is connected to the spectroscopy chamber B, which holds a XPS-setup through a load lock. UHV is achieved by different pumps and is monitored by a set of total pressure gauges. The reaction gas atmosphere can be controlled by leak valves connected to the gas supply and partial pressures are monitored by two residual gas analyzers.

2.1.2 Sample pretreatment

A general experimental requirement in surface science is an UHV environment as mentioned earlier 2.1.1. To perform a reproducible series of measurements, the initial sample cleanliness as well as the affecting gas mixture have to be controlled. Also the temperature of the sample has to be monitored and controlled during the experiments. Before mounting the sample into the UHV chamber, it undergoes a set of pretreatments like pressing, mechanical polishing, chemical etching, rinsing in organic solvents, etc. However the final preparation, in order to achieve an atomically clean surface, can only be performed textitin situ, in UHV.

2.1.2.1 Temperature control and regulation

A crystal surface can be cleaned e.g. by annealing. This heating process can be realized by passing electrical current through the sample (FEM/FIM setup) or through electron bombardment (PEEM/XPS setup). At reasonable high temperatures adsorbed species and even surface oxide can be removed. The limit of this process is the melting point of the investigated crystal surface, since it can differ from the materials bulk properties due to the premelting effect. Also possible unwanted phase transitions have to be avoided. A drawback of such a procedure is the temperature dependent spreading of surface contamination and segregation of impurities from the bulk to the surface. Annealing can also be applied to restore the surface´s crystallographic order, considering the above objections. It is apparent, that the measurement of the sample temperature has to be done *in situ*. In the present setups, a thermocouple Ni/CrNi type K is spotwelded directly to the samples and the signal can be processed using a multimeter with the according software. The type K thermocouple covers the required temperature range (270 *to* 1640 K) and fulfills the precision (< 1 %) needed for experiments.

2.1.2.2 Controlling the reaction atmosphere

In situ chemical processing requires reactive gases at low pressures introduced through a leak valve into the vacuum chamber. Oxygen gas provides an oxidizing atmosphere whereas hydrogen and carbon monoxide provide a reducing atmosphere. The use of ionization gauges and of a residual gas analyzer allows monitoring of the gas composition throughout the sample pretreatment process. The PEEM-XPS setup uses the combined Pirani and cold cathode pressure gauge (PKR 251, Compact FullRange^{TM} Gauge, Pfeiffer Vacuum) and a spinning rotor gauge (Viscovac, Leybold) to measure the total pressure

of individual chambers (Fig. 2.2). Quadrupole mass spectrometers (e-Vision 2, MKS Spectra Products) are mounted in chamber A and B for residual gas analysis. During PEEM experiments, the valve connecting the PEEM electronic lens system to chamber A is closed and differential pumping realized. A Bayard-Alpert type hot cathode ionization gauge measures the pressure within the PEEM. The FEM/FIM setup uses two Bayard-Alpert type hot cathode ionization gauges and a spinning rotor gauge (Viscovac, Leybold) (Fig. 2.1) to measure the total pressure. A combined Pirani and cold cathode pressure gauge (PKR 251, Compact FullRange^{TM} Gauge, Pfeiffer Vacuum) is used during experiments. A quadrupole mass spectrometer (Quadrex 200, INFCON) measures the partial pressures. In both experimental setups, mounted ion getter pumps are able to measure the pressure through their ion current. The established pre-vacuum, in order to run turbomolecular pumps, is controlled by thermal conductivity Pirani gauges (ThermoVac, Leybold).

2.1.2.3 Sample cleaning

The use of heat and chemical treatments is often not sufficient to remove the surface contamination in order to establish a crystallographically defined and clean sample surface. Different techniques may be used to further clean the surface. The ion sputter gun enables bombardment of the surface with noble gas ions (typically, Ar^+). An ion beam is produced by introducing Ar gas through a leak valve into an electron gun. There argon ionization takes place by electron impact and formed Ar^+ ions are extracted and accelerated by high voltage ($\geq 1\ kV$) towards the sample. The Ar^+ ion and the sputter current can be measured between the bombarded sample and electrical ground potential. An annealing process, to restore the surface order, is usually applied afterwards.
The field ion microscopy technique provides in addition an unique way of surface preparation, namely field evaporation. A high electric field applied to the conducting specimen may cause the desorption of surface species (field desorption) including removing of the native surface atoms of the sample (field evaporation). Increasing the field strength in small steps, a controlled field evaporation process forms the shape of the tip apex towards a hemispherical geometry. The process can be followed *in situ* by field ion microscopy (section 2.2.3).

2.2 Point-projection microscopies

In 1937 Erwin Müller invented the field emission microscope (FEM) and since then the technique evolved and became a well established tool in surface science [49]. Like other microscopy techniques it is used to produce magnified images of the sample surface. The operational principle is based on the high electrostatic field applied to the metal tip surface, enabling, in turn, the tunneling of electrons (section 2.2.1). The field ion microscope (FIM) was the method, that enabled Müller to see surface atoms for the first time [50] using the noble gas ions for imaging (section 2.2.3). In both cases the nm-sized apex of a specimen-tip is projected to a screen cm away from the specimen, i.e. the FEM/FIM devices are point-projection microscopes.

2.2.1 Field emission microscopy

Already in 1928 Eyring, Mackeown and Millikan observed an electric current between a metal tip cathode and the anode when a voltage in the order of kV was applied [51]. The experiments were performed in high vacuum conditions and although it was already assumed, that the applied high electrostatic field was the driving power behind the observed phenomenon, it could not be explained with the physical model of the time though. In the same year Fowler and Nordheim established a theory explaining the observed current by consideration of the new quantum theory of condensed matter [52]. The process was called field emission and is schematically shown in Fig. 2.3a. Electrons with an energy close to the Fermi level can tunnel through a barrier, whose width is defined by the applied field and is in the range of the electron wavelength. The occurring field emission electron flux is related to the electric field strength and the work function as discussed in detail below (section 2.2.2).

In 1936 Johnson and Shockley reported the construction of a new and simple electron microscope for filaments [53]. They installed a round metal wire in the axis of a glass tube coated with a fluorescent layer on the inside, which had a helical nickel wire inlay. At a potential of 10 kV on the nickel wire they observed an emission pattern, due to cold emission, on the tube wall. The regular visible dark and white stripes represented in some way the wire crystal structure.

In the same year Müller performed first experiments to determine the work function of tungsten using cold electron emission [54]. For this a tungsten tip should have been

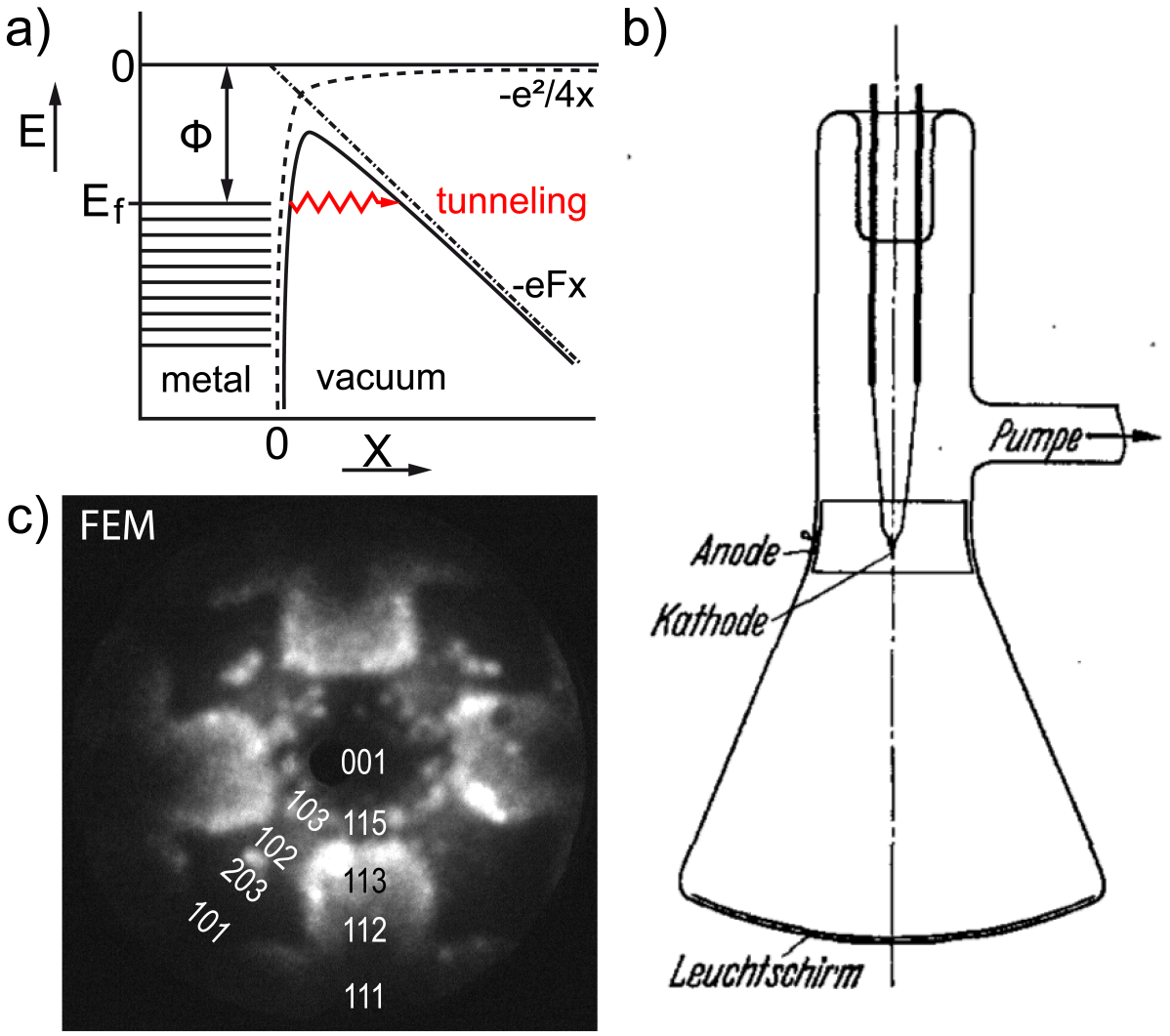

Fig. 2.3. a) Potential energy diagram for electrons (solid line) at the distance X from the metal surface. The imaging potential and the electric field are represented by dotted lines. b) First published layout of the field emission microscope in a glass tube. The cathode (tip), the anode, the fluorescent screen and the direction to the pump are labeled. Taken from Ref. [49]. c) FEM image taken from a rhodium curved crystal during an ongoing hydrogen oxidation reaction. The (001) centered pattern shows fourfold symmetry attributed to the face centered cubic lattice type. Anisotropy in the imaging contrast represents different crystallographically oriented facets labeled by the corresponding Miller indices.

prepared and the author already noted, that an etching and polishing process would have been necessary to build an uniform apex. In 1937 Müller was able to create such a tip and reported a radius of curvature of 1 µm [55]. Müller was able to observe the spatial distribution of electrons emitted from such a tip with a newly constructed field emission microscope. The corresponding experimental setup can be seen in Fig. 2.3b.

The tip was placed in front of a fluorescent screen at a distance of 10 cm. The glass tube was evacuated and a conducting gold layer burned into the glass was used as an anode. At anode voltages of several kV, electrons are emitted following the force lines of the electric field, with the field gradient being perpendicular to the sample surface. The point projection of a hemispherical tip to the screen allows highly magnified images with a resolution of 2 nm. The symmetrical patterns on the screen show dark areas and bright areas of high electron intensity (Fig. 2.3) The observable symmetries are a direct consequence of the crystal unit cell. The concept of stereographic projection allows crystallographic indication of the tip surface (section 1.3.3). The emission intensity of different crystallographic orientations is governed by the work function of corresponding facets depending on its atomic roughness in accord with the Smoluchowski theorem [56].

2.2.2 The Fowler-Nordheim relation

Already in 1928 Fowler and Nordheim derived quantum-mechanically the equation describing the current density j of electrons, tunneling through a field deformed potential barrier to escape the metal.

$$j = \frac{1.54 \times 10^{-6} F^2}{\phi t^2(\xi)} exp \left[\frac{-(6.83 \times 10^7 \phi^{3/2} f(\xi)}{F} \right] \quad [A/cm^2] \tag{2.1}$$

Where F is the applied field in V/nm, ϕ is the metal work function in eV and $f(\xi)$ and $t(\xi)$ can be treated as material constants of unity to receive the so-called elementary Fowler-Nordheim-type equation [57].

2.2.3 Field ion microscopy

In 1941 Müller discovered that, when the field is at a certain particular strength, some adsorbed atoms on the surface are ruptured from the surface, ionized and accelerate towards the screen [58]. The phenomenon is called field desorption and is used to remove adsorbed species for cleaning purposes (section 2.1.2.3). The original sample surface sites of generated ions are point projected to a screen but at the time image intensification could not be achieved. In 1951 Erwin Müller constructed the field ion microscope (FIM) by establishing a channel plate image intensifier and increased the resolution of his point projection microscope [50]. The apparatus is similar to the FEM and includes a sharp tip together with an fluorescent screen placed in a glass tube. Hydrogen from an alcohol flame was introduced into the gals tube at a pressure of 8×10^{-3} $mbar$. At a field strength

of about 15 V/nm on the tip apex the contours of its lattice steps could be observed. Neutral gas phase molecules are polarized and thus attracted to the tip surface by an inhomogeneous electric field around the tip apex. Müller supposed that hydrogen would first adsorb on the apex and then field desorb as positive ions becoming thus the imaging species. In 1954 Inghram and Gomer stated that the polarized gas atoms first thermally accommodate by a series of hopping events with decaying distance (Fig. 2.4b) [59]. The

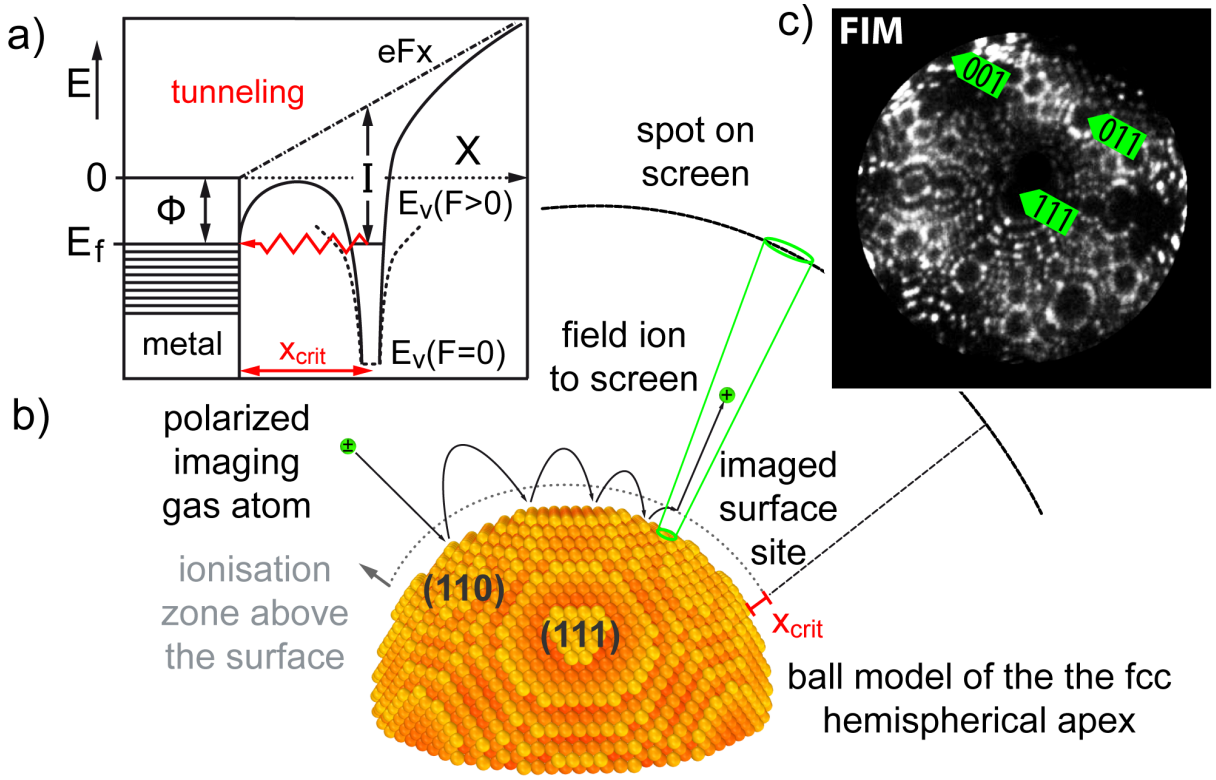

Fig. 2.4. a) Potential diagram of the field ionization of a gas atom close to the metal surface. At a critical distance an electron can tunnel from its energy level, elevated by an applied electric field in the atom to or above the Fermi level of the metal surface. b) Polarization of an individual gas atom in an applied electric field and its thermal accommodation to the surface temperature in a series of hopping events. In the ionization zone close to x_{crit} positive ions are formed above protruding sample atoms. The formed ions accelerate radially away from the surface. An imaged surface site is therefore visible as a spot on the screen. The magnification m is given by the ratio of radii of curvature (radius of hemispherical apex R and radius of screen D) and a geometrical factor β ($m \equiv D/\beta R$). c) The projected FIM micrograph of an (111) oriented rhodium nanotip shows individual protruding surface atoms. The surface atoms form facets of different crystallographic orientation and their areal arrangement converges a hemisphere shape.

field ionization of a volatile species is most likely to occurs in close proximity to the metal surface, when the DeBrolige wavelength of the tunneling electron is in the dimension of the potential barrier width. This critical distance ($x_{crit} = (I - \phi)/F_0$, Fig. 2.4a) is

dependent on the applied electric field, which is strongest on spherical perturbations. In particular, above protruding apex atoms, the electron can tunnel from the gas atom to the metal above its Fermi level. The produced ion will accelerate radially away from the surface to the screen. In 1956 Müller and Bahadur used helium as the imaging species and were able to see protruding tungsten atoms at room temperature [60]. In the same year Müller used cryogenic temperatures to resolve individual atoms, forming concentric edges of facets [61].

2.2.4 FEM/FIM experimental setup

In the present contribution a stainless steel chamber including the FEM/FIM apparatus was used. As is already shown in Fig. 2.1 the desired gas atmosphere or UHV is achieved by an interplay of pumps and leak valves. A schematic layout of the FEM/FIM apparatus used by the author is depicted in Fig. 2.5. A tip specimen is mounted to the sample holder consisting of a manipulator with a cooling finger. A multichannel plate and a phosphorous screen generate the image, when using the experimental setup as a FEM. The multichannel plate works as a dynode single particle intensifier i.e. for electrons and ions with lateral resolution [62]. The impinging particle starts a cascade of secondary electron emission within one channel and the P20 covered screen converts the electron current density image into a visible image. In the case of the FIM three main requirements have to be applied.

1. The voltage applied to the tip is positive in respect to the counterelectrode.
2. An imaging gas is introduced in the chamber, usually a noble gas like He or Ne at a pressure of about 3.5×10^{-5} $mbar$.
3. The sample tip is cooled i.e. by liquid nitrogen to low temperatures to avoid thermal blurring due to crystal lattice vibrations.

The tip sample itself is spot-welded to an ark-formed (0.125 mm) tantalum wire. The ends are spot-welded to two tungsten bars. The tungsten bars act as electrical feedthrough and are integrated in the glass Dewar construction, a cooling finger, which is filled with liquid nitrogen during experiments to enable a sample tip temperature of about 77 K.
The methods require a potential of up to ±20 kV applied to the sample tip. Within the experimental setup isolation is ensured by the glass inset of the sample holder. Galvanic isolation of the experimental setup is necessary in respect to service facilities i.e. trafos. An isolating transformer is used for the potential decoupling of the heating current. The

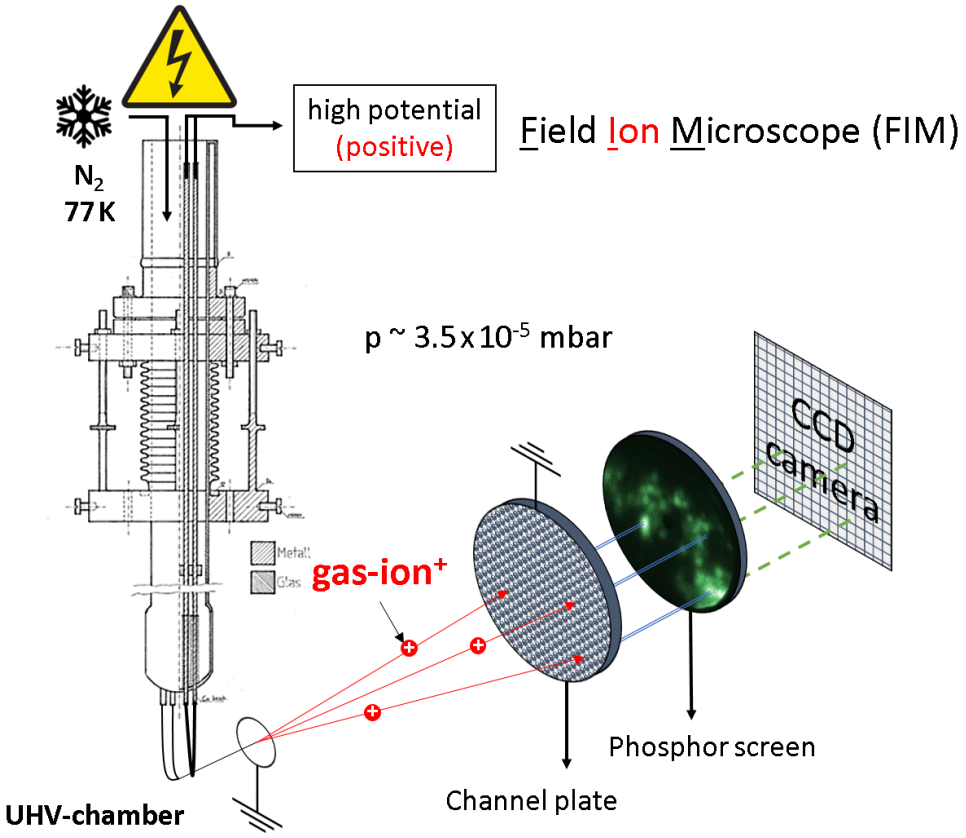

Fig. 2.5. The essential parts of the FIM experimental setup are shown and the requirements of the technique indicated. The phosphorous screen, the multichannel plate and the sample tip counterelectrode arrangement are installed inside the UHV chamber. The CCD-camera captures the screen through a viewport. The sample holder consists of a manipulator and a cooling finger with tungsten bar inlays. This setup provides electrical feed-through, sample fixation, cooling to 77 K and sample positioning. The imaging gas is introduced into the chamber at typically 3.5×10^{-5} *mbar*

thermovoltage generated by the type K thermocouple is translated into a signal transferred to the heating unit. The signal is either transmitted over an optical fiber or wireless. The latter has the benefit of using an analog to digital converter which allows direct integration of the thermovoltage into the processing software.

The sample tip positioning occurs by a manipulator with three screw axis. A movable counterelectrode serves as a focus device for the charged imaging particles and the electrical connection enters the UHV chamber on the bottom side of the chamber (Fig. 2.6b). A multichannel plate is set in front of the screen to increase the incoming electron (ion) flux. The potential applied to the multichannel plate is typically 2.2 kV in respect to the counterelectrode. A phosphorescence screen converts the arriving electrons into visible

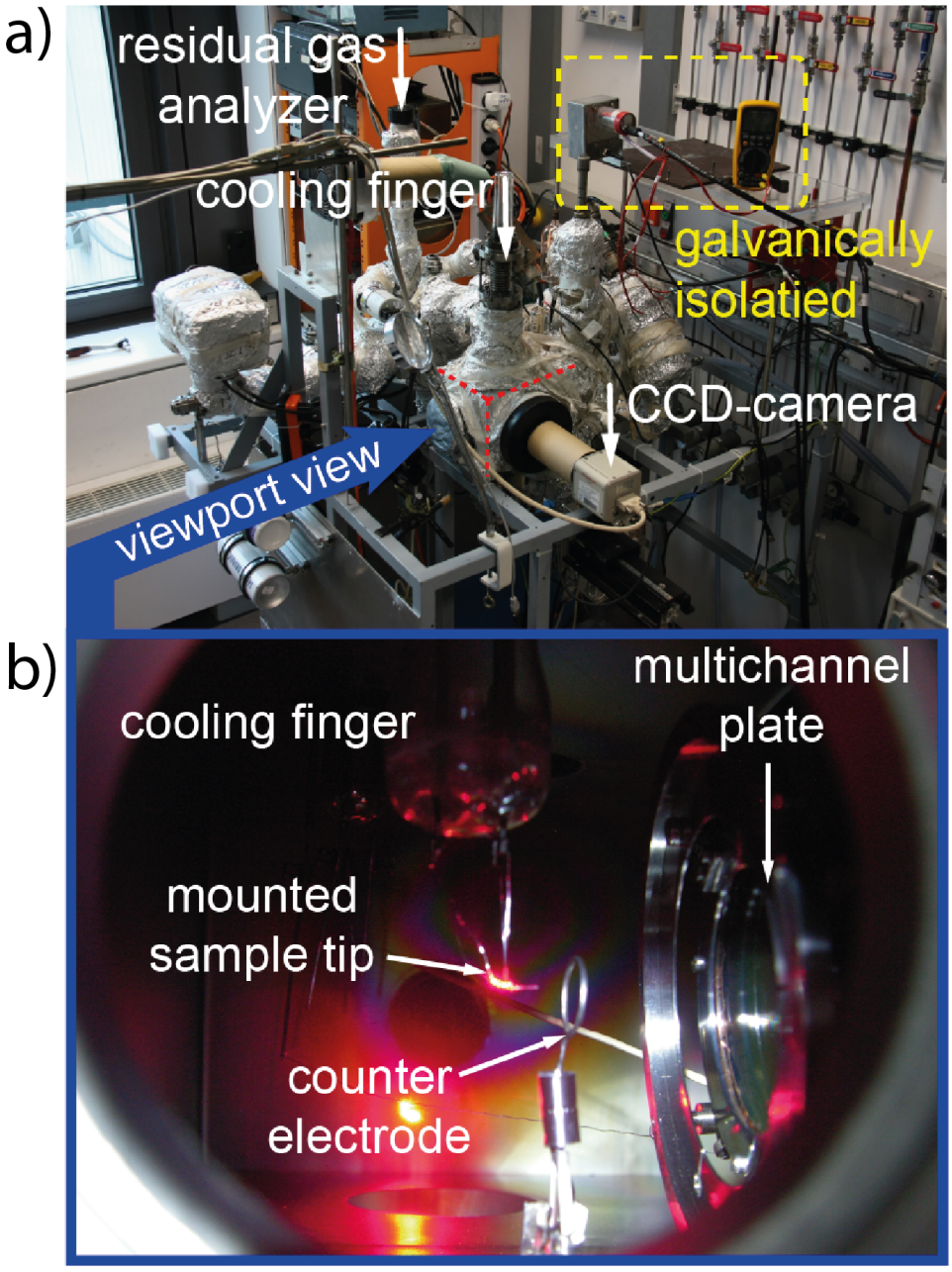

Fig. 2.6. a) Schematic overview of components of the FEM/FIM setup. Besides the main FEM/FIM chamber, the residual gas analyzer (quadrupole mass spectrometer (QMS)),the CCD-camera and the cooling finger are indicated. An isolating transformer is connected intermediary to the heating circuit and the thermovoltage is transmitted wireless to ensure galvanic isolation. The perspective of graph *b* is obtained through the indicated viewport. b) Image showing the inside of the UHV main chamber hosting the FEM-FIM setup, taken trough a viewport. The cooling finger, the sample tip, the counter electrode and the multichannel plate are visible.

contrast. The screen itself is put on a potential of about 1.38 kV in respect to electrical ground. A high speed CCD-camera (Hamamatsu Digital Camera 93000C) captures the screen pictures as a sequence of video frames.

2.3 Photoemission electron microscopy

In 1932 Brüche used an electrostatic lens system to image a heated cathode emitting electrons [63]. One year later Brüche used UV-light to irradiate the sample surface and generate photoelectrons [64]. The electrons were accelerated and focused by simple magnetic lenses and so the photoemission electron microscope (PEEM) was realized. Also in 1933 Johannson introduced the basis of the four electrode electrostatic lens system (tetrodes [65]), realized by Dücker almost 30 years later [66]. In the early 1980´s surface science was interested in PEEM and the just developed LEEM at TU Clausthal was also used as an UHV-PEEM system [67]. For pure PEEM studies a small flange-on PEEM was constructed by Engel [68]. It was commercially adopted by Staib instruments and used successfully at Fritz Haber Institute (FHI) in Berlin [69, 70].

The contrast of the PEEM is generated by the work function dependent emission of photoelectrons from a metal sample, surface itself or from any adsorbed chemical species. The technique is able to provide images with a lateral resolution within the low nm range and is capable to retrieve information from the whole region of interest in a parallel way, i.e. simultaneously. The development of the UHV-compatible PEEM layouts offer the possibility to witness *in situ* surface dynamic processes like adsorption, diffusion or layer growth, in principle any process accompanied by changes in work function. The visualization of oscillation surface reactions on single crystal surfaces, developed by Nobel laureate Gerhard Ertl is potentially the most known application of PEEM [71].

2.3.1 The photoelectric effect and working principle of the photoemission electron microscopy

In 1886 Hertz made first experiments with UV-light enhancing the traveling distance of sparks in an electric field dependent on the electrodes material [72]. His former assistant Hallwachs continued the research on this phenomenon and in 1888 Hallwachs formulated the hypothesis that a metal plate, which is illuminated by UV-light, is positively charged, because the electrons are forced out [73]. In 1905 Nobel laureate Albert Einstein (honored for his work 1928) clarified the phenomenon by delivering the proper explanation [74]. In his thesis the kinetic energy of a photoelectron is the direct result of the photon-electron interaction

$$E_{kin} = h\nu - E_B - \phi \tag{2.2}$$

where hv is the energy of a photon, E_B is the binding energy of the electron and ϕ is the work function, which varies dependent on the chemical composition of the sample, surface crystallography, adatoms, etc. A microscope can be constructed, that utilizes the photoelectric effect. The photoemission electron microscope generates its imaging contrast out of the photoelectron flux, which is dependent on the local work function of the studied surface. Even small lateral differences in the local work function can be resolved in this way. Low energy photons (i.e. Hg discharge lamp: $I_{max} \cong 4.9\ eV$) open up a narrow interval of a few eV for the photoelectrons kinetic energy. Such a photoelectron spectrum includes not only elastically scattered electrons but also secondary inelastically scattered electrons with lower kinetic energy. The spectral width $(hv - \phi)$ increases and so the photoelectron flux, when the work function is lowered at the sample surface resulting in a brighter image spot. Two UPS spectra, which were taken from two different regions, are depicted in Fig. 2.7a. The area with ϕ_1 represents the clean surface and on area with ϕ_2 an

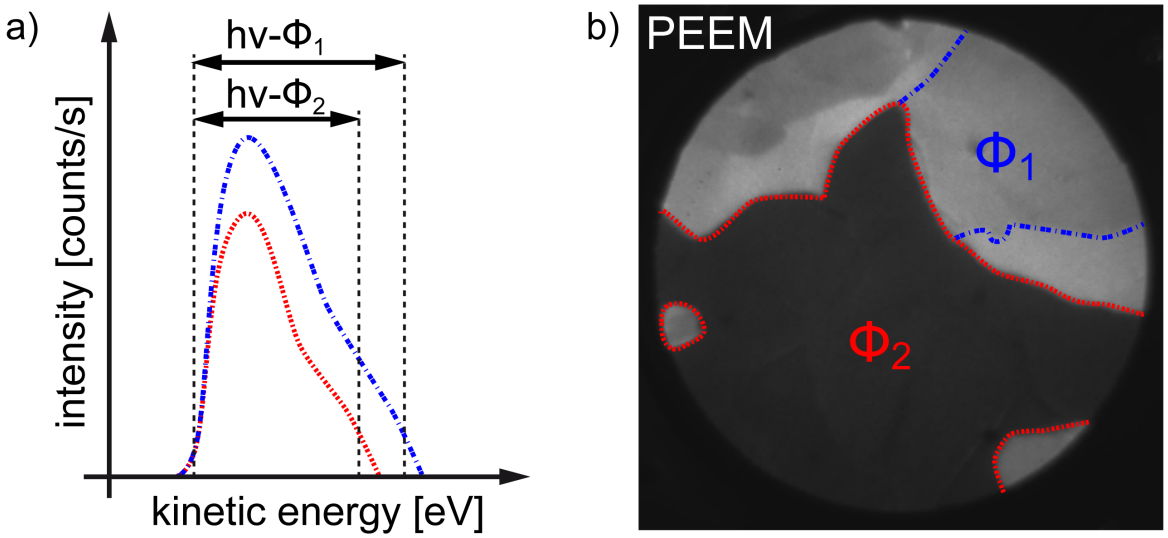

Fig. 2.7. Correlation of photoelectron spectra with a corresponding PEEM video frame: a) The width of the photoelectron spectra is dependent on the work function. A higher work function area emits lesser photoelectrons with reduced kinetic energy. b) The PEEM video frame has a contrast dependent on the work function. Bright areas (ϕ_1) correspond to a low work function area and dark areas (ϕ_2) correspond to a higher work function area.

electronegative species is adsorbed. The adsorbate increases the work function ($\phi_2 \geq \phi_1$) and therefore the spectral width is reduced and the total photoelectron flux is smaller. The generated contrast can be used to picture e.g. catalytic reactions where inhomogeneously adsorbed chemical species induce local work function changes. The imaging optics use an

electrostatic lens system that accelerates, deflects, focuses and decelerates the electrons onto a multichannel plate, which amplifies the signals while conserving lateral resolution (Fig. 2.10). A phosphorous screen converts the electron flux into a visible image that is captured with an CCD-camera. The latency of the phosphorous screen and the frame rate of the camera determines the temporal resolution.

2.3.2 X-ray photoelectron spectroscopy

In 1907 Innes performed experiments with a Roentgen tube and a magnetic field hemisphere, working as an kinetic energy analyzer for electrons. He was able to record a first spectrum of the electron intensity as a function of their velocity [75]. Siegbahn improved the method and in 1956 he published the first high energy resolution spectrum [76]. Further development of the technique, called electron spectroscopy for chemical analysis (ESCA), also got great attention in the field of surface science [77] and resulted in the Nobel price awarded in 1981 [78].
Today X-ray photoelectron spectroscopy (XPS) is a widely spread technique used in surface science to obtain chemical information from the surface layers. The method relies on the photo effect discussed in section 2.3.1. In XPS high energy radiation, namely X-rays, are used to generate core level electron exaltation of the sample atoms (Fig. 2.8).
A conventional laboratory X-ray source produces a characteristic spectrum depending on the used secondary target. Usually the Mg-K_α-line (1253.6 eV) and the Al-K_α-line (1486.6 eV) provide enough intensity and have a narrow enough peak width for chemical analysis. The emitted photoelectrons are measured in respect to their kinetic energy, plotted in a typical XPS spectrum. The kinetic energy of photoelectrons is measured with a hemispherical analyzer in dependence of the analyzers Fermi energy. The Fermi energy of the analyzer is related to the Fermi energy of the sample by a certain voltage (U). The kinetic energy of electrons measured by the analyzer is then given by

$$E_{kin,analyzer} = h\nu - E_B - eU - \phi_{analyzer} \ . \tag{2.3}$$

The hemispherical analyzer consists of two concentric hemispheres, a lens system and an electron detector. A voltage is applied to both hemispheres (Fig. 2.8) so that only photoelectrons of a certain pass energy reach the detector. The analyzer operates usually in constant analyzer energy (CAE) mode, where the pass energy is held constant and the transfer lens system retards the kinetic energy of photoelectrons to the range accepted by the hemispherical analyzer.

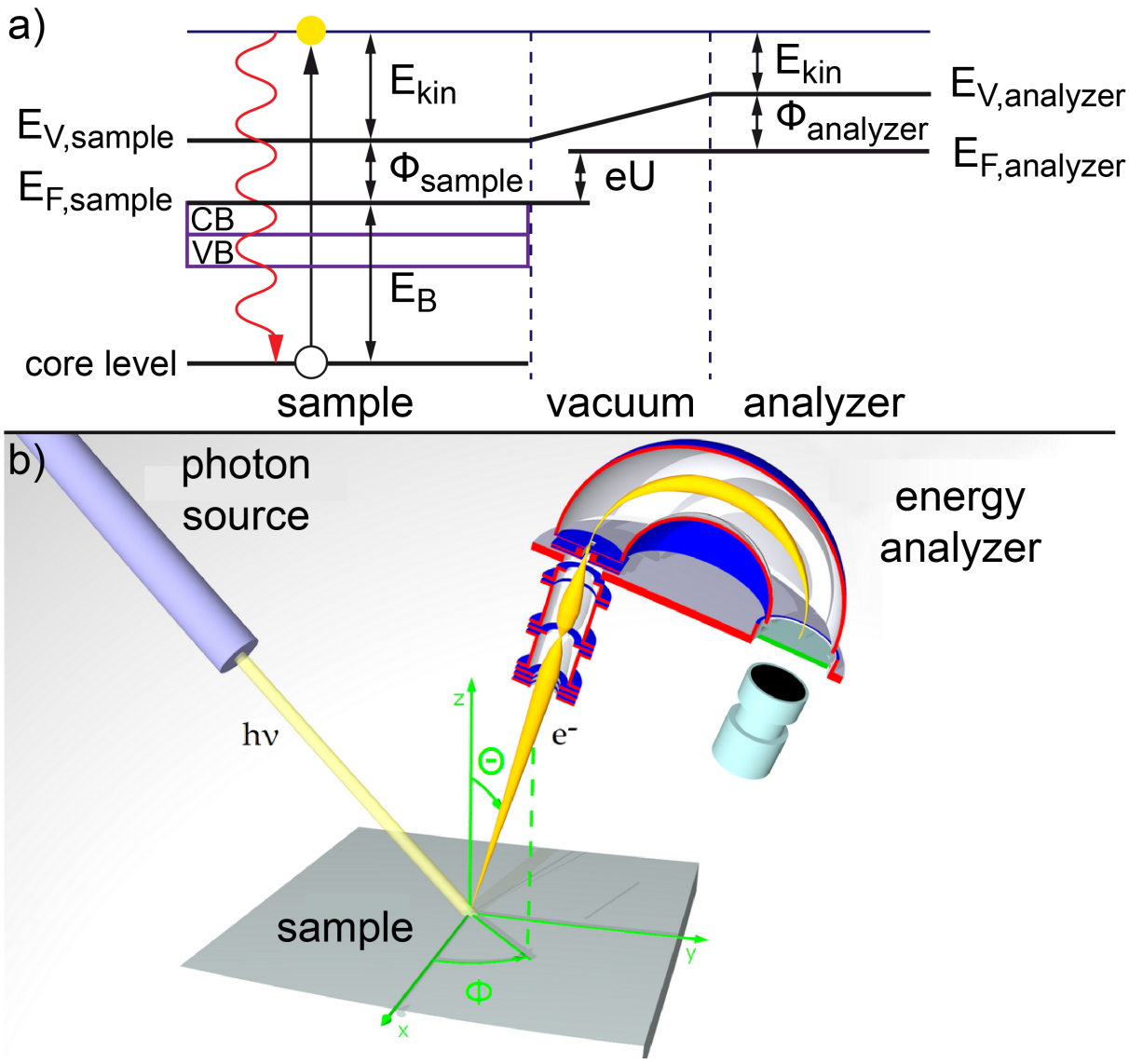

Fig. 2.8. a) Energy levels in XPS. The kinetic energy of the photoelectrons is measured with respect to the Fermi level of the analyzer. b) Schematic cross section through a concentric hemispherical analyzer.

Two highlights mark the unique position XPS holds in surface science as a spectroscopic method. Firstly this technique is able to register changes in the electronic surface structure. A so called *chemical shift* for binding energy lines in the spectrum can be noticed upon a change in the chemical surrounding of the probed atoms. On the other hand XPS is a surface sensitive technique due to the inelastic mean free path of electrons. The information depth is maximized, if the sample surface is normal to the analyzers lens system and can be reduced by tilting the sample.

2.3.3 PEEM/XPS experimental setups

The PEEM is installed inside the microscopy chamber *A* of the multifunctional UHV-system (Fig. 2.9). The main components are a UV-source, a sample holder, an electro-

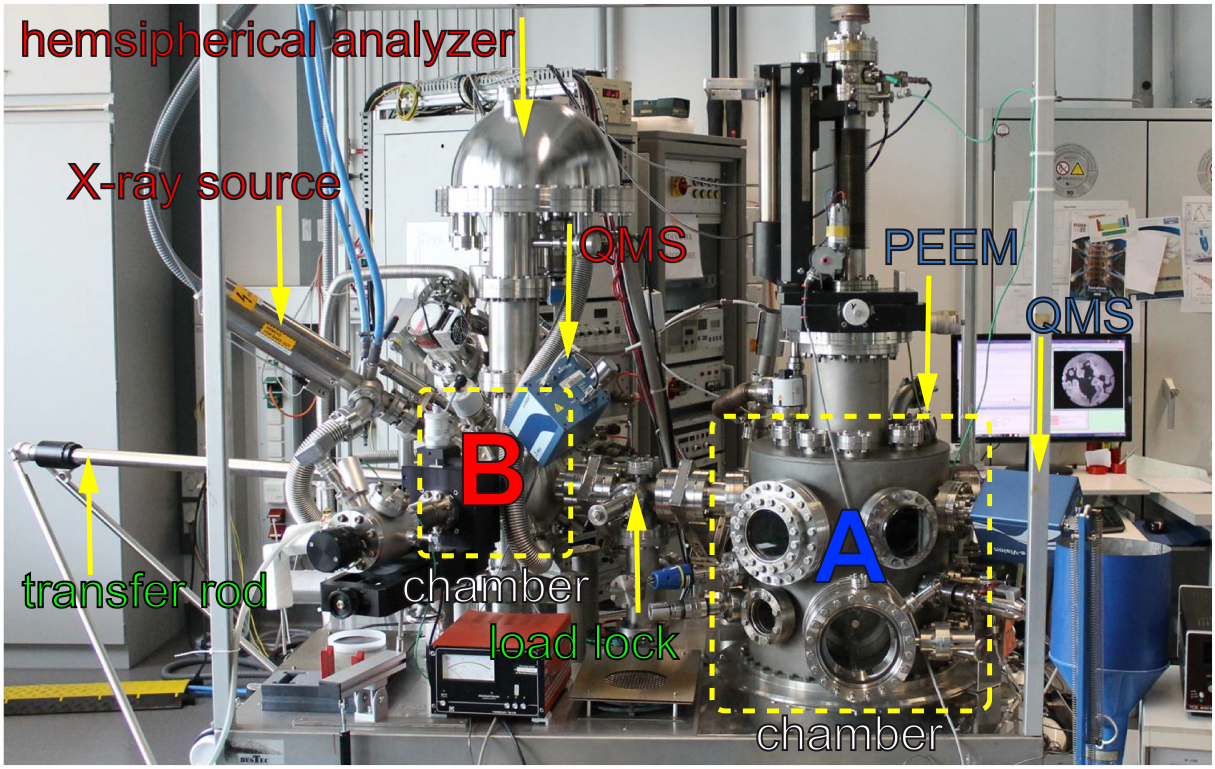

Fig. 2.9. The PEEM/XPS system. The microscopy chamber *A*, the spectroscopy chamber *B* and visible process equipment are labeled.

static lens system and an electron detector. The water-cooled deuterium UV-lamp (D200, Heraeus) has a cut-off energy of 6.8 eV and is used as excitation source, illuminating the sample through a viewport under an incidence angle of about 75°. The sample holder is attached to a manipulator having five degrees of freedom. This allows positioning of the sample perpendicular to the PEEM entrance cone. The distance of the entrance cone to the sample surface is about 3 to 5 mm and photoelectrons, which are released near ground potential, are accelerated towards the cone by a transfer voltage of 15 keV. The PEEM-150 (Staib Instruments) consists of four lenses leading the electrons towards a multichannel plate. The image column of the PEEM uses basically the first three of them. The individual lenses are each arranged one after another and serve a distinct purpose as listed below and in Fig. 2.10.

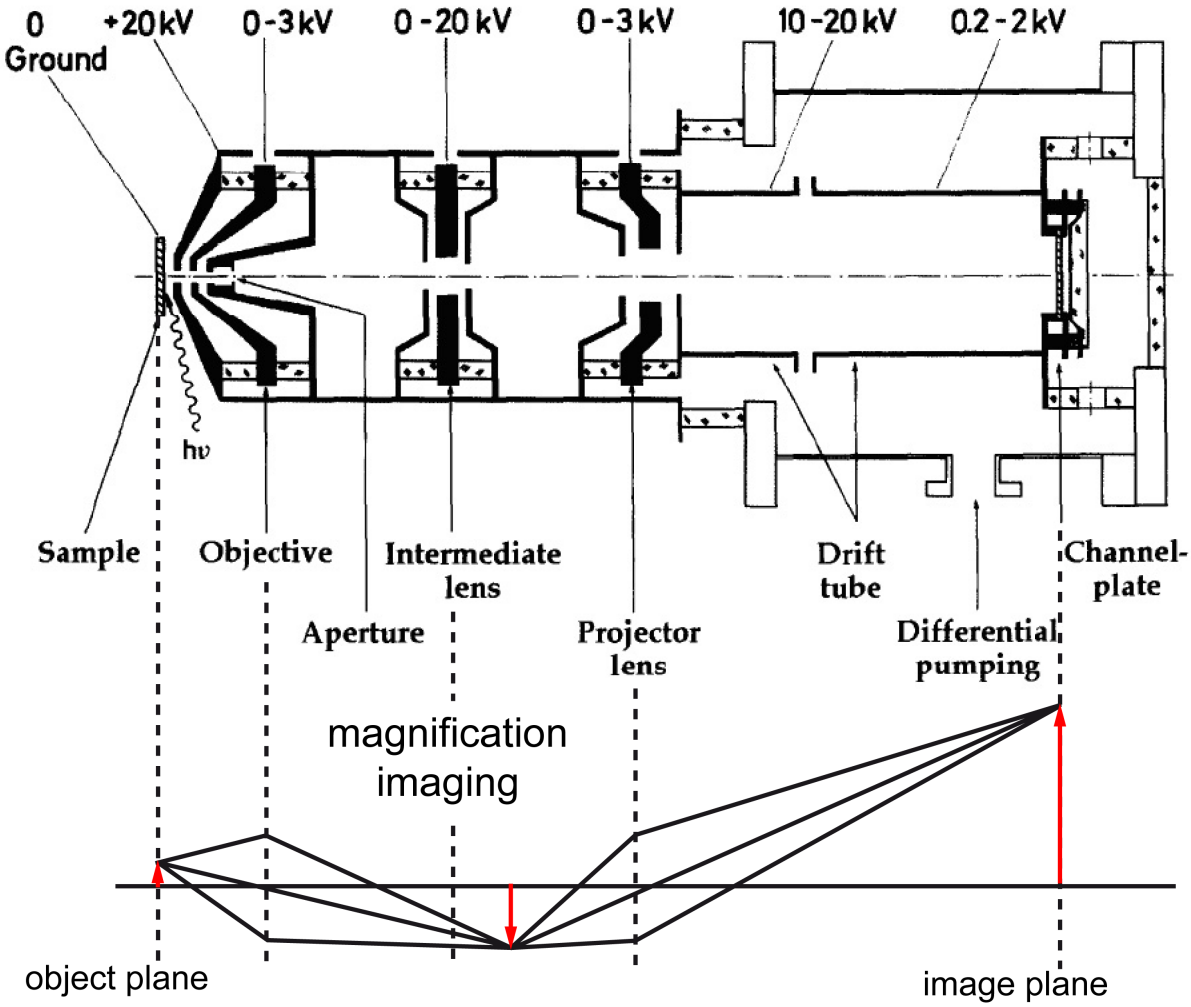

Fig. 2.10. Schematic cross section of the PEEM used in the present work adopted from Ref. [78]. The image magnification in the PEEM imaging column consists basically of three imaging lenses.

1. The objective lens (applied potential 3.3 kV) forms the first magnified image from the object plane to the backfocal plane.

2. The intermediate lens (applied potential 10 kV) forms a virtual intermediate image since the potential is near transfer voltage.

3. The projective lens (applied potential 1.58 kV) magnifies a second time to the image plane.

4. The decelerating lens (applied potential 1.25 kV) reduces the photoelectrons kinetic energy.

The focused photoelectrons form the magnified image on a microchannnel plate detector, which works as an image intensifier. Reduction of the kinetic energy is necessary, because the multichannel plate, with a gain voltage of 800 V, can process impinging electrons with kinetic energy between 200 and 2000 eV. The electron beam coming out of the multichannel plate gets accelerated towards the phosphorous screen by a voltage of 3 kV. The high speed CCD-camera (Hamamatsu Digital Camera C11440) captures an image series with temporal resolution down to the low µs range.
The XPS is located in the chamber *B* of the UHV-setup (Fig. 2.2) and the main components are a water-cooled X-ray source (XR 50, SPECS), a sample holder (Standard LN2, SPECS), a hemispherical electron analyzer (Phoibos 100, SPECS; Fig. 2.8) and a detector consisting of a multichannel plate with a 2D-CCD detector. The axis of the hemispherical analyzer, starting at the entrance slit prolonged through its lens system, has an off-axis angle of 54.7° in respect to the axis of the X-ray beam.

2.4 Additional surface techniques

In the present work, the rhodium samples were previously analyzed at the Service Center for Transmission Electron Microscopy of the Technische Universität Wien (USTEM). A scanning electron microscope (SEM) was used to provide a high resolution image of the Rh curved crystal sample. The polycrystalline Rh foil was probed with the electron backscatter diffraction (EBSD) technique to determine the crystallographic orientation of surface domains.

2.4.1 Scanning electron microscopy

The scanning electron microscopy (SEM) technique uses an electron beam of energy from 1 to 10 keV which is focused by a lens system onto the sample surface. The diameter of the beam can be as small as 1 nm. Deflection coils can move the beam in a raster across the surface, and simultaneously by the same scan generator an electron beam in a video tube is moved across the screen. The magnification results from the size ratio between the display and the scanned surface area of the sample. Different types of signals can be detected, resulting in various modes of operation. The secondary electron mode collects low energy secondary electrons by a directional detector. The topography of the sample gets revealed, since the secondary electron yield is strongly angular dependent and shadowing effects appear [79].

2.4.2 Electron backscatter diffraction

Electron backscatter diffraction (EBSD) allows structural identification of a crystal formation. The technique requires a SEM with a mounted EBSD detector. The electron beam is focused on the sample surface and some of the impinging electrons can backscatter and leave under a certain angle to undergo subsequent scatter events [80]. The scattered electrons can perform elastic diffraction on lattice planes. If the angle fulfills the Bragg condition for a certain lattice plane, interference forms a diffraction pattern. The sum of diffraction forms a pattern of Kikuchi bands, which represent intersections and paths between the lines in orientation space. If the sample crystallographic system is known, individual bands can be related to the Miller indices of the diffracting lattice planes [81]. The process software compares obtained images systematically, using crystal data libraries to perform indexing. At least three intersecting bands need to be characterized to reveal the crystal orientation of the probed domain. The technique enables the crystallographic characterization of micro structures within the sample [82].

2.5 The rhodium samples

In the present work the hydrogen oxidation reaction on three different Rh-samples was studied: 1) a Rh tip with a radius of curvature of about 25 nm with an apex exposing differently oriented facets; (2) the curved Rh crystal with a hemispherical apex that has a diameter of about 1.3 µm; (3) a polycrystalline Rh foil consisting of differently oriented crystalline grains, forming domains of several µm size. The Rh samples can be ordered according to their size as shown in Fig. 2.11. All samples were prepared to fulfill the experimental requirements and the applied methods restriction.

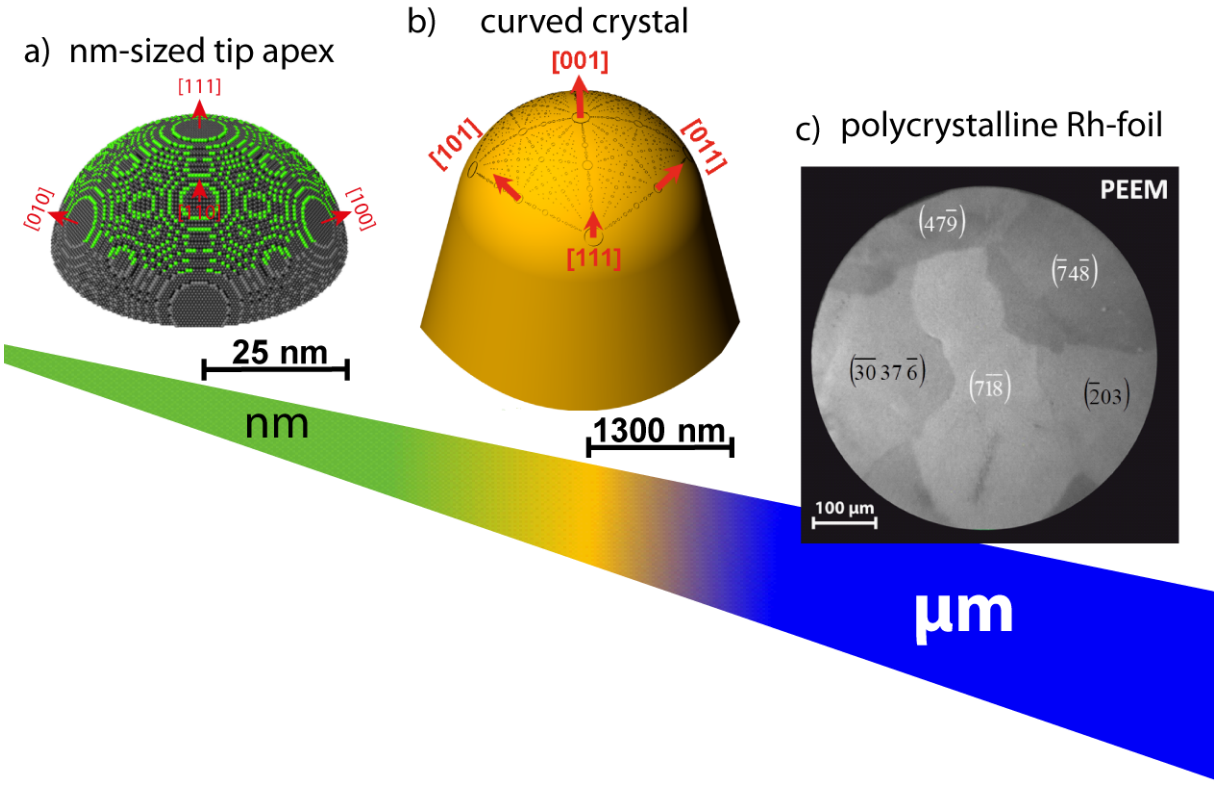

Fig. 2.11. Three different Rh samples ordered along the size axis: a) a nm-sized apex of a nm-sized Rh tip with a radius of curvature of 25 nm with an [111] orientation represented by a ball model; b) a µm-sized curved crystal with a diameter of 1.3 µm; c) a polycrystalline Rh foil consisting of µm-sized grains with different crystallographic orientations.

2.5.1 Nm-sized rhodium specimen

The nm-sized Rh sample is a sharp needle-like specimen prepared to have a hemispherically shaped apex with a radius of curvature of 25 nm as schematically shown in Fig. 2.12.

From a piece of pure Rh wire (purity 99.99 %, MaTecK) a preliminary specimen was sharp-

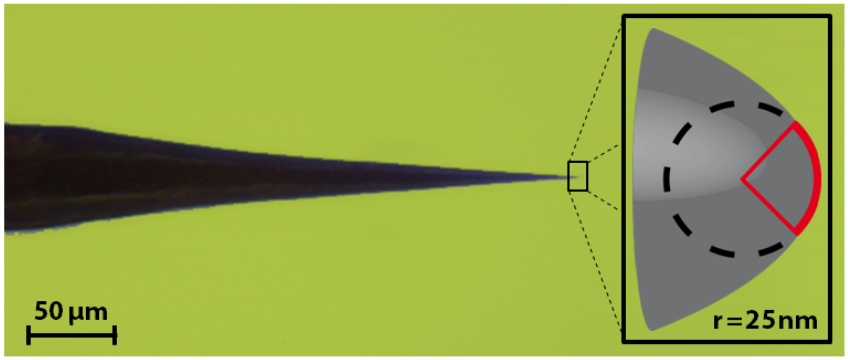

Fig. 2.12. Optical image of the nm-sized Rh specimen. The cuspid shape is achieved by electrochemical etching. The apex of the tip has a hemispherical form with a radius of curvature of 25 nm.

ened by electrochemical etching. For the etching process an eutectic mixture of NaCl and $NaNO_3$ has been melted and a voltage of about 5 V was applied between the molten salt mixture and the Rh wire to initiate the current and an electrolytic removal of Rh atoms. To observe the sharpening an optical microscope was used after each etching cycle. The prepared specimen was spotwelded to the sample holder (section 2.2.4) and cleaned with an organic solvent. In order to create an apex with a nearly ideal hemispherical shape on the atomic scale, field evaporation, performed in the field ion microscope setup, was used as described in section 2.1.2.3. The removal of protruding surface atoms by a strong electrostatic field established an ordered pattern of facets shown in Fig. 3.1. This hemispherical surface was reestablished before every catalytic experiment.

2.5.2 µm-sized curved rhodium crystal

Similarly to the nm-sized Rh specimen a µm-sized curved Rh crystal was fabricated. As basis a Rh tip was produced by means of electrochemical etching as described above. The fabricated specimen was spotwelded to the sample holder and transferred to the FEM/FIM UHV setup. A shaping process was developed to form the curved crystal (Fig. 2.13): a combination of chemical processing and high temperature annealing. The annealing was performed at 1590 K, followed by heating in an oxidizing atmosphere. Therefore the surface was exposed to 1.33×10^{-7} *mbar* of O_2 in the time span of 60 s at a temperature of 1590 K. The next step involved H_2, dosed at 1.33×10^{-7} *mbar* for 60 s at a temperature of 1200 K. The last step was a fast temperature flash at about 1600 K which rendered the surface in a clean, absorbate free state. The sample holder was cooled by

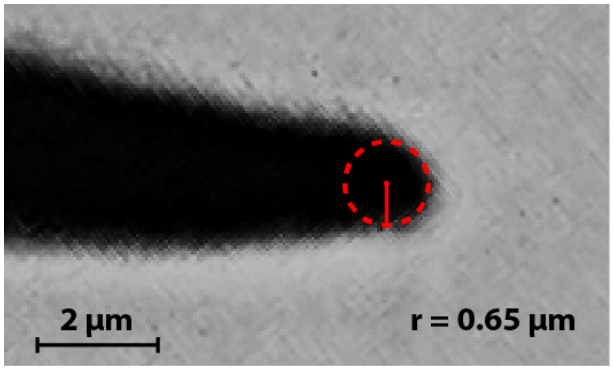

Fig. 2.13. Optical image of the µm-sized Rh curved crystal. The cuspid shape is achieved by annealing and chemical processing. The apex of the tip has a hemispherical form with a radius of curvature of about 0.65 µm.

liquid nitrogen during the cleaning process to guarantee an almost instant cooling after a high temperature annealing step. After each shaping cycle the tip was imaged with FEM and an increase of the required imaging potential towards a constant value indicated that the equilibrium shape for the applied conditions was achieved.

2.5.3 Polycrystalline rhodium foil

A rectangular peace of a polycrystalline rhodium foil (10×12 mm^2, purity 99.99 %, MaTecK) with a thickness of 0.2 mm, was fixed onto a sample holder plate. Figure 2.14 shows the sample holder arrangement with the K type thermocouple attached to the Rh foil and two isolated electrodes for the transmission of the temperature signal. The

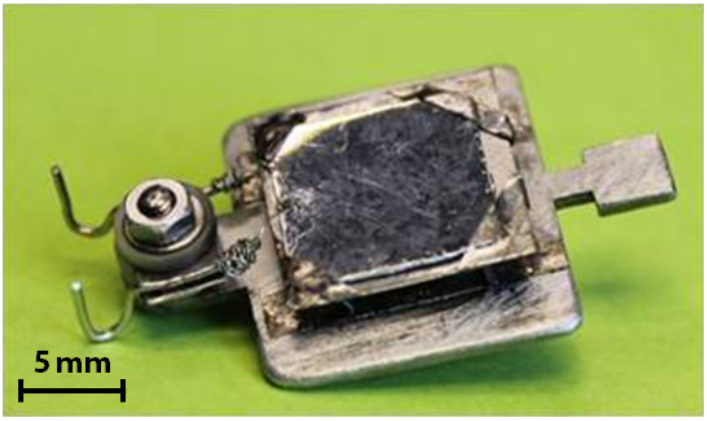

Fig. 2.14. The polycrystalline Rh foil is mounted to the sample plate. The type K thermocouple wires (NiCr/Ni) are attached to the Rh foil and two isolated contact electrodes.

flat surface was prepared by pressing, polishing and rinsing with organic solvent. The

sample was transferred into the PEEM-XPS setup through the loadlock, where it could be cleaned in UHV as described in section 2.1.2.3. The UHV cleaning process involved Ar^+ sputtering, annealing, and chemical processing with oxygen. The sputtering with Ar^+ ions at 1 keV was performed at 300 K and was followed by annealing to 973-1073 K for 30 min. To remove carbon impurities an additional chemical processing with oxygen at 773 K was performed until the XPS spectrum confirmed the absence of environmental carbon. The survey XPS spectrum of the clean Rh foil is shown in Fig. 2.15. An XPS

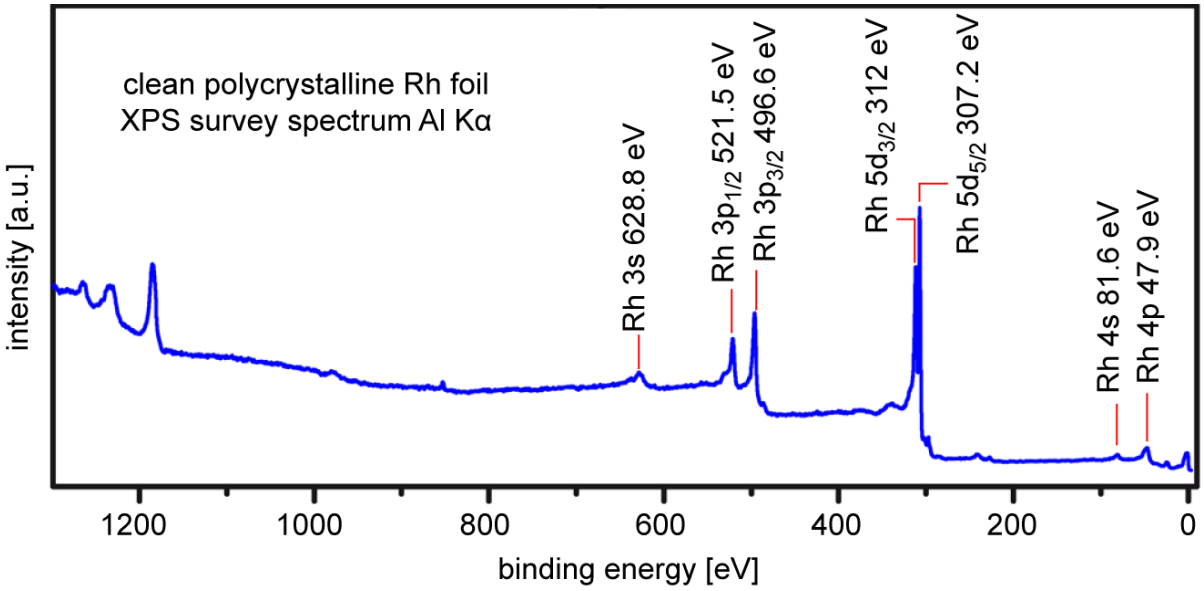

Fig. 2.15. XPS survey spectrum of the clean polycrystalline Rh foil. The characteristic Rh peaks are labeled.

control of the Rh foil was performed before every experiment to assure the cleanness of the sample surface.

3

Results

3.1 Nanometer-sized Rh tip

The nm-sized Rh tip, introduced in section 2.5.1, was imaged by FIM and characterized (section 3.1.1) using the atomically resolved FIM micrographs. The hydrogen oxidation reaction on this specimen was studied using FEM. The kinetic phase transitions between two steady states of the catalytic H_2 oxidation reaction were studied in a temperature range of 413 to 493 K. The catalytic behavior could be summarized in a kinetic phase diagram described in section 3.2.3 and kinetic transitions at 413 K are additionally discussed in detail in section 3.2.3.

3.1.1 Identification of the Rh tip crystallography

3.1.1.1 FIM micrographs with atomic resolution

As already mentioned in section 2.2 the FIM is a point projection microscope able to image the surface of a specimen on the atomic scale. Figure 3.1 shows a FIM micrograph of a nm-sized Rh tip apex. Since individual Rh atoms are visible in the micrograph, the geometry of the nm-sized facets formed on the surface can be directly observed. The three-fold symmetry in a fcc crystal system is characteristic for the {111} oriented facets. Other low Miller index facets were identified considering the symmetry within the Rh fcc crystal system. The {110} oriented facets have two symmetry axes: (i) The axis between two {111} oriented facets which is seen as a straight alinement of stepped facets in the FIM image (Fig. 3.1) and (ii) the axis connecting the {001} oriented facets which is seen as a curved line in the stereographically projected image in Fig. 3.1. The {001} oriented facets are located on the border of the field of view and exhibit four symmetry axes. Regions with facets consisting of pure stepped surfaces are located along the connecting lines between the main low Miller index poles. Rough surfaces with a high kink density are formed between the lines. A suitable ball model was constructed and is explained in the section below.

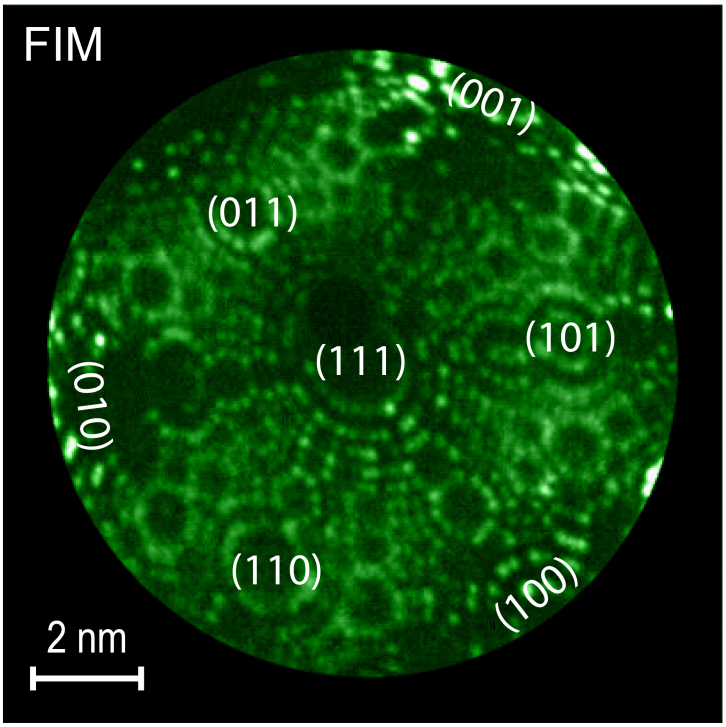

Fig. 3.1. Identification of the crystallography of a Rh nanotip: FIM micrograph of a clean (111)-oriented Rh tip imaged with Ne^+ at 77 K and at an applied field of 35 V/nm. Main low Miller index facets are labeled.

3.1.1.2 Ball model

Since the FIM images mainly the protruding surface atoms, the construction of a ball model is a helpful method to reveal the position of all atoms forming the tip apex [83]. It is assumed that the apex has a hemispherical shape which is a close approximation for most transition metal specimens [84, 85]. For the modeling of the tip, the radius of the hemispherical tip apex has to be determined. The radius of tips with a hemispherical apex bigger than 5 nm is usually estimated by the "ring counting method" [86]. As Fig. 3.2a shows schematically, two crystallographically identified poles, facets having the Miller indices [hkl] and [h'k'l'], on the apex surface are separated by the angle ϕ. The tip apex exhibits a number of monatomic steps n along the path from [hkl] to [h'k'l']. These steps are separated by the distance s which is given for cubic crystal systems by

$$s = \frac{a}{\xi\sqrt{h^2 + k^2 + l^2}} \tag{3.1}$$

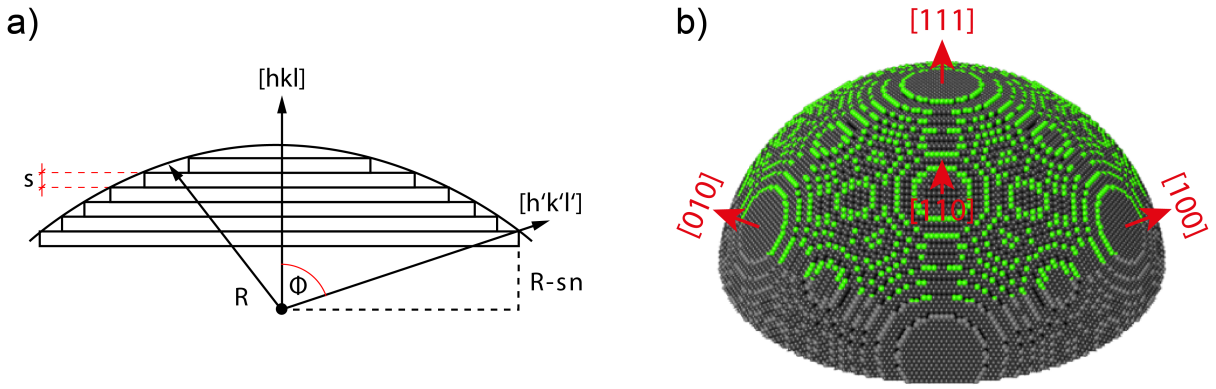

Fig. 3.2. A schematic drawing of the surface layers and a ball model constructed for a nm-sized Rh tip apex imaged in Fig. 3.1; a) the angular separation of two poles ([hkl] and [h'k'l']) is indicated by angle ϕ and the relation between the radius R and the layer distance sn is illustrated by dotted lines; b) the ball model of a hemispherical Rh apex with a diameter of 25 nm. Main low Miller index facets are labeled.

where a is the lattice constant and ξ an integer being 1 if $h+k+l$ is even and being 2 if $h+k+l$ is odd, for an fcc crystal. As a consequence the radius R of the hemispherical tip apex can be calculated by the relation

$$R = \frac{sn}{1 - cos\phi} \quad . \tag{3.2}$$

Using this method, a radius of 25 nm was determined for the nm-sized Rh tip imaged in Fig. 3.1. Figure 3.2b shows the corresponding ball model, where protruding atoms, visible in the field of view in Fig. 3.1, are represented as green points.

3.1.2 Hydrogen oxidation reaction on the Rh nanotip

To reveal the kinetic behavior of the catalytic hydrogen oxidation reaction on the Rh nanotip, the reaction was studied by FEM. As already explained in section 1.4.5, this reaction has a bistable character and the variation of external parameters such as, e.g p_{H_2}, may induce a kinetic transition between the two steady states of the reaction. Such kinetic transitions are usually accompanied by the nucleation and spreading of reaction fronts, which transport the gradient of surface coverage: low activity state - high oxygen coverage, high activity state - low oxygen coverage. The state of the surface can be monitored with FEM and thus the catalytic behavior of the reaction system can be revealed and summarized e.g. in a kinetic phase diagram.

Isothermal experiments in the temperature range 433 to 493 K:
Hydrogen oxidation experiments were performed at constant O_2 pressure (7.7×10^{-7} $mbar$) and constant temperature, chosen in the range of 433 to 493 K. In turn, the H_2 pressure was varied in the range from 1×10^{-7} $mbar$ to 1×10^{-6} $mbar$. At the beginning of such an isothermal experiment the surface was covered by oxygen, thus the system was in a low activity state (Fig. 3.3). The corresponding FEM image intensity obtained from the whole sample apex (Fig. 3.3a Frame 1) is low, as can be seen in Fig. 3.3b. The H_2 pressure was increased, then a kinetic transition τ_A to the active state was observed (Fig. 3.3b) at a p_{H_2} of 6.6×10^{-7} $mbar$. First, the reaction entered a transient state, where the corresponding FEM image brightness (Fig. 3.3 a Frame 2) is at a maximum level, then the intensity was stabilized at a high level (active state, Fig. 3.3a Frame 3). The observed kinetic transition τ_A happens simultaneously on all facets of the apex within the time resolution of the camera (0.02 s). High diffusivity of hydrogen at temperatures above 433 K causes the reaction to be spatially coupled within the whole field of view. Therefore the presented hysteresis loop (Fig. 3.3b) and the kinetic phase diagram (Fig. 3.3c) represent the whole nm-sized Rh apex. On further p_{H_2} increase the reaction system remains in an active state. The H_2 pressure was then lowered and at 3.7×10^{-7} $mbar$ a reverse kinetic transition τ_B was observed, when the FIM image brightness decreased to its initial level (low activity state, Fig. 3.3a Frame 4).

As already explained in section 1.4.5 a kinetic phase diagram can be constructed from transition points τ_A and τ_B obtained from these and analogue experiments that only differ in temperature, applied in a range from 433 K to 493 K (Fig. 3.3c). The region of bista-

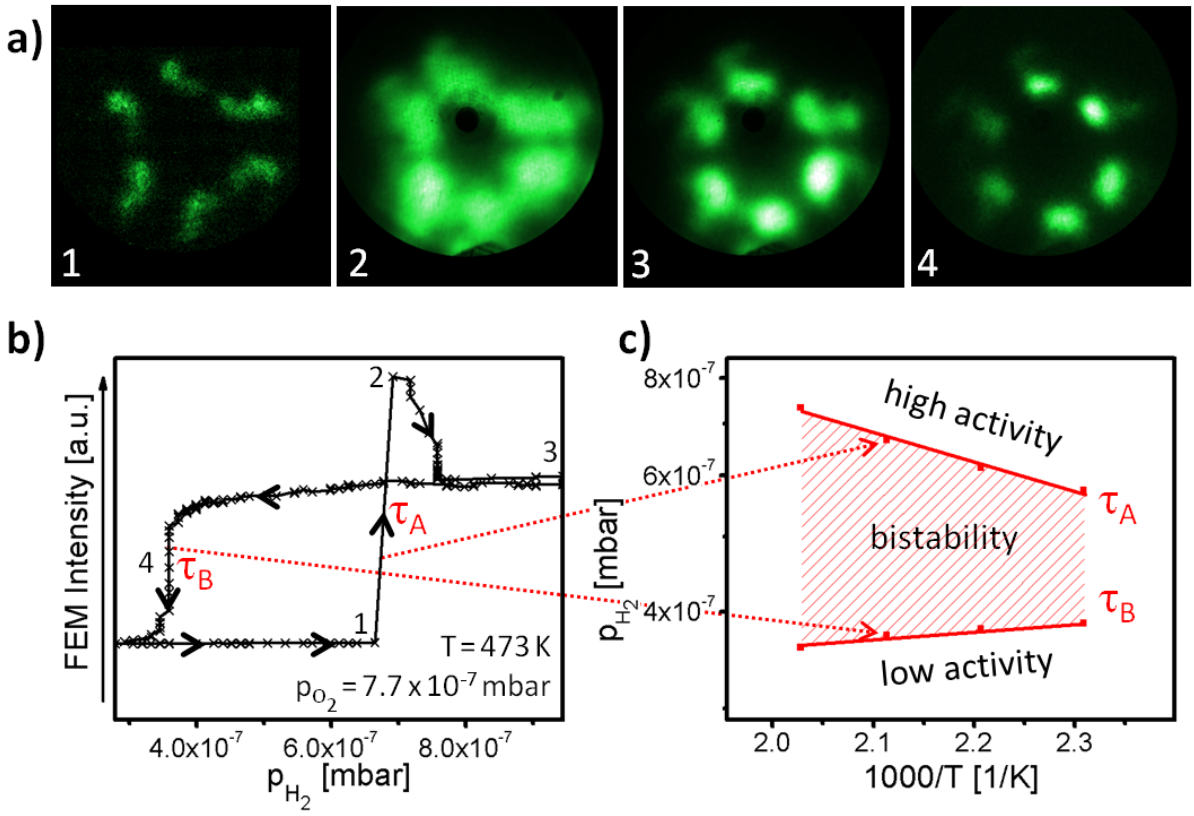

Fig. 3.3. Catalytic hydrogen oxidation reaction on a nm-sized Rh tip apex was studied: a) series of FEM video frames was taken during the cycle-wise variation of H_2 pressure at constant O_2 pressure (7.7×10^{-7} *mbar*) and constant temperature (473 K); b) the corresponding change in FEM image intensity is shown as a hysteresis like curve. The position of the video frames from (a) are labeled by numbers and the kinetic transitions between the two steady states of high and low activity are marked as τ_A and τ_B kinetic transition points; c) kinetic phase diagram including τ_A and τ_B values in a temperature range of 433 to 493 K at constant O_2 pressure.

bility narrows with decreasing temperature indicating that at lower temperatures lower H_2 pressures are sufficient to render the reaction into the high activity state and, in turn, the low activity state is reestablished at higher H_2 pressures than for higher temperatures.

Isothermal experiment at 413 K:

The hydrogen oxidation was additionally studied at a significantly lower temperature (413 K) on the nm-sized Rh tip apex. Kinetic transition points τ_A and τ_B were obtained in the same way as described above and are additionally marked in the phase diagram (Figure 3.4). The reaction behavior at 413 K differs drastically of that described in Fig. 3.3. The τ_A kinetic transition, to the active state at 413 K, occurs at a p_{H_2} of 6.9×10^{-7} *mbar*, which is high compared to the p_{H_2} obtained for τ_A points in the temper-

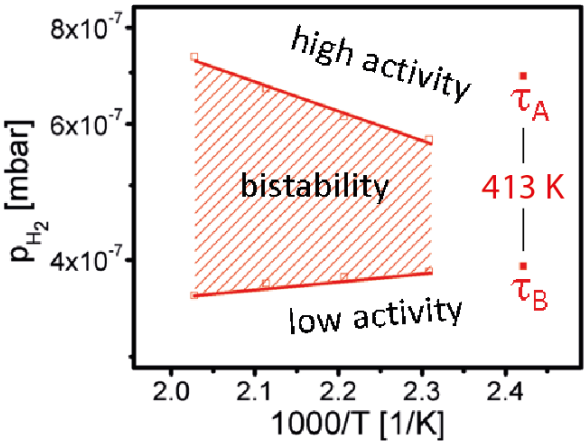

Fig. 3.4. Kinetic phase diagram for the hydrogen oxidation reaction on a Rh nanotip. Kinetic transition points obtained at 413 K and at constant O_2 pressure (7.7×10^{-7} *mbar*) are labeled (full squares). The τ_A and τ_B values, in a temperature range of 433-493 K are additionally plotted (empty squares) and regions of high activity, bistability and low activity are indicated.

ature range of 433-493 K. However, the kinetic transition point τ_B at 413 K and at a p_{H_2} of 3.9×10^{-7} *mbar* does not shift significantly to higher p_{H_2} values. The τ_B point prolongs the trend of transition points τ_B, obtained in the temperature range of 433-493 K. Consequently, τ_A and τ_B transition points at 413 K span a wide range of bistability. This rather abrupt change of reaction behavior at low temperatures ($\leq$ 413 K) meets with a curved Rh crystal and is explained in section 3.2.3.

Figure 3.5 shows such a kinetic transition τ_A of the nm-sized Rh tip at 413 K. The recorded FEM images (red) are superimposed on the FIM micrograph (green, taken from Fig. 3.1) to illustrate the underlying crystallographic surface structure. First, an increase of image brightness can be noticed around the Rh(101) facet (Fig. 3.5a) then the subsequent FEM pattern (Fig. 3.5b) shows additional bright spots on the six Rh{135} facets, which surround the Rh(111) facet in the center of the image. Later on, an increased brightness in the Rh(111) area, including the neighboring Rh{112} facets, is observed in Fig. 3.5c. The FEM pattern shown in Fig. 3.5d represents the final catalytically active state of the probed nm-sized Rh apex, comparable to Fig. 3.3a Frame 2. At the time all Rh{110} facets are surrounded by four bright Rh{135} facets presented in Fig. 3.5d.

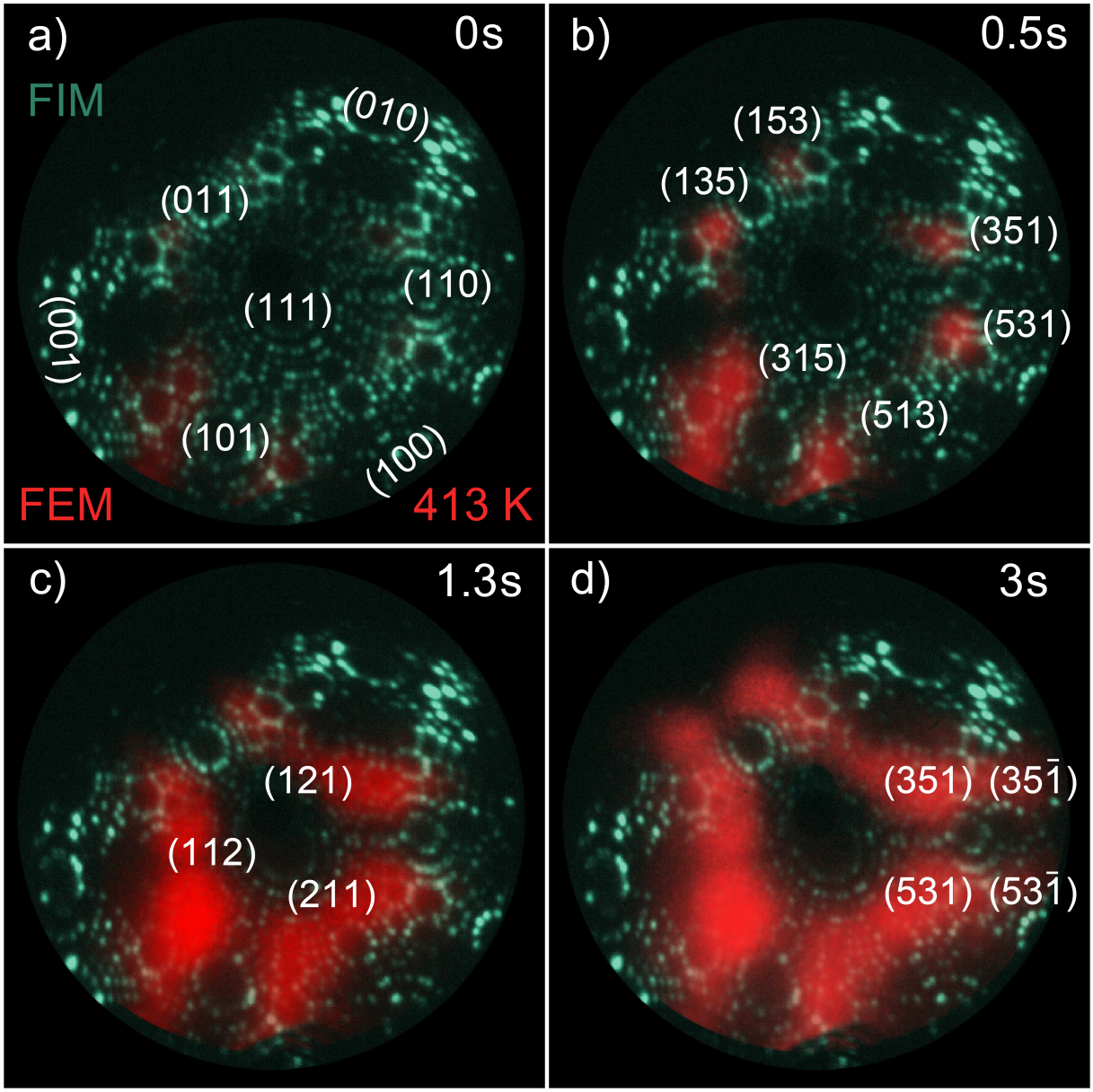

Fig. 3.5. Kinetic phase transition on a Rh nanotip for the H_2 oxidation reaction at 413 K: The FEM micrographs (red) are superimposed on a FIM image (green, taken from Fig. 3.1), that shows the arrangement of facets with atomic resolution. Main low Miller index facets are labeled.

The behaviour of the H_2 oxidation at 413 K differs strongly from that at higher temperatures (433-493 K). At higher temperatures the transition τ_A occurs simultaneously for the whole Rh apex (within the resolution of 0.02s). In turn, at 413 K the transition occurs separately for individual regions of the tip (at the same time resolution). The progress of the transition proceeds as illustrated in Fig. 3.5. Figure 3.6 represents a schematic

stereographic projection of the Rh tip. The evolution of the reaction fronts monitored in Fig 3.5 is schematically traced by arrows. Triangle-like regions with a centered Rh{111} facet are alternately shaded. Low Miller index facets e.g. Rh{110} are located half way on the border between two adjacent triangular-shaped regions and Rh{100} facets are situated on the corners. The idea to grid the sample surface into these triangular-shaped regions, serves as model used in further explanations.

The first appearance of active facets is around the Rh(101) facet (Fig. 3.5a), here the Rh(315) and the Rh(513) facets both become active. A front starts to spread and an increase of image brightness can be observed on all other Rh{135} facets within the center triangular-shaped region (light gray, Fig. 3.6a). Figure 3.6b reveals that starting from the Rh(315) facet, subsequent the Rh(135) facet and at last the Rh(153) facet show an increase of image brightness. These consecutive intensity increases are about 45 ms delayed (blue and green arrow). The reoccurring distance, on the hemispherical apex surface, from such a Rh{135} facet to a neighboring Rh{135} facet is 12.1 nm and is represented by arrows in Fig. 3.6a. Hence, a velocity of 270 nm/s is calculated for the propagating front along the blue and green arrows in Fig. 3.6. Then, the activated Rh{135} facets (Fig. 3.5b) show a fluctuating image intensity for about 500 ms (starting at 400 ms in Fig. 3.6c). Eventually the whole triangular-shaped region simultaneously changes to the active state (starting at about 1050 ms in Fig. 3.6c). Adjacent triangular-shaped regions labeled e.g. $(\bar{1}11)$ and $(11\bar{1})$ in Fig. 3.6a do not change to the active state at this stage of the kinetic transition. In Fig. 3.6c it is shown exemplary for the Rh$(35\bar{1})$ facet, that an increase of image brightness is observed over a second later (red arrow). In the same way a velocity of 12 nm/s can be calculated.

It can be summarized that within one triangular-shaped region the first initiation of Rh{135} facets happens "fast" (270 nm/s) one after another, spatially dependent on the starting point of the spreading front. Then a state of fluctuating image brightness is followed by a synchronized transition to the fully active state. The initiation of neighboring triangular-shaped regions (dark gray, Fig. 3.6a) is delayed. This can be explained with the unique crystallographic composition of facets located at the border of such two triangular-shaped regions. There, a centrally arranged Rh110 facet and vicinal surfaces exhibit grooves and can show missing row reconstructions (explained in section 1.4.3) parallel to the boarder of the two adjacent triangular-shaped regions. Such arrangement of surfaces causes an anisotropic propagation of reaction fronts [39, 87]. In the present

case, the propagation is therefore "slow" (12 nm/s) in the direction perpendicular to the grooves, e.g. on a Rh(110) facet in the [001] direction. Due to the two different time regimes that apply to the spreading front induced by the τ_A kinetic transition over the whole nm-sized Rh apex, a "stop and go" nature of the phenomenon is recognizable.

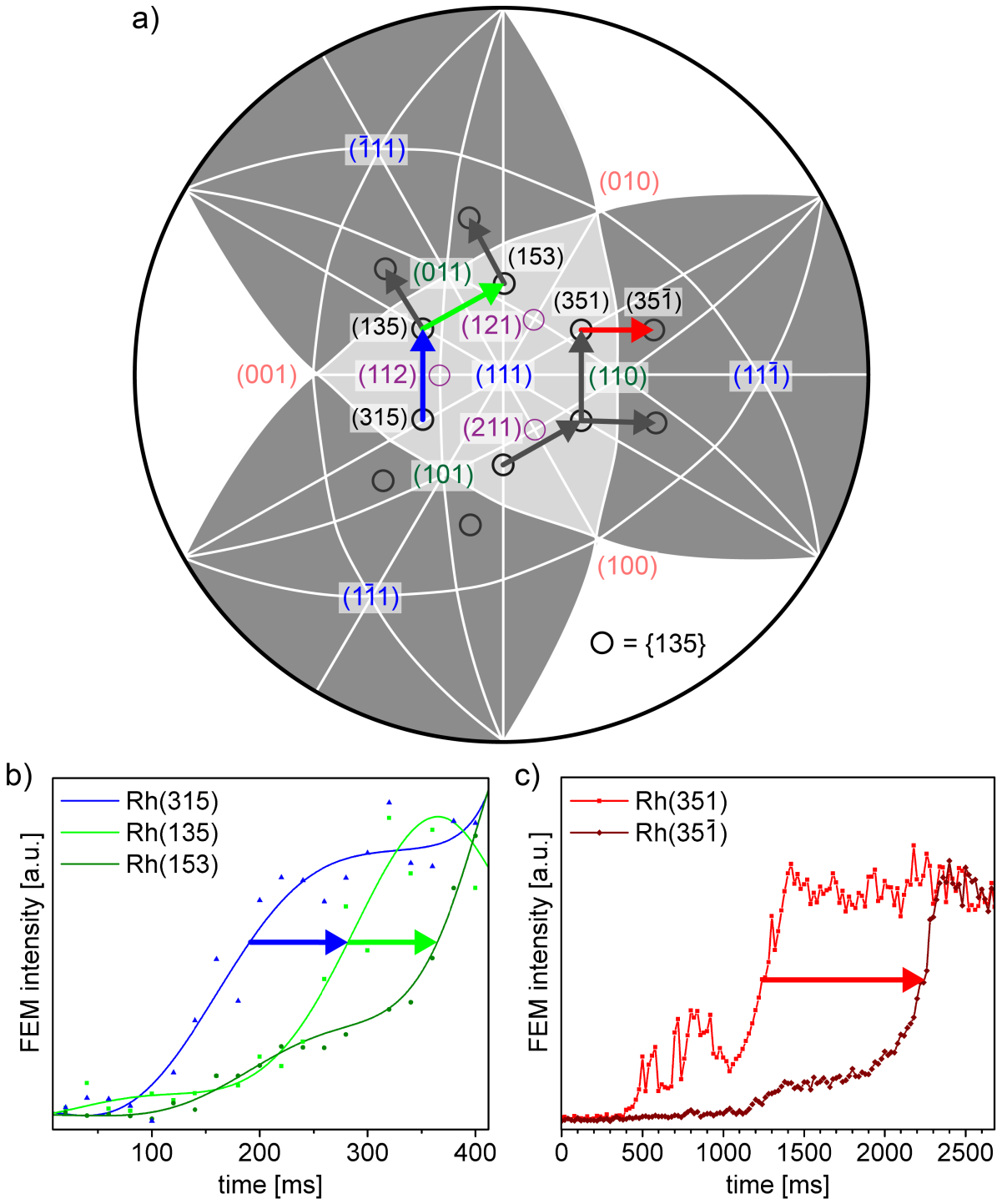

Fig. 3.6. Kinetic transition from inactive to active steady state at 413 K: a) stereographic projection of the nm-sized Rh apex. A centered triangle-like region (light gray) is framed by symmetric equivalent neighboring regions (dark gray). Arrows show the direction of front propagation; b and c) image brightness measured at different Rh{135} facets during the kinetic transition at 413 K. The colors of arrows in (b) and (c) correspond to the colors of arrows in (a).

3.2 Curved Rh crystal

Structure sensitivity is an important aspect in catalysis. The different reaction steps of a heterogeneously catalyzed reaction such as adsorption, reaction and desorption discussed in section 1.4.1 are structure sensitive [88, 89]. Most studies in surface science on structure sensitivity used single crystal samples with well ordered surfaces on the atomic level. When several surface orientations should be probed a set of single crystal samples containing differently oriented surfaces may be used. This is however a cost intensive investment. A systematic study to reveal the influence of different crystallographic surface orientations on a catalytic reaction would require a kind of a "surface structure library" containing differently stepped surfaces[90]. A polycrystalline surface may exhibit domains of different crystallographic orientations as described in section 3.3 providing a kind of a surface structure library. Using a spatial resolved surface analysis method, i.e. PEEM, different domains can be probed within one experiment. However, on a polycrystalline surface the distribution of crystallographic orientations of domains is rather random. A more ordered approach involves e.g. curved surface of a cylindrical crystal sample [91–95]. The advantage of studying such curved surface is that they exhibit a range of different step and kink densities dependent on the position of the surface. To span a wider range of crystallographic orientations, a sample curvature in two directions might be helpful and as a result a dome shaped curved crystal can be formed. A complete (including all possible single crystal surfaces) surface structure library was reported for Cu consisting of a set of six spherical single crystals [96]. Experiments on the oxidation behavior of Cu using such samples proved the high-throughput quality in terms of probed crystallographic orientations [97].

In this thesis a µm-sized dome shaped Rh curved crystal was prepared, so that all crystallographic orientations on the surface span the entire stereographic projection explained in section 1.3.3. This µm-sized hemispherical crystal sample serves as a complete library of fcc-structures. The FEM and FIM were used as spatially resolving microscopes to image the hydrogen oxidation reaction on such a Rh specimen.

3.2.1 Fabrication and identification of a µm-sized Rh curved crystal

The µm-sized curved crystal was fabricated from a Rh wire and formed by annealing in UHV as described in section 2.5.2. The surface of this sample was imaged using FEM and symmetrical patterns at different adsorbate coverages are shown in Fig 3.7. The crys-

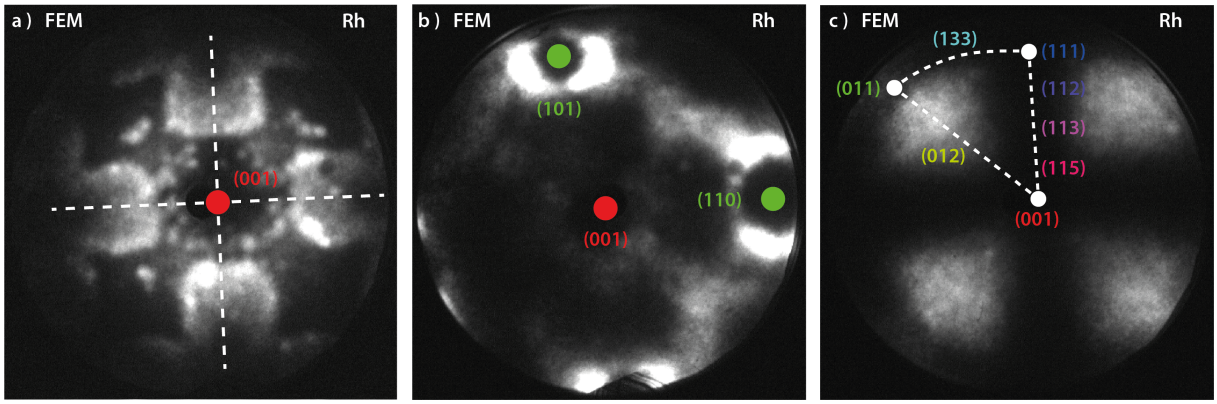

Fig. 3.7. Identification of the orientation of a µm-sized Rh curved crystal: a) FEM image of the Rh curved crystal sample indicates a four fold symmetry; b) at 600 K and a carbon monoxide pressure of 2.3×10^{-6} *mbar* carbon islands are formed around the Rh{110} facets; c) FEM micrograph of the clean surface with low miller index facets labeled and the stereographic triangle marked by dotted lines.

tallographic identification of the curved Rh crystal surface by FEM images relies on the stereographic projection discussed in section 1.3.3 in addition to the crystal system of the sample. A hemispherical fcc Rh crystal apex exhibits poles of different symmetries, each representing a particular crystallographic direction. The FEM image of the Rh sample reveals the four-fold symmetry, where the central region is related to a Rh(001) facet (Fig 3.7a). To reveal the positions of other main low Miller index surfaces, additional "symmetry arguments" were used. Figure 3.7b shows the curved crystal surface after an exposure of carbon monoxide at 2.3×10^{-6} *mbar* at 600 K. Bright ring like structures can be seen and should form around Rh{110} facets as reported in literature [ ]. With the positions of the orientations {100} and {110} and the symmetry of fcc Rh, the full identification of surface crystallography is possible (Fig. 3.7c). The labeled Miller indices are colored corresponding to the inverse pole figure (Fig. 1.3).

3.2.2 Spherical model

The apex of the Rh curved crystal sample can be described by a hemisphere. The radius of that hemisphere was determined in three ways: (i) An estimation based on the necessary potential to image the tip with FEM; (ii) an optical microscope image (Fig. **??** indicated a tip radius of about 0.5 µm; (iii) a SEM micrograph. Starting from the curved crystal orientation and the apex diameter of 0.65 µm a 3D-model can be constructed. Figure 3.8 shows such a model for a hemispherical apex of a presented [001]-oriented Rh tip. $\{kh\,k\,l\}$-facets are indicated by black circles. Which facets appear as circles is determined

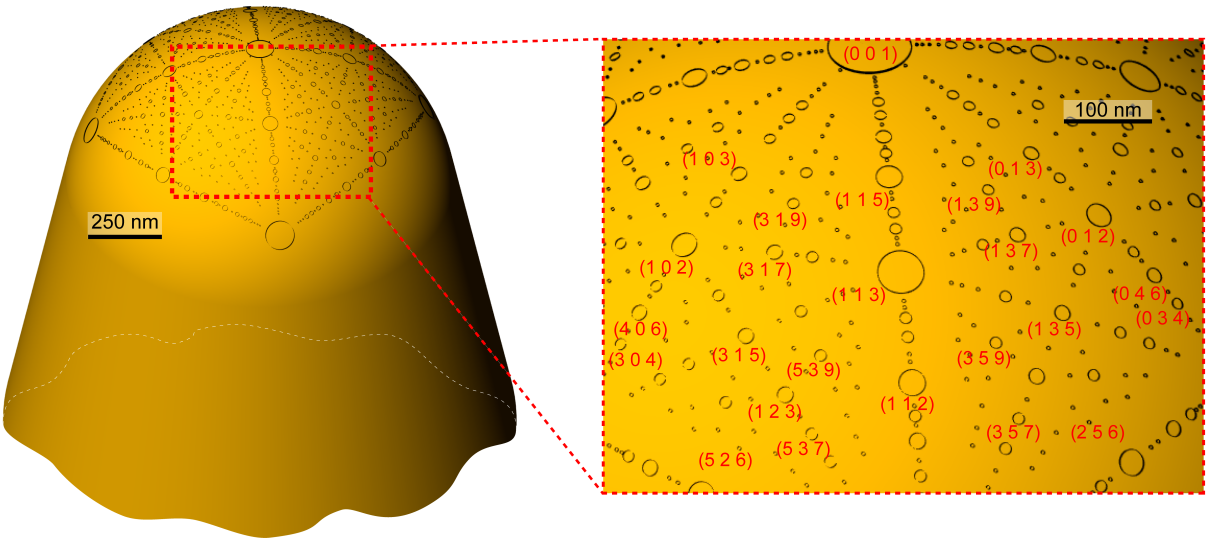

Fig. 3.8. Hemispherical model of the curved crystal. Based on a radius, distances on the surface between two facets can be calculated. The magnified area around the (113) orientation has labeled low Miller index facets (bigger circles) as well as labeled higher Miller index facets (smaller circles).

by a threshold value for inter-layer distances (d-spacing, explained in section 3.1.1.2) between the closest planes of a certain crystallographic orientation. The radius of a circle indicates the magnitude of the d-spacing, which means that low miller index directions are represented by bigger circles. From this model, distances and directions in real space can be obtained using the stereographic projection images. A region of interest on the model of the curved crystal shown as an inset in Fig. 3.8 is labeled with the according Miller indices of crystallographic orientations.

Figure 3.9 presents a SEM-micrograph of the crystallographically fully characterized curved Rh crystal sample. The constructed net of orientations is additionally introduced

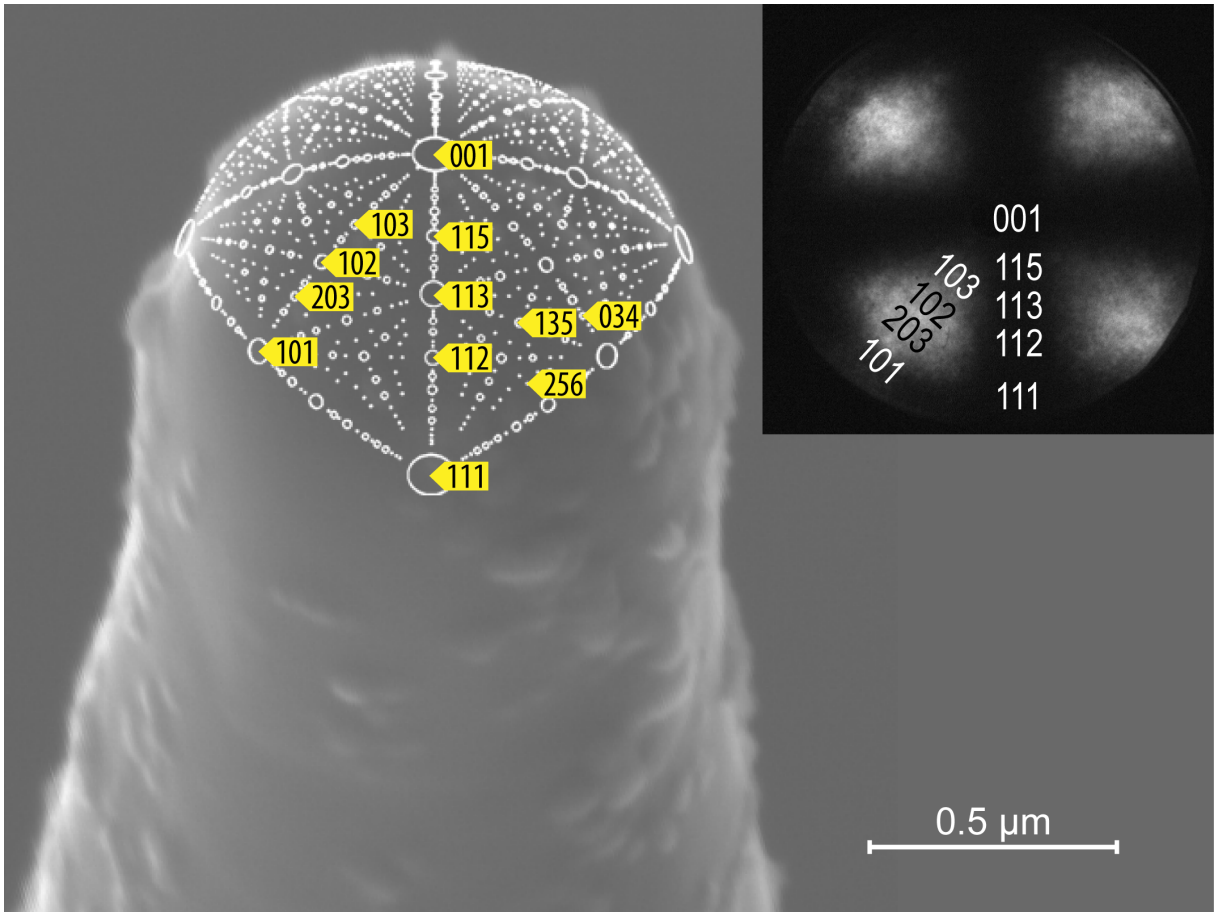

Fig. 3.9. SEM micrograph of the curved crystal specimen. The net of crystallographic orientations is introduced as an overlayer. The inset shows the corresponding FEM micrograph of the clean Rh surface.

as an overlayer. The inset shows the corresponding FEM-image of the clean Rh surface.

3.2.3 Hydrogen oxidation reaction on the curved Rh crystal

The catalyzed hydrogen oxidation reaction exhibits a bistable character in a broad parameter range. Kinetic transitions between the high and low activity state occur at different external parameters. Experiments were performed at constant external parameters (p_{O_2} and T) performing only a cyclewise variation of p_{H_2}. A change of surface coverage was imaged by FEM. The *kinetics by imaging* approach sets up a relationship between the obtained FEM image intensity and the catalytic activity state of the reaction. In turn, the bistability of hydrogen oxidation on Rh can be quantified from the hysteresis-curves of image intensity to p_{H_2}. In such a way Kinetic transition points τ_A and τ_B were extracted from experiments. A kinetic phase diagram was constructed using the obtained points to summarize the catalytic behavior of the $H_2/O_2/Rh$ reaction system as described in section 1.4.5. For the µm-sized curved crystal sample the propagation of reaction fronts was studied in a temperature range of 393 to 493 K by FEM. The nucleation centers of such reaction fronts were characterized using the reaction product water as an imaging species in FIM, to directly image initial active sites.

Isothermal experiments in the temperature range 433 to 493 K:

In analogy to section 3.1.2, isothermal hydrogen oxidation experiments were performed at constant p_{O_2} (7.7×10^{-7} *mbar*), at different temperatures ranging from 433 to 493 K. At the start of each experiment the surface of the curved Rh crystal was oxygen covered and therefore in the low activity state (low image intensity, Fig. 3.10). An increase of p_{H_2} to 1.2×10^{-6} *mbar* and subsequent reduction to the initial p_{H_2} pressure, revealed the kinetic transitions between the inactive and active steady states of the reaction and *vice versa*. All facets of the curved Rh crystal are coupled by spreading reaction fronts that accompany kinetic transition of the catalyzed hydrogen oxidation reaction.

Figure 3.10b shows the kinetic phase diagram constructed from τ_A and τ_B values obtained from such isothermal experiments in the temperature range from 433 to 492 K. The width of the bistability area is dependent on temperature and narrows towards low temperatures: i.e. at lower temperatures a lower p_{H_2} is necessary to activate the high activity state of the hydrogen oxidation reaction and in turn a higher p_{H_2} is necessary for the low activity state of the catalyzed reaction.

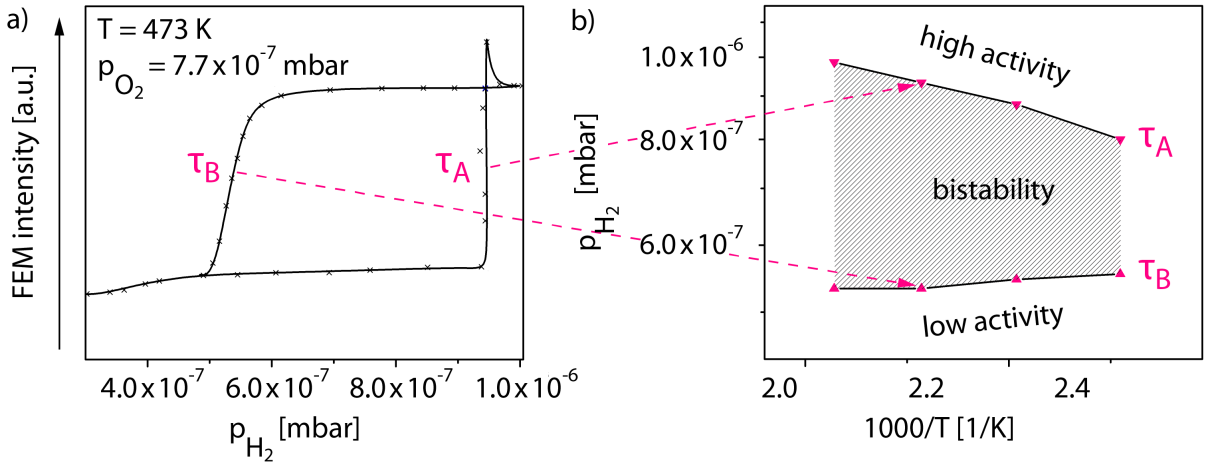

Fig. 3.10. Catalytic hydrogen oxidation reaction on a curved Rh crystal sample: a) hysteresis like FEM intensity curve obtained during the cyclic variation of hydrogen pressure, at constant oxygen pressure of 7.7×10^{-7} *mbar* and a constant temperature of 473 K. The kinetic transition points τ_A and τ_B are labeled; b) kinetic phase diagram constructed from τ_A and τ_B values in a temperature range of 433 to 493 K at constant p_{O_2}. The bistable region and the monostable regions of high and low activity are indicated.

3.2.3.1 Reaction front propagation guided by surface reconstruction

As already mentioned, the catalyzed hydrogen oxidation reaction can operate in two steady states dependent on external parameters i.e. partial pressures and temperature. If oxygen predominately covers the Rh surface the reaction is in the low activity state. Increasing hydrogen pressure, hydrogen will win the adsorption competition and will react off the oxygen on the surface. The high activity state corresponds to the reduced surface. A spreading reaction front indicates the boundary between differently covered surface areas. Such a replacement of coverage on the surface can be described by a spreading reaction-diffusion front.

Experiments on the Rh curved crystal were performed at 413 K and 433 K to observe the spreading hydrogen fronts. Starting at an initially oxygen covered surface (low activity state), p_{H_2} was increased at constant oxygen pressure (7.7×10^{-7} *mbar*) until a τ_A kinetic transition to the active state was initiated. The occurring hydrogen fronts were imaged with FEM, showing an evolution of bright patterns (high activity state - hydrogen phase) while p_{H_2} was kept constant. Figure 3.11 includes series of FEM micrographs, recorded during the spreading of reaction fronts at 413 K and 433 K.

The hemispherical shape of the Rh sample allows to use this curved crystal as a "surface structure library". This means, that a full set of differently oriented facets is present

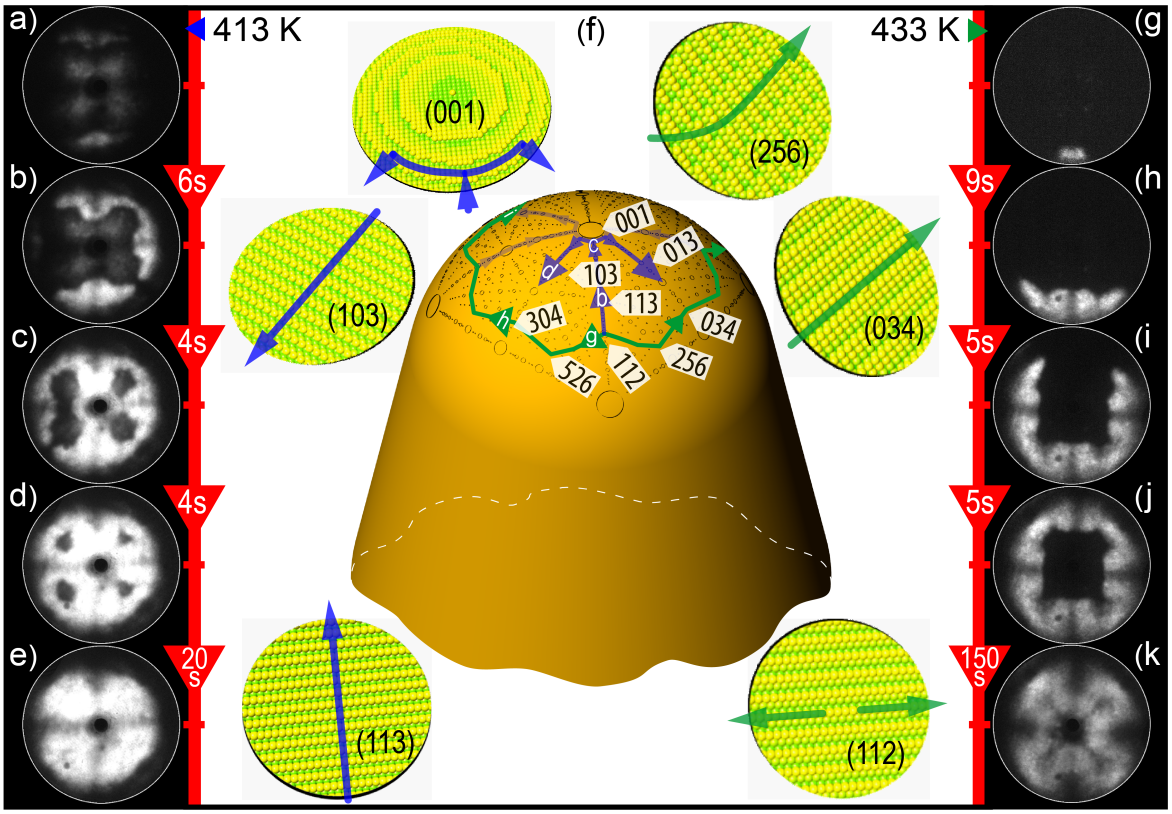

Fig. 3.11. Front propagation of the hydrogen oxidation reaction on a curved Rh crystal: a-e) spreading of reaction fronts at 413 K during the catalytic transition to the high activity state displayed by FEM micrographs, taken at significant instants; f) hemispherical model of the curved Rh crystal and ball models of different stepped surfaces. Blue arrows are part of a blue path that corresponds to (a-e) and green arrows are part of a green path that corresponds to (g-k). The paths indicate the predominant direction of front propagation; g-k) spreading of reaction fronts at 433 K during the catalytic transition to the high activity state displayed by FEM micrographs, taken at significant instants.

multiple times on the whole sample surface in close proximity to each other. Such kind of "surface structure library" is suitable to reveal structure sensitive phenomena like propagating reaction fronts . Appearing reaction fronts expand across all these different surface orientations and at the same time, they may reveal their structure sensitivity towards their direction and velocity of propagation, within one experiment. From *in situ* FEM videos, paths of such "guided" reaction fronts were evaluated and are shown in Fig. 3.11f for two temperatures: 413 and 433 K.

Isothermal experiment at 413 K:

Propagation of the reaction fronts at 413 K upon a τ_A kinetic transition is shown in

Fig. 3.11a-e. Figure 3.11a shows the beginning of spreading reaction fronts at the Rh{112} facets on the curved crystal. Due to a fourfold symmetry, this Rh{112} facet appears four times within the field of view forming the corners of a square (section 3.2.1). It can be seen, that the Rh(112) facet is already in the high activity state, as well as the counterpart Rh($\bar{1}\bar{1}2$) facet. As Fig. 3.11b shows, the predominate direction of spreading is towards the center of the image and towards neighboring Rh{110} facets. On these Rh{110} facets the speed of propagation is slowed for reasons discussed in section 3.1.2. A third nucleation event, and the resulting pattern can be seen on the right hand side of the image. Figure 3.11c shows, that propagating reaction fronts reached the center Rh(001) facet and merge sideways on the Rh(001) vicinal surfaces. A forth front from the left hand side can be seen. In Fig. 3.11d, last remaining dark regions located around Rh{103} facets are visible. Figure 3.11e finally shows the whole sample being in the high activity state of the hydrogen oxidation reaction.

Isothermal experiment at 433 K:

In analogy to the previously described experiment, Fig. 3.11g-k shows a series of FEM images taken during an equivalent experiment at 433 K. The exemplary selected images describe the propagation of the hydrogen front. In Fig. 3.11g the nucleation of a reaction front on the Rh(112) facet is shown. Subsequently, as visible in Fig. 3.11h, the front spreads preferable towards the Rh{110} facets. Figure 3.11i shows the delayed propagation of the front towards the center Rh(001) facet. further progression of the front can be seen along a "meridian-like" path (green path, Fig. 3.11f) around the curved crystal. In Fig. 3.11j it can be seen, that this circular path is closed. Still, a rectangular-shaped area enclosed by Rh{113} facets remains dark. Finally, Fig. 3.11k shows that, the high activity state on the whole apex was established (delayed by 150 s).

It can be summarized, that the appearance and structure sensitive broadening of high activity surface regions, during a kinetic transition τ_A, differs with temperature. In the experiments performed at 413 and 433 K, the nucleation of reaction fronts takes place at Rh{112} facets. However, for temperatures $\leq$413 K multiple Rh{112} facets were generating reaction fronts. On the contrary, in all performed experiments at temperatures $\geq$433 K, only a single Rh{112} facet induced a nucleation event within the field of view. As discussed in section 1.5 spreading hydrogen fronts on different Rh surfaces can show anisotropy in their directions of spreading. Especially on stepped and kinked surfaces the progressive motion of fronts is guided by the particular configuration of steps and ter-

races [98]. The Rh curved crystal serves as a collection of such differently oriented facets assembled in close proximity to each other and aligned according to the stereographic triangle. At temperatures $\leq$413 K spreading fronts oriented towards the center can be observed on the curved Rh crystal, whereas at temperatures $\geq$433 K the propagating reaction fronts follow a "latitude-line-like" path. A change of the crystals surface structures occurring between these two temperature regimes may describe the differences of the observed front propagation.

As reported in section 1.4.3 bulk-terminated Rh facets can rearrange to a missing row reconstruction at elevated temperatures. Figure 3.12 shows such missing row reconstructions of facets next to bulk-terminated facets for comparison. A suitable model of the Rh curved crystal (introduced in section 3.2.2) with a radius of 100 nm (Fig. 3.12a) represents the basis for the calculation of ball models, representing the atomic structure of a hemispherical sample. Framed sections (dashed lines), including each a full set of crystallographic orientations, are presented in Fig. 3.12b. The ball model of a bulk-terminated surface section (blue, left hand side) is depicted besides the ball model including reconstructed facets (green, right hand side). There, Rh{113} and Rh{011} facets show a (1×2) missing row reconstruction. Since every second row is missing, surface roughness for the reconstructed facets increases. Rh atoms from the third layer have missing nearest neighbor Rh atoms and can therefore be seen in the ball model (purple-like color). These missing row reconstructions were not reported below 400 K [26]. The two surface morphologies (bulk-terminated and reconstructed) can be attributed to the two different paths (cross-like and meridian-like, Fig. 3.11f) of the spreading reaction fronts. White arrows and dashed lines in Fig. 3.12b represent the two paths on the attributed surface. On the bulk-terminated surface the initiated front spreads towards the center Rh(001) facet across stepped facets i.e. Rh(113) and Rh(115) and sideways along vicinal terraces of Rh(111). Kinked facets such as Rh(315) delay the propagation of the reaction fronts. This is also the case for the uniquely stepped Rh(102) facet. Here terraces being vicinal to Rh(001) lie perpendicular to the typical grooves of Rh{101} terraces, a composition creating a homogeneous degree of surface roughness with no directional preferences. These are the last facets to be occupied by the hydrogen phase. On the other hand, at temperatures $\geq$433 K the observed evolution of patterns does not proceed to the center Rh(001) facet. At the position of reconstructed Rh{113} facets the spreading front is almost stopped in comparison to the progress of front propagation along the meridian-like path. A full circle along this path closes after 19 s. A rectangular region (visible in Fig. 3.11j) between the Rh{113} facets remains in the low activity state of the reaction. During 150 s this region

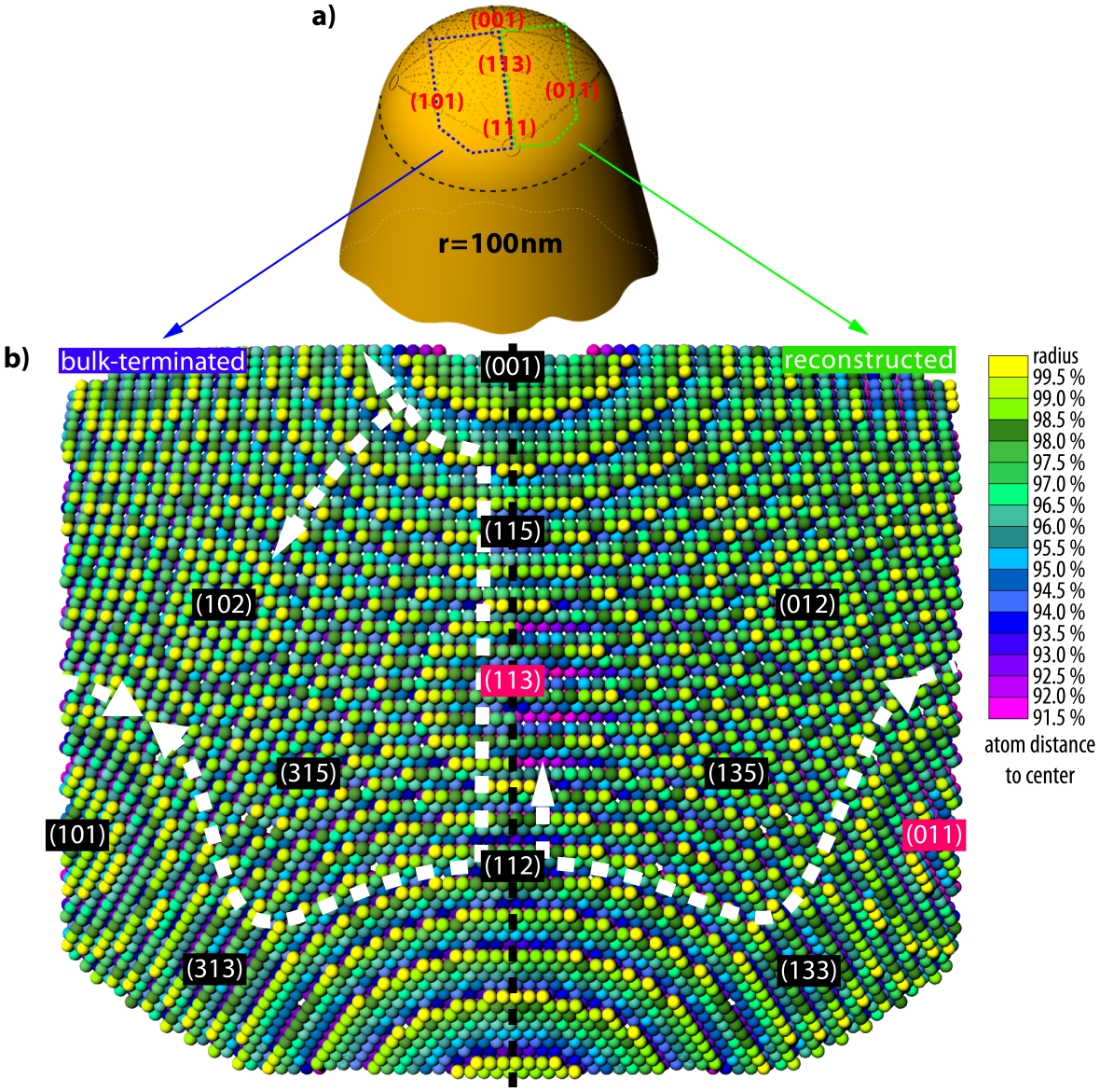

Fig. 3.12. Surface structure of a Rh curved crystal sample: a) model of a Rh curved crystal sample based on the crystallographic orientation discussed in section 3.2.2. Two regions of interest including each a full set of crystallographic orientations are framed; b) part of a ball model from a hemispherical Rh sample with a diameter of 100 nm. The balls represent Rh atoms and are colored according to their distance to the center of the hemisphere. Differently oriented facets and vicinal planes are shown. Left hand side (corresponds to the blue frame in (a)): the Rh surface is bulk-terminated; right hand side (corresponds to the green frame in (a)): the surface shows a (1×2) missing row reconstruction on Rh{011} and Rh{113} facets. White dashed lines indicate the predominately direction of reaction front propagation depicted in Fig. 3.11f.

slowly scales down and finally disappears. The reconstructed facets i.e. Rh{113} may facilitate the growth of oxide, which could act as a barrier to front propagation and has

to be reacted of by hydrogen first.

The behavior of the hydrogen oxidation reaction in a temperature range from 392 to 493 K on the curved Rh crystal is summarized in Fig. 3.13. The kinetic phase diagram for the temperature range from 433 to 493 K and τ_A and τ_B obtained at 393 K and 413 K are presented. As discussed earlier, at both temperature regions front propagation occurs

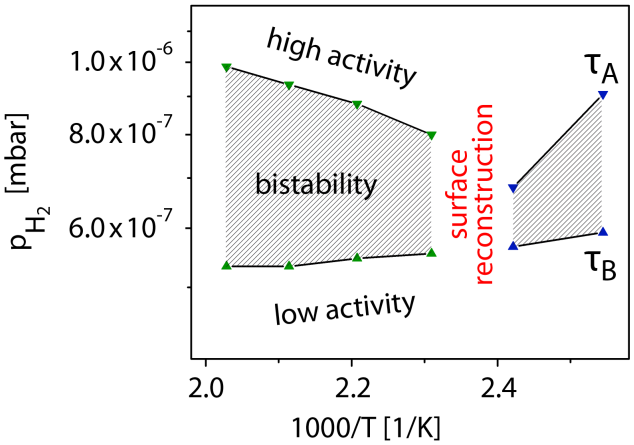

Fig. 3.13. Behavior of the hydrogen oxidation reaction on the curved Rh crystal sample, summarized in a kinetic phase diagram. Kinetic transition points τ_A and τ_B were obtained in a temperature range from 393-493 K. Two regimes for the reaction behavior can be identified, which are separated between 413 and 433 K.

along a specific path that is guided by surface reconstructions. In a temperature range of 433≥T≥413 K the surface reconstruction occurs. Correspondingly, the shape of the phase diagram presented in Fig. 3.10 changes at this critical temperature.

3.2.3.2 Nucleation of a reaction front

To reveal active sites on a catalyst surface during an ongoing chemical reaction, field ionization of reaction products and consequent use of the resulting ions as imaging species in FIM can be used [99–104]. For instance, in the case of a Pt specimen during hydrogen oxidation the reaction product water can be ionized to H_3O^+ and to H_2O^+ and exploited as the main imaging species [105–107]. In turn, the pulsed field desorption mass spectrometry was applied to study water formation from O_2 and H_2 on Rh nanotips [108].
The µm-shaped curved Rh crystal can serve as a surface structure library that reveals surface sites, where the kinetic transition from low activity state to high activity state occurs. Upon such kinetic transition first active sites that start to produce water molecules will also provide the imaging species for FIM.

Isothermal experiment at 393 K:
The corresponding FIM experiment was performed at a constant temperature of 393 K. At first a constant oxygen pressure was set up to 2.1×10^{-5} *mbar* and with FEM the adsorption of oxygen on the Rh curved crystal surface could be monitored. The polarity of the applied voltage was changed and the field of about 10 V/nm was applied to ionize the originating water molecules. Then the hydrogen partial pressure was raised (up to 8.0×10^{-5} *mbar*) to induce a kinetic transition. The kinetic transition was imaged by FIM using the reaction product (water) as imaging species. Figure 3.14 shows such a kinetic transition towards the active state at p_{H_2} of 2.6×10^{-5} *mbar*. One after another, Rh{112} facets start the nucleation of water production. Figure 3.14h shows schematically the temporal evolution of the initial reaction front across the Rh surface. The propagation of the reaction front is reflected in gray areas that spread predominately towards the Rh{111} facets (yellow arrow).
The behavior of the τ_A kinetic transition at 393 K matches with experiments discussed in section 3.2.3.1 and which were performed at the same temperature. In both cases, each of the Rh{112} facets serves as an independent center of nucleation of the kinetic transition and as a consequence four separated spreading reaction fronts could be observed at 393 K. The role of this facet being the "pacemaker" in hydrogen oxidation on Rh seems to be related to that of RhO_x formation. Combined STM and DFT studies on Rh(113) surfaces and "flatter" Rh(223) surfaces revealed, that these surfaces (and probably many similar vicinal surfaces) can stabilize single Rh adatoms at low coverages of oxygen ($\leq 2/3$ ML) by forming single RhO_2 species. These RhO_2 species arrange themselves to

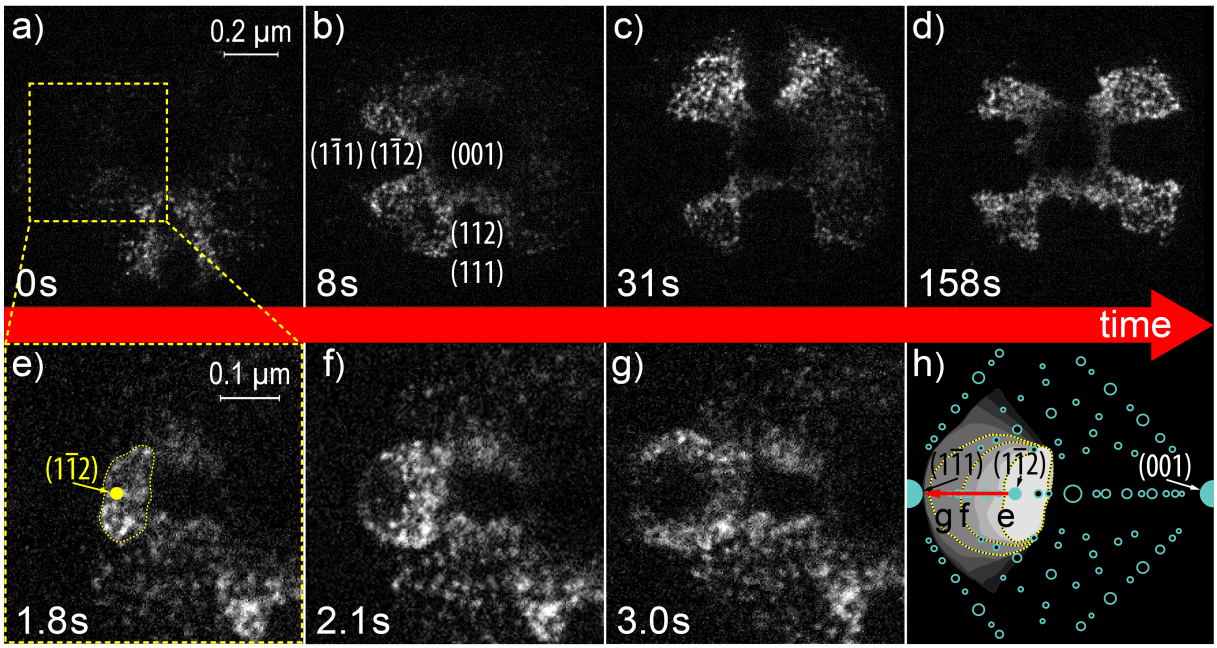

Fig. 3.14. FIM mapping of active sites on the Rh curved crystal during hydrogen oxidation: a-d) FIM images taken during the kinetic transition to the active state. The evolution of water production over the whole Rh curved crystal is shown; e-g) the "Zeitlupe" for the period between (a) and (b); e) magnification of the yellow square region in (a) at 1.8 s after (a). The catalytically active region forms at the Rh(1$\bar{1}$2) facet and is framed by a dashed line; f) the reaction front predominately spreads towards the Rh(1$\bar{1}$1) facet; g) the area of active sites forms a circular shape that continues to grow; h) shapes of reaction fronts (including the shapes of reaction fronts from (e-g)) are shown to illustrate the spatio-temporal evolution of reaction fronts on-top of a crystallographic net.

regular structures on the terraces of Rh(113)-like surfaces and in that way increasing the density of dangling bonds at the surface. The O-stabilized Rh adatoms show oxide-like properties. Therefore, this initial oxidation phenomenon can be described as 0D oxide formation and is understood as a precursor to tri-layer surface oxide formation at higher oxygen coverages [109, 110]. It is argued, that the surfaces hosting undercoordinated Rh ad-monomers stabilized by oxygen are highly reactive compared to any other sort of initial Rh oxides [111]. In the present experiments on the Rh curved crystal, the reaction conditions of the oxygen pressure of 2.1×10^{-5} *mbar* and temperature of 393 K may allow the Rh{112} facets to rearrange in a similar way. The observed nucleation of reaction fronts at Rh{112} facets underlines the high reactivity character of this surface orientations, at least in hydrogen oxidation on Rh.

3.3 Polycrystalline Rh foil

The polycrystalline Rh foil sample was introduced in section 2.5.3. After pretreatment the cleanness of the sample was verified with XPS. The clean sample surface could be imaged with PEEM. Figure 3.15 shows a PEEM image of several flat domains cut from metal grains forming the polycrystalline Rh foil. The size of these domains lies in the

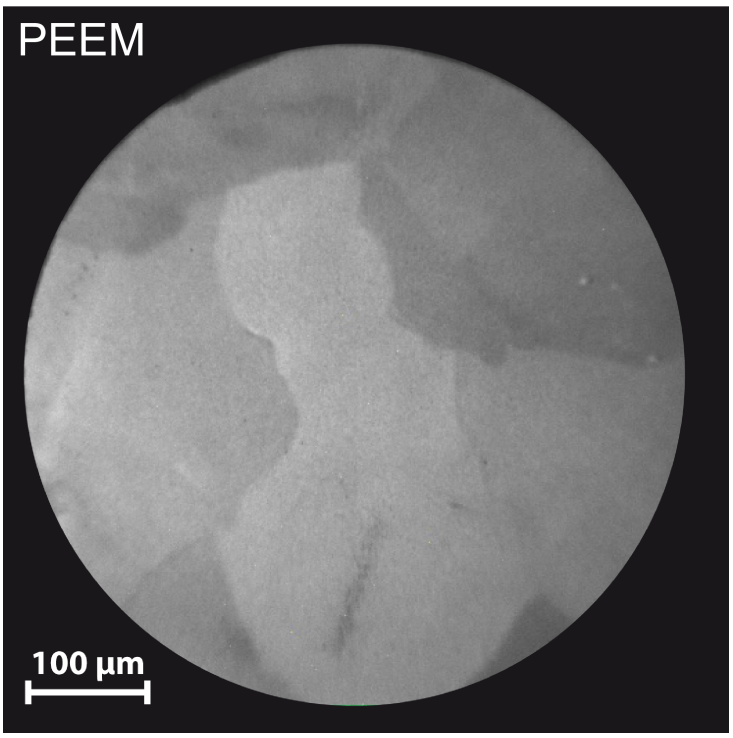

Fig. 3.15. PEEM image of a clean polycrystalline Rh surface. The Rh foil consists of µm-sized differently oriented high miller index domains confined by grain boundaries.

range of 0.1 mm and each domain is framed by a grain boundary (visible as a dark line). Such grain boundaries are interfaces between two grains, or crystallites forming a polycrystalline material. Grain boundaries are two dimensional defects in a bulk material who i.e. decrease thermal conductivity, disrupt dislocations or serve as onset points for corrosion. On the flat polycrystalline sample surface the different orientations of metal grains to each other, result in the formed domains to appear at different levels of brightness. The contrast appears due to different work functions of the corresponding differently stepped Rh surfaces.

Therefore the polycrystalline Rh sample serves as kind of a surface structure library. Within the field of view of a microscope, i.e. PEEM, a set of randomly distributed surface orientations can be probed. This allows to observe differences in the structure sensitive

behavior of the hydrogen oxidation reaction on the Rh sample within one experiment. The influence of surface structure on nucleation and propagation of reaction fronts during hydrogen oxidation will be discussed in detail below.

3.3.1 Identification of the polycrystalline Rh foil crystallography

In order to study the hydrogen oxidation reaction on the individual domains of the polycrystalline Rh foil their precise crystallographic orientation was defined by EBSD. The EBSD measurements were performed by a field emission scanning electron microscope in combination with an EBSD detector and an evaluation procedure as already explained in section 2.4. The result is shown in Fig. 3.16. Within the same field of view as shown in

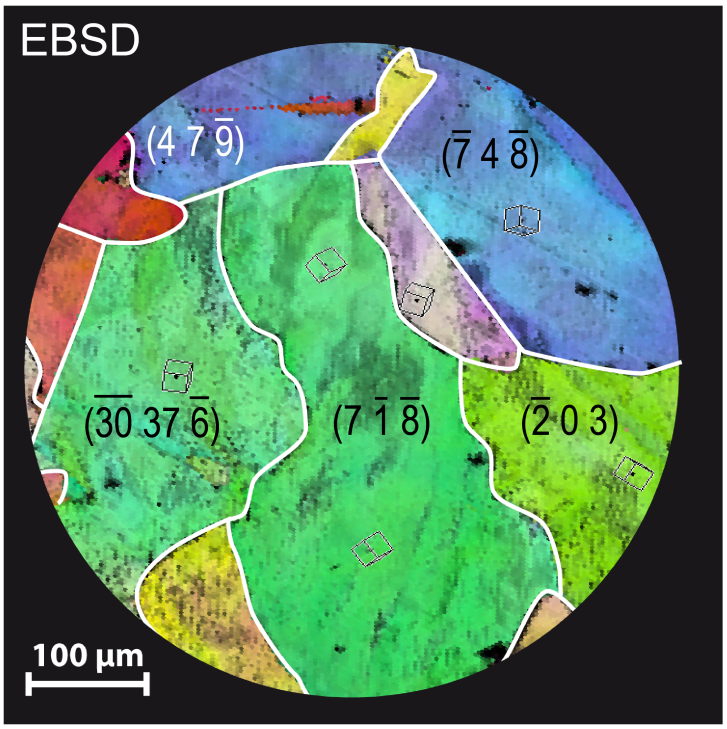

Fig. 3.16. The EBSD color coded map determines the crystallographic orientation of individual domains of a polycrystalline Rh foil. Stepped surfaces are labeled by the corresponding high Miller index and grain boundaries are highlighted by white lines.

Fig. 3.15 µm-sized domains are labeled with the exact corresponding high miller index. The color code of the EBSD map representing different crystallographic orientations is attributed to the inverse pole figure depicted in Fig. 1.3. Grain boundaries are marked by white lines and black dots within a domain represent particle like defects of different sizes.

3.3.2 Hydrogen oxidation reaction on the polycrystalline Rh foil

The catalytic hydrogen oxidation reaction on Rh has a bistable character as already explained in section 1.4.5. The catalytic reaction system can be in either of two steady states: the low activity state, where a dense oxygen layer covers the Rh surface, and the high activity state, with mainly hydrogen adsorbed on the Rh surface. A change of external parameters, i.e p_{H_2}, or temperature regulates the surface coverage and accordingly triggers kinetic transitions between the two steady states. Such a kinetic transition may be accompanied by the nucleation and propagation of a reaction front.

Isothermal experiments in the temperature range 433 to 493 K:

The PEEM image in Fig. 3.17a shows such spreading reaction fronts at 493 K, where the dark oxygen covered areas are consumed by enlarging bright hydrogen covered areas. This τ_A kinetic transition to the high activity state can be induced by an increase of p_{H_2}

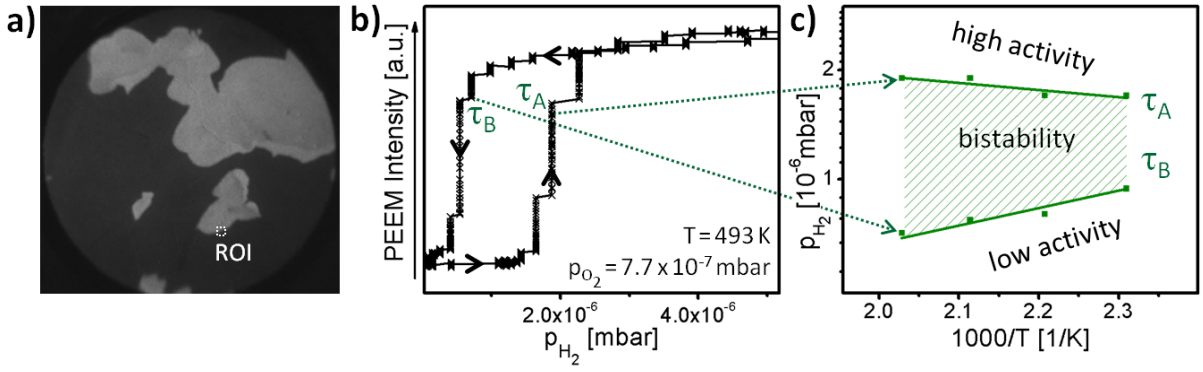

Fig. 3.17. Catalytic hydrogen oxidation reaction on a polycrystalline Rh foil: a) PEEM image taken during a τ_A kinetic transition to the high activity state. Spreading reaction fronts enlarge the bright hydrogen covered areas and couple domains within the field of view. The labeled ROI was used to measure the image intensity during experiments; b) change of PEEM image intensity during variation of p_{H_2} at constant temperature shows a hysteresis like curve. Two transition points τ_A and τ_A can be determined; c) kinetic phase diagram including transition points from the temperature range of 433 to 493 K at constant p_{O_2}.

as shown in Fig. 3.17b. The PEEM image intensity during all experiments was measured in the rectangular ROI labeled in Fig. 3.17a. During the induced kinetic transition the observed reaction fronts unimpeded cross the grain boundaries and couple the kinetic transition on different oriented Rh domains. The hysteresis like curve shown in Fig. 3.17b therefore represents the whole Rh surface. The almost stepwise change of the measured PEEM intensity reveals besides the τ_A kinetic transition also the τ_B kinetic transition when p_{H_2} is changed in a cyclewise way.

From kinetic transition points obtained from such isothermal experiments within a temperature range of 433 to 493 K, a kinetic phase diagram was constructed (Fig. 3.17c) for the polycrystalline Rh foil.

3.3.2.1 Nucleation centers

Figure 3.18 shows propagation of reaction fronts just after their nucleation on the polycrystalline Rh-foil, induced by a kinetic transition from the oxygen covered state to the active reduced state. The nucleation of reaction fronts occurs on defects present on the flat Rh sample surface. A comparison with the EBSD map in Fig. 3.16 reveals that the

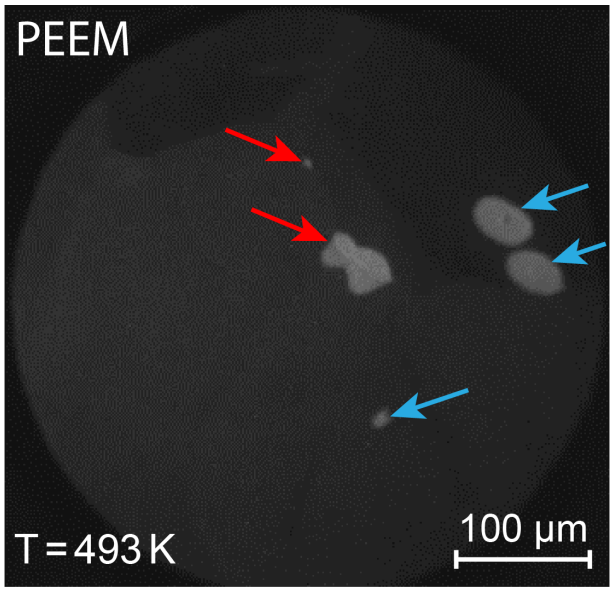

Fig. 3.18. Hydrogen oxidation reaction on a polycrystalline Rh foil at 493 K. The surface is mainly covered with oxygen (dark areas). Arrows mark propagating reaction fronts that nucleated on defects and enlarge the hydrogen covered areas (bright areas) on the polycrystalline surface. Red arrows label nucleation on grain boundaries and blue arrows label nucleation on defects within a domain.

nucleation events occur either on grain boundaries indicated by red arrows, or nucleation events marked with blue arrows take place on defects within a Rh domain.

3.3.2.2 Anisotropy of spreading fronts

The spreading of hydrogen oxidation reaction fronts is guided by the influence of the Rh surface crystallography as discussed in section 1.5. Smooth low miller index Rh single crystals e.g. with an isotropic Rh(111) surface exhibit circular or triangular shaped

reaction fronts [42]. The Rh(110) surface instead is an anisotropic surface with grooves that guide the reaction front to an elliptical shape [39]. High Miller index surfaces provide step edges, that promote hydrogen diffusion parallel to the step edge direction. The polycrystalline Rh foil, hosting different stepped surfaces and since the nucleation of fronts occurs also on defects within a domain as explained in section 3.3.2.1, is suitable to study the influence of high Miller index surface orientations on the preferred direction of front spreading. By observing the spreading fronts on different domains of this Rh

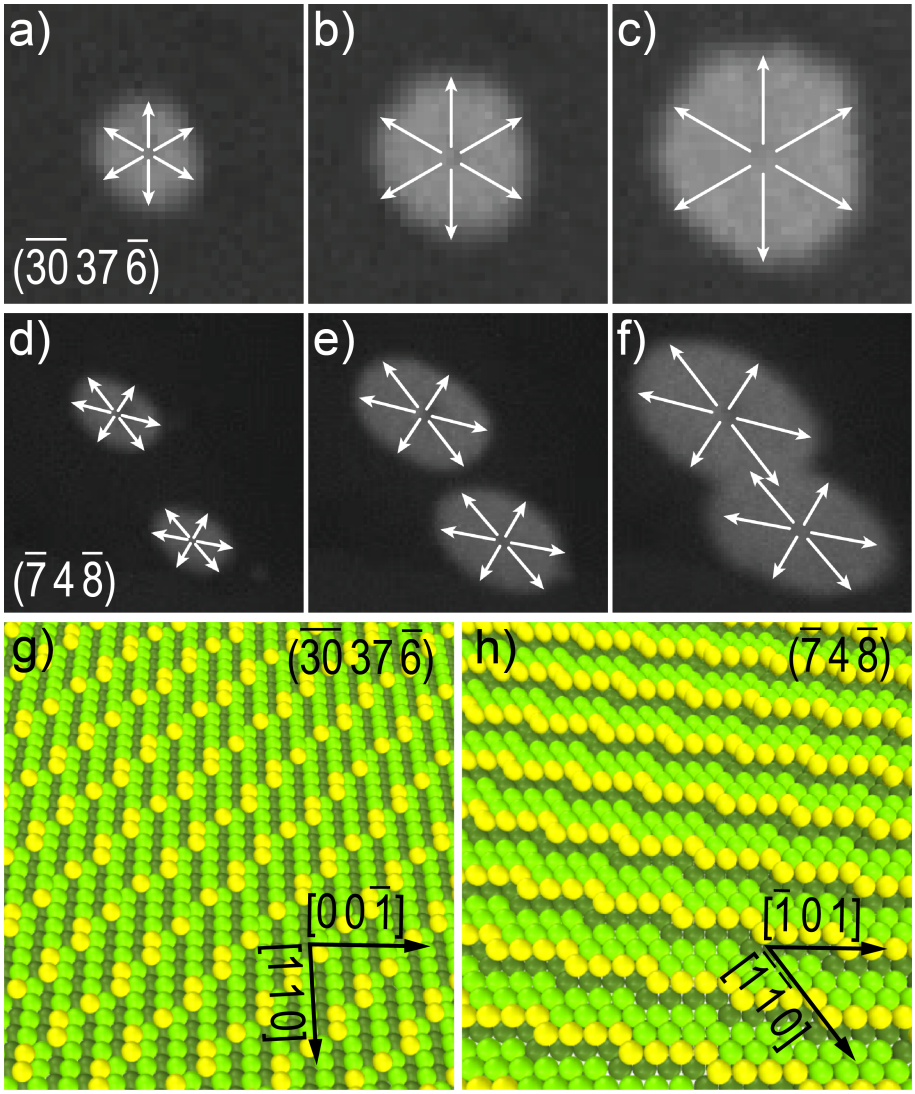

Fig. 3.19. Front propagation during hydrogen oxidation on stepped Rh surfaces: a-c) A Rh($\bar{3}0\,37\,\bar{6}$) domain nucleated an isotropic, circular spreading front. The corresponding ball model of the surface orientation is shown in (g); d-f) a Rh($\bar{7}4\bar{8}$) surface shows an anisotropic, elliptically shaped reaction front. The corresponding ball model is shown in (h); g) ball model of a Rh($\bar{3}0\,37\,\bar{6}$)surface; h) ball model of a Rh($\bar{7}4\bar{8}$) surface

surface structure library, the structure sensitivity of the directions of front propagation is uncovered. Figure 3.19 shows examples of isotropic and anisotropic front propagation on a Rh($3\bar{0}\,3\,7\,\bar{6}$) and a Rh($\bar{7}4\bar{8}$) stepped surface. In the case of Rh($3\bar{0}\,3\,7\,\bar{6}$) the surface consists of Rh{110} terraces (Fig. 3.19g) separated by kinked step edges. On this surface the hydrogen oxidation reaction exhibits an isotropic, almost circular front propagation (Fig. 3.19a-c). The expected anisotropic propagation on a Rh{110}terraces seems to be compensated by the kinked step edges cutting the Rh{110} grooves at an angle of about 45°. On the Rh($\bar{7}4\bar{8}$) surface the reaction shows an anisotropic front propagation behavior (Fig. 3.19d-f). However, the terraces of the Rh($\bar{7}4\bar{8}$) surface are isotropic Rh{111} oriented (Fig. 3.19h) surfaces but the high step density seems to guide the front spreading into a preferred direction. This results in an elliptically shaped reaction front.

4

Conclusion

In the present work, the catalytic behavior of the hydrogen oxidation reaction on Rh samples was investigated in the 10^{-6} *mbar* regime using field emission microscopy (FEM) and photo emission electron microscopy (PEEM). Differently sized Rh samples were used to study the change of reaction behavior along a size axis. All samples were prepared so that they exposed differently oriented Rh surfaces that were probed *in situ* by parallel imaging. Structure sensitivity of the catalytic hydrogen oxidation was observed using these Rh-"surface structure libraries"

The apex of a Rh-nanotip was prepared by field evaporation to have a radius of curvature of 25 nm. In turn, chemical processing and annealing was used to shape a curved crystal in the µm-dimension. The shape of the Rh nanotip could be determined by field ion microscopy (FIM) and that of the curved Rh crystal by scanning electron microscopy (SEM). The crystallography of both curved Rh samples was determined by means of stereographic projection. The polycrystalline Rh-foil was characterized with electron backscatter diffraction (EBSD) that provided a map of Miller index domains.

Insights into kinetics of catalytic hydrogen oxidation reaction could be taken by the *kinetics by imaging* approach. A relationship between the local PEEM and FEM image brightness and the catalytic activity of the reaction was established: The oxygen covered Rh surface (low activity state) has a lower work function providing a lower electron yield and a darker image contrast than the reduced hydrogen covered surface. Kinetic transitions between the low and high activity states could therefore be monitored *in situ* by PEEM and FEM in a particular external parameter range. Cycle wise variation of p_{H_2} at constant p_{O_2} and T could reveal the hysteresis-like kinetics of the reaction. This represents the bistability in hydrogen oxidation on Rh, which results from the Langmuir-Hinshelwood mechanism combined with the adsorption behavior of O_2 and H_2. A set of experiments at different temperatures in a range of 433 to 493 K was summarized in the so called kinetic phase diagram for comparison of all studied systems, namely a polycrystalline Rh foil, a µm-sized curved crystal and a nm-sized Rh tip (Fig. 4.1). The topmost

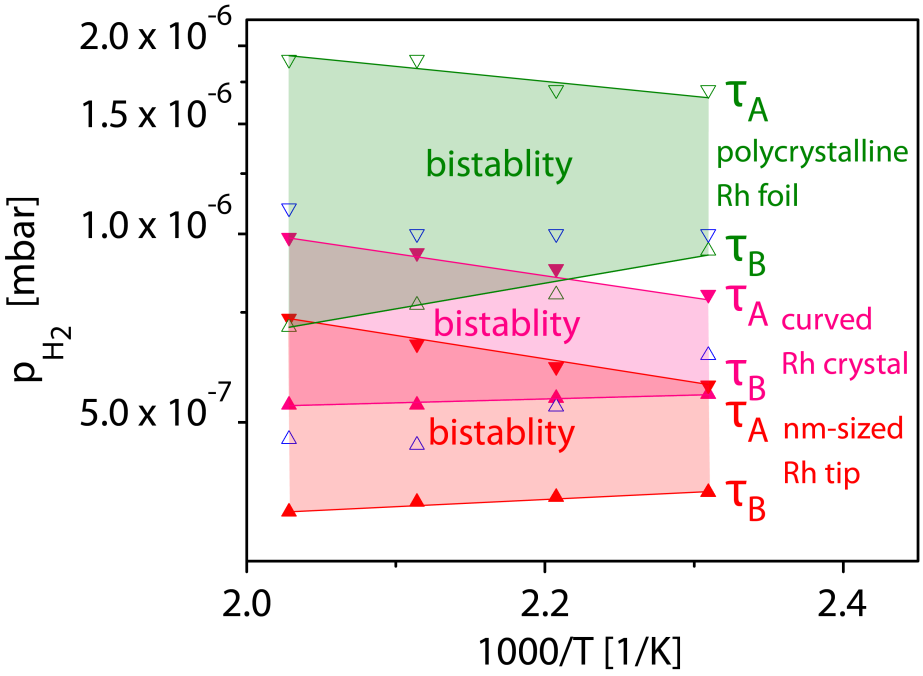

Fig. 4.1. Differently sized Rh samples in a kinetic phase diagram covering a temperature range of 433 to 493 K at a constant p_{O_2} of 7.7×10^{-7} *mbar*.

phase diagram (green) corresponds to the polycrystalline Rh foil sample, the centric phase diagram (purple) is corresponding to the µm-sized curved crystal and on the low end of the p_{H_2} axis the phase diagram of the nm-sized tip is located (red). The position of the bistability area in respect to p_{H_2} correlates with the size and properties of the catalytic systems. Due to the small size of the facets, the surface of the nm-sized curved apex has a higher contribution of low coordinated Rh atoms in comparison to the surface of the µm-sized curved crystal. The polycrystalline Rh foil domains of µm-size have an even lower percentage of low coordinated Rh atoms. This affects the position of the phase diagram.

Kinetic transitions in hydrogen oxidation reaction were spatially resolved by FEM and PEEM in order to reveal structure sensitivity of the reaction. On the nm-sized Rh apex the reaction fronts accompanying the transitions, couple the reaction over the whole sample surface. However, a "stop-and-go" like front spreading was revealed between (111)-oriented triangular-like regions framed by (110)-like vicinal regions.

Water molecules formed as product of hydrogen oxidation could be ionized and used for FIM imaging the active centers. In this way, the exact positions of nucleation centers

of reaction fronts could be revealed: they are located on Rh{112} facets. In turn, the µm-sized curved crystal was used as a "Zeitlupe" to image front propagation that takes longer across the larger facets compared to smaller facets on the nm-sized Rh apex. In such a way, spreading hydrogen fronts were observed to follow particular "pathways", starting from nucleation centers and spreading until high catalytic activity on the whole curved sample surface is reached. At different temperatures in a range from 393 to 493 K different "pathways" were observed, whereas the Rh{113} facets were observed to delay the front propagation above 433 K. It can be concluded that temperature dependent oxygen-induced surface reconstructions alter the surface structure changing the direction and velocity of front propagation.

On the polycrystalline Rh sample propagating fronts could be observed to nucleate on both, macroscopic defects and grain boundaries. The particular surface structure of the individual domains governs the front propagation: e.g. the steps of a Rh($\bar{7}4\bar{8}$) surface guide reaction fronts to an elliptical shape, although a circular form could be expected due to the (111) structure of terraces on this surface.

Summarizing it could be said, that known difficulties of comparative experiments in catalysis research can be overcome by using "surface structure libraries" in combination with spatially resolved kinetic experiments by exposing different crystallographic orientations to identical reaction conditions simultaneously. Polycrystalline precious metal foil (Rh in the present case), consisting of many µm-sized domains of different structures, as well as µm-sized "curved" crystals and nm-sized nanotips are examples of such "surface structure libraries" and provide promising insights into the structure dependency and heterogeneity of catalytic reactions, such as hydrogen oxidation on Rh.

List of figures

References

[1] P. E. McGovern, J. Zhang, J. Tang, Z. Zhang, G. R. Hall, R. A. Moreau, A. Nunez, E. D. Butrym, M. P. Richards, C.-s. Wang, G. Cheng, Z. Zhao, C. Wang, *Proceedings of the National Academy of Sciences* **2004**, *101*, 17593–17598.

[2] J. Wang, L. Liu, T. Ball, L. Yu, Y. Li, F. Xing, *Proceedings of the National Academy of Sciences* **2016**, *113*, 6444–6448.

[3] J. Berzelius, *Årsberättelse om framstegen i fysik och kemi*, Norstedt, **1835**.

[4] J. W. Döbereiner, *Ueber neu entdeckte höchst merkwürdige Eigenschaften des Platins und die pneumatisch-capillare Thätigkeit gesprungener Gläser: ein Beitrag zur Corpuscularphilosophie*, Jena: Schmid, **1823**.

[5] W. Ostwald, *Zeitschrift für Physik* **1902**, *3*, 313.

[6] B. E. Smith, R. L. Richards, W. E. Newton, *Catalysts for nitrogen fixation: nitrogenases, relevant chemical models and commercial processes*, *Vol. 1*, Springer Science & Business Media, **2013**.

[7] J. W. Erisman, M. A. Sutton, J. Galloway, Z. Klimont, W. Winiwarter, *Nature Geoscience* **2008**, *1*, 636–639.

[8] G. Ertl, *Journal of Vacuum Science & Technology A: Vacuum Surfaces and Films* **1983**, *1*, 1247–1253.

[9] J. Arblaster, *Platinum Metals Review* **1996**, *40*, 62.

[10] T. Wilberforce, Z. El-Hassan, F. Khatib, A. A. Makky, A. Baroutaji, J. G. Carton, A. G. Olabi, *International Journal of Hydrogen Energy* **2017**, *42*, 25695–25734.

[11] P. E. Dodds, I. Staffell, A. D. Hawkes, F. Li, P. Grünewald, W. McDowall, P. Ekins, *International Journal of Hydrogen Energy* **2015**, *40*, 2065–2083.

[12] G. B. Kauffman, *Platinum Metals Review* **1999**, *43*, 122–128.

[13] M. Ó. Conaire, H. J. Curran, J. M. Simmie, W. J. Pitz, C. K. Westbrook, *International Journal of Chemical Kinetics* **2004**, *36*, 603–622.

[14] V. Gorodetskii, J. Block, W. Drachsel, *Applied Surface Science* **1994**, *76-77*, 129–135.

[15] R. J. Baxter, P. Hu, *The Journal of Chemical Physics* **2002**, *116*, 4379–4381.

[16] S. Weller, *AIChE Journal* **1956**, *2*, 59–62.

[17] A. Anton, D. C. Cadogan, *Surface Science* **1990**, *239*, L548–L560.

[18] D. Castner, B. Sexton, G. Somorjai, *Surface Science* **1978**, *71*, 519–540.

[19] J. Derouin, R. G. Farber, D. R. Killelea, *The Journal of Physical Chemistry C* **2015**, *119*, 14748–14755.

[20] D. Castner, G. Somorjai, *Applications of Surface Science* **1980**, *6*, 29–38.

[21] P. Thiel, J. Yates, W. Weinberg, *Surface Science* **1979**, *82*, 22–44.

[22] K. D. Gibson, M. Viste, E. C. Sanchez, S. J. Sibener, *The Journal of Chemical Physics* **1999**, *110*, 2757–2760.

[23] J. Yates, P. Thiel, W. Weinberg, *Surface Science* **1979**, *82*, 45–68.

[24] E. Schwarz, J. Lenz, H. Wohlgemuth, K. Christmann, *Vacuum* **1990**, *41*, 167–170.

[25] D. N. Belton, G. B. Fisher, C. L. DiMaggio, *Surface Science* **1990**, *233*, 12–26.

[26] V. K. Medvedev, Y. Suchorski, C. Voss, T. V. de Bocarmé, T. Bär, N. Kruse, *Langmuir* **1998**, *14*, 6151–6157.

[27] P. Dudin, A. Barinov, L. Gregoratti, M. Kiskinova, F. Esch, C. Dri, C. Africh, G. Comelli, *The Journal of Physical Chemistry B* **2005**, *109*, 13649–13655.

[28] G. Hoogers, D. King, *Surface Science* **1993**, *286*, 306–316.

[29] K. A. Peterlinz, S. Sibener, *Surface Science* **1995**, *344*, L1239–L1244.

[30] S. Schwegmann, H. Over, V. D. Renzi, G. Ertl, *Surface Science* **1997**, *375*, 91–106.

[31] J. Wider, T. Greber, E. Wetli, T. Kreutz, P. Schwaller, J. Osterwalder, *Surface Science* **1998**, *417*, 301–310.

[32] M. Todorova, W. X. Li, M. V. Ganduglia-Pirovano, C. Stampfl, K. Reuter, M. Scheffler, *Physical Review Letters* **2002**, *89*, 96103.

[33] V. Zhdanov, B. Kasemo, *Surface Science Reports* **1994**, *20*, 113–189.

[34] M. Cencini, C. Lopez, D. Vergni in *Lecture Notes in Physics*, Springer Berlin Heidelberg, **2003**, pp. 187–210.

[35] B. von Boehn, R. Imbihl, *Physical Chemistry Chemical Physics* **2017**, *19*, 18487–18493.

[36] A. S. Mikhailov, *Foundations of Synergetics I*, Springer Berlin Heidelberg, **1994**.

[37] M. Berdau, G. G. Yelenin, A. Karpowicz, M. Ehsasi, K. Christmann, J. H. Block, *The Journal of Chemical Physics* **1999**, *110*, 11551–11573.

[38] D. Vogel, C. Spiel, Y. Suchorski, A. Trinchero, R. Schlögl, H. Grönbeck, G. Rupprechter, *Angewandte Chemie International Edition* **2012**, *51*, 10041–10044.

[39] F. Mertens, R. Imbihl, *Chemical Physics Letters* **1995**, *242*, 221–227.

[40] A. Schaak, R. Imbihl, *The Journal of Chemical Physics* **2000**, *113*, 9822–9829.

[41] A. Schaak, S. Shaikhutdinov, R. Imbihl, *Surface Science* **1999**, *421*, 191–203.

[42] A. Schaak, R. Imbihl, *Chemical Physics Letters* **1998**, *283*, 386–390.

[43] A. Schaak, B. Nieuwenhuys, R. Imbihl, *Surface Science* **1999**, *441*, 33–44.

[44] M. Tammaro, J. Evans, C. Rastomjee, W. Swiech, A. Bradshaw, R. Imbihl, *Surface Science* **1998**, *407*, 162–170.

[45] V. Gorodetskii, V. Elokhin, J. Bakker, B. Nieuwenhuys, *Catalysis Today* **2005**, *105*, 183–205.

[46] V. Gorodetskii, B. Nieuwenhuys, W. Sachtler, G. Boreskov, *Surface Science* **1981**, *108*, 225–234.

[47] Y. Suchorski, G. Rupprechter, *Surface Science* **2016**, *643*, 52–58.

[48] Y. Suchorski, C. Spiel, D. Vogel, W. Drachsel, R. Schlögl, G. Rupprechter, *ChemPhysChem* **2010**, *11*, 3231–3235.

[49] E. W. Müller, *Zeitschrift für Physik* **1937**, *106*, 541.

[50] E. W. Müller, *Zeitschrift für Physik* **1951**, *131*, 136.

[51] C. Eyring, S. Mackeown, R. Millikan, *Physical Review* **1928**, *31*, 900.

[52] R. H. Fowler, L. Nordheim, *Proceedings of the Royal Society A: Mathematical Physical and Engineering Sciences* **1928**, *119*, 173–181.

[53] R. P. Johnson, W. Shockley, *Physical Review* **1936**, *49*, 436–440.

[54] E. W. Müller, *ZS. f. techn. Physik* **1936**, *17*.

[55] E. W. Müller, *Zeitschrift für Physik* **1937**, *106*, 132.

[56] R. Smoluchowski, *Physical Review* **1941**, *60*, 661–674.

[57] R. G. Forbes, J. H. Deane, *Proceedings of the Royal Society A: Mathematical Physical and Engineering Sciences* **2007**, *463*, 2907–2927.

[58] E. W. Müller, *Die Naturwissenschaften* **1941**, *29*, 533–534.

[59] M. G. Inghram, R. Gomer, *The Journal of Chemical Physics* **1954**, *22*, 1279–1280.

[60] E. W. Müller, K. Bahadur, *Physical Review* **1956**, *102*, 624–631.

[61] E. W. Müller, *Journal of Applied Physics* **1956**, *27*, 474–476.

[62] J. L. Wiza et al., *Nucl. Instrum. Methods* **1979**, *162*, 587–601.

[63] E. Brüche, *Die Naturwissenschaften* **1932**, *20*, 49–49.

[64] E. Brüche, *Zeitschrift für Physik* **1933**, *86*, 448–450.

[65] H. Johannson, *Annalen der Physik* **1933**, *410*, 385–413.

[66] H. Düker, A. Illenberger, *Die Naturwissenschaften* **1962**, *49*, 445–446.

[67] W. Telieps, E. Bauer, *Ultramicroscopy* **1985**, *17*, 57–65.

[68] W. Engel, M. Kordesch, H. Rotermund, S. Kubala, A. von Oertzen, *Ultramicroscopy* **1991**, *36*, 148–153.

[69] H. H. Rotermund, W. Engel, M. Kordesch, G. Ertl, *Nature* **1990**, *343*, 355–357.

[70] M. Ehsasi, *Applied Surface Science* **1994**, *76-77*, 89–100.

[71] G. Ertl, *Angewandte Chemie International Edition* **2008**, *47*, 3524–3535.

[72] H. Hertz, *Annalen der Physik und Chemie* **1887**, *267*, 983–1000.

[73] W. Hallwachs, *Annalen der Physik und Chemie* **1888**, *269*, 301–312.

[74] A. Einstein, *Annalen der Physik* **1905**, *322*, 132–148.

[75] P. D. Innes, *Proceedings of the Royal Society A: Mathematical Physical and Engineering Sciences* **1907**, *79*, 442–462.

[76] K. Siegbahn, K. Edvarson, *Nuclear Physics* **1956**, *1*, 137–159.

[77] S. Kono, S. M. Goldberg, N. F. T. Hall, C. S. Fadley, *Physical Review Letters* **1978**, *41*, 1831–1835.

[78] K. Siegbahn, *Reviews of Modern Physics* **1982**, *54*, 709–728.

[79] K. Vernon-Parry, *III-Vs Review* **2000**, *13*, 40–44.

[80] S. Nishikawa, S. Kikuchi, *Proceedings of the Imperial Academy* **1928**, *4*, 475–477.

[81] R. A. Schwarzer, D. P. Field, B. L. Adams, M. Kumar, A. J. Schwartz in *Electron Backscatter Diffraction in Materials Science*, (Eds.: A. J. Schwartz, M. Kumar, B. L. Adams, D. P. Field), Springer US, **2009**, pp. 1–20.

[82] B. L. Adams, S. I. Wright, K. Kunze, *Metallurgical Transactions A* **1993**, *24*, 819–831.

[83] G. L. W. Cross, A. Schirmeisen, P. Grütter, U. T. Dürig, *Nature Materials* **2006**, *5*, 370–376.

[84] W. Paul, Y. Miyahara, P. Grütter, *Nanotechnology* **2012**, *23*, 335702.

[85] D. NiewieczerzaŁ, C. Oleksy, A. Szczepkowicz, *Ultramicroscopy* **2012**, *112*, 1–9.

[86] J. A. Panitz, S. B. McLane, E. W. Müller, *Review of Scientific Instruments* **1969**, *40*, 1321–1324.

[87] G. Comelli, V. Dhanak, M. Kiskinova, G. Paolucci, K. Prince, R. Rosei, *Surface Science* **1992**, *269-270*, 360–364.

[88] B. Lang, R. Joyner, G. Somorjai, *Surface Science* **1972**, *30*, 440–453.

[89] S. Bernasek, G. Somorjai, *Surface Science* **1975**, *48*, 204–213.

[90] D. Woodruff, *Journal of Physics: Condensed Matter* **2016**, *28*, 491001.

[91] A. Armitage, H. Liu, D. Woodruff, *Vacuum* **1981**, *31*, 519–522.

[92] A. Armitage, D. Woodruff, *Surface Science* **1982**, *114*, 414–430.

[93] J. Arlow, D. Woodruff, *Surface Science* **1985**, *157*, 327–338.

[94] J. Arlow, D. Woodruff, *Surface Science* **1985**, *162*, 310–315.

[95] J. Arlow, D. Woodruff, *Surface Science* **1987**, *180*, 89–109.

[96] A. de Alwis, B. Holsclaw, V. Pushkarev, A. Reinicker, T. Lawton, M. Blecher, E. Sykes, A. Gellman, *Surface Science* **2013**, *608*, 80–87.

[97] T. Lawton, V. Pushkarev, E. Broitman, A. Reinicker, E. Sykes, A. Gellman, *The Journal of Physical Chemistry C* **2012**, *116*, 16054–16062.

[98] M. Datler, I. Bespalov, S. Buhr, J. Zeininger, M. Stöger-Pollach, J. Bernardi, G. Rupprechter, Y. Suchorski, *Catalysis Letters* **2016**, *146*, 1867–1874.

[99] H. D. Beckey, *Zeitschrift für Naturforschung A* **1959**, *14*, 712.

[100] A. R. Anway, *The Journal of Chemical Physics* **1969**, *50*, 2012–2021.

[101] H. J. Heinen, F. W. Röllgen, H. D. Beckey, *Zeitschrift für Naturforschung A* **1974**, *29*, 773.

[102] N. Ernst, G. Bozdech, J. H. Block, *Berichte der Bunsengesellschaft für physikalische Chemie* **1978**, *82*, 756–766.

[103] N. Ernst, G. Ehrlich in *Topics in Current Physics*, Springer Berlin Heidelberg, **1986**, pp. 75–115.

[104] V. Gorodetskii, W. Drachsel, J. Block, *Applied Surface Science* **1994**, *76-77*, 122–128.

[105] N. Ernst, G. Bozdech, V. Gorodetskii, H.-J. Kreuzer, R. Wang, J. Block, *Surface Science* **1994**, *318*, L1211–L1218.

[106] W. Drachsel, C. Wesseling, V. Gorodetskii, *Le Journal de Physique IV* **1996**, *06*, C5–31–C5–36.

[107] W. A. Schmidt, *Zeitschrift für Naturforschung A* **1964**, *19*, 318–327.

[108] T. V. de Bocarmé, G. Beketov, N. Kruse, *Surface and Interface Analysis* **2004**, *36*, 522–527.

[109] F. Mittendorfer, *Journal of Physics: Condensed Matter* **2010**, *22*, 393001.

[110] J. Klikovits, M. Schmid, L. R. Merte, P. Varga, R. Westerström, A. Resta, J. N. Andersen, J. Gustafson, A. Mikkelsen, E. Lundgren, F. Mittendorfer, G. Kresse, *Physical Review Letters* **2008**, *101*, 266104.

[111] F. Mittendorfer, T. Franz, J. Klikovits, M. Schmid, L. R. Merte, S. S. Zaman, P. Varga, R. Westerström, A. Resta, J. N. Andersen, J. Gustafson, E. Lundgren, *The Journal of Physical Chemistry Letters* **2011**, *2*, 2747–2751.

Appendix

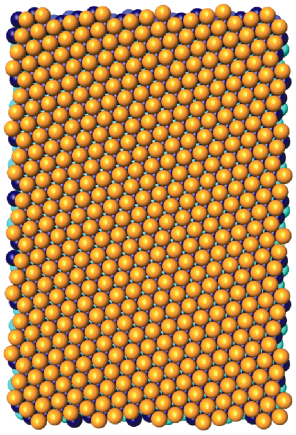

Rh(111)

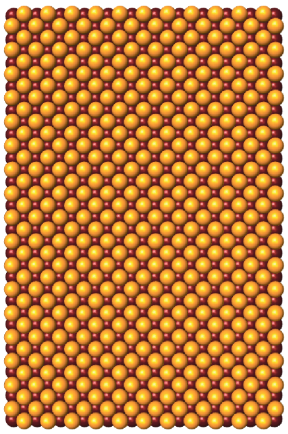

Rh(001)

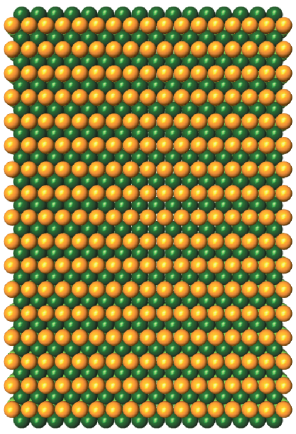

Rh(101)

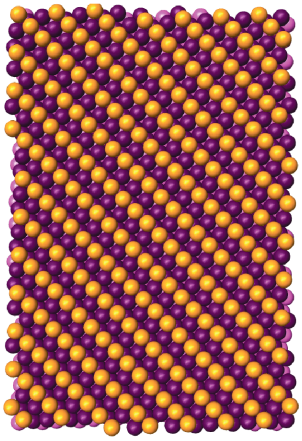

Rh(113)

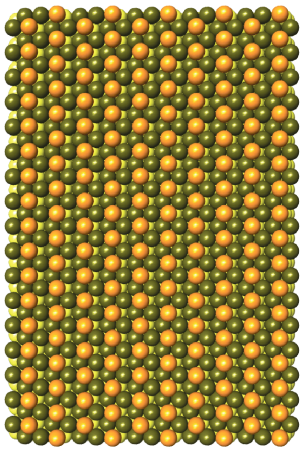

Rh(102)

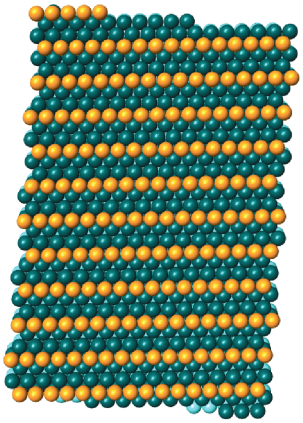

Rh(133)

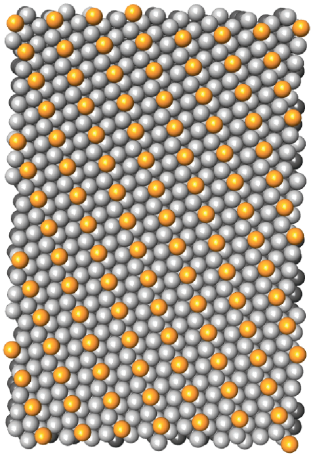

Rh(123)

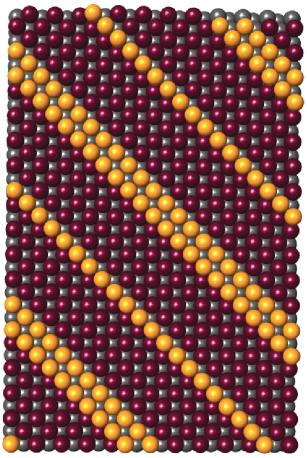

Rh(1110)